

Doctoral theses at NTNU, 2024:87

Erik Koren

A study on hydrogen uptake and diffusion in X65 pipeline steel using gaseous and electrochemical methods

Doctoral thesis

NTNU
Norwegian University of Science and Technology
Thesis for the Degree of
Philosophiae Doctor
Faculty of Engineering
Department of Mechanical and Industrial
Engineering



Norwegian University of
Science and Technology

Erik Koren

A study on hydrogen uptake and diffusion in X65 pipeline steel using gaseous and electrochemical methods

Thesis for the Degree of Philosophiae Doctor

Trondheim, March 2024

Norwegian University of Science and Technology
Faculty of Engineering
Department of Mechanical and Industrial Engineering

NTNU

Norwegian University of Science and Technology

Thesis for the Degree of Philosophiae Doctor

Faculty of Engineering

Department of Mechanical and Industrial Engineering

© Erik Koren

ISBN 978-82-326-7768-9 (printed ver.)

ISBN 978-82-326-7767-2 (electronic ver.)

ISSN 1503-8181 (printed ver.)

ISSN 2703-8084 (online ver.)

Doctoral theses at NTNU, 2024:87

Printed by NTNU Grafisk senter

Preface

This doctoral thesis concludes the work performed to fulfill the requirements for the Philosophiae Doctor (PhD) degree at the Norwegian University of Science and Technology (NTNU). The work was performed at the Department of Mechanical and Industrial Engineering at NTNU in Trondheim, Norway, from August 2020 to September 2023. A 4 months research stay was spent at the Department of Mechanical Engineering at Kyushu University (KU), Japan. Prof. Roy Johnsen was the main supervisor, and Dr. Dong Wang, the co-supervisor.

The PhD project was part of the *HyLINE - Safe Pipelines for Hydrogen Transport*, a research collaboration between NTNU, KU, and SINTEF. The project was funded by the Norwegian Research Council (Project code: 294739), in addition to industrial partners: Equinor, Gassco, TechnipFMC, AirLiquide, NEL, TenarisDalmine, and TotalEnergies.

Abstract

Hydrogen, a clean energy carrier, is recognized as a critical building block to develop a carbon-neutral energy sector. To realize the hydrogen economy, it is essential to develop a hydrogen distribution infrastructure. Repurposing existing natural gas pipelines for H₂ gas transportation is an economically favored choice for long-distance hydrogen transportation. However, pipeline steels can be subjected to hydrogen embrittlement (HE), and HE susceptibility is an essential part of evaluating the feasibility of repurposing pipelines. Hydrogen uptake and diffusivity can affect the degree of HE. H₂ gas charging is challenging due to safety risks and limited testing facilities. In contrast, electrochemical charging is a safer and more accessible method.

The objective of this PhD work is to relate electrochemical and gaseous hydrogen charging based on the hydrogen uptake. If the relationship is transferable to mechanical testing, electrochemical charging could support the evaluation of pipeline steels for H₂ gas transport. Hydrogen uptake, diffusivity, and trapping in one vintage and two modern X65 pipeline steels were investigated. Both electrochemical and gaseous hydrogen charging have been conducted. Hydrogen desorption and permeation techniques were employed in the investigation.

An equivalency in terms of hydrogen uptake between gaseous and electrochemical charging was established. A Sieverts' relationship was determined from H₂ gas permeation, which relates the hydrogen fugacity with the concentration in the steel. The hydrogen uptake from electrochemical permeation, in combination with the determined Sieverts' relationship was used to determine the equivalent fugacity and pressure of different electrochemical charging conditions. Electrochemical charging performed in a 3.5 wt% NaCl solution at applied current densities of -1 , -15 , and -50 mA cm⁻² were equivalent to hydrogen fugacities of 49.1, 101.9, and 222.7 bar. In addition, a systematic approach was conducted to determine an electrochemical charging condition equivalent to a H₂ gas pressure relevant for transportation (200 bar). Electrochemical charging in a 3.5 wt% NaCl solution with 2 g l⁻¹ thiourea at -1225 mV_{Ag/AgCl} was equivalent to a hydrogen pressure of 201.9 bar.

The effective hydrogen diffusion coefficient determined by different methods at room temperature was between 1.95×10^{-7} and 3.34×10^{-6} cm² s⁻¹ for the Vintage steel and between 8.56×10^{-7} and 2.70×10^{-6} cm² s⁻¹ for the Modern quenched and tempered steel. The larger scatter of the Vintage steel was attributed to a concentration-dependent effective diffusivity induced by multiple major trap sites. In addition, ferrite-pearlite bands in the Vintage steel could cause a more tortuous diffusion path.

Future work should be conducted to investigate the transferability of the determined equivalency to mechanical testing. In addition, studies on the effect of surface conditions on the hydrogen uptake, such as oxide layer, Pd coating, flow coating, and gas impurities, would be of interest.

Acknowledgments

I would like to thank my supervisor, Professor Roy Johnsen, for giving me this opportunity. Your support and guidance have been essential to me throughout this project. I would also like to thank my co-supervisor, Dr. Dong Wang. With your knowledge and encouragement, you have been an important contributor to me over the past three years.

I want to thank Associate Professor Xu Lu for always being available to discuss results and sharing your expertise, which has been most valuable during this work. I want to thank Dr. Catalina Hagen for performing the gas permeation experiments—for your positive attitude, ideas, and for always asking the important questions. I would also like to thank the members of the HyLINE project for showing interest in my work and bringing valuable input during our project meetings.

I am grateful to Professor Hisao Matsunaga and Professor Junichiro Yamabe for your hospitality during my stay at Kyushu University. I also want to thank Professor Yamabe for helping with experiments and always being available for scientific discussions. I want to thank Ritsuko Matsuo for helping with gas charging and TDS testing and for creating a friendly environment in the lab. A special thank you to everyone who helped me settle in at KU and made my stay memorable.

I also want to thank Nils-Inge Nilsen for help with gas charging for permeation tests. Thank you, Cristian, Ellen, Iman, and Shabnam, for sharing your knowledge and experience in the lab. A special thanks to Chandra for all the discussions and distractions. I was lucky to have you as an office mate. In addition, I thank my friends and colleagues at NTNU and KU for making the past three years good ones.

Finally, I want to thank my friends and family for being my biggest supporters. My deepest gratitude goes to my wife, Anne, for your patience, encouragement, and support.

Table of Contents

Preface	i
Abstract	iii
Acknowledgements	v
List of Figures	ix
List of Tables	xi
Nomenclature	xiii
1 Introduction	1
1.1 Background	1
1.2 Objective	2
1.3 Thesis overview	3
2 Literature review	5
2.1 Pipeline steel	5
2.2 Hydrogen embrittlement	6
2.2.1 Hydrogen embrittlement in pipeline steel	6
2.3 Hydrogen uptake	7
2.3.1 Uptake from gas	7
2.3.2 Uptake from electrolyte	8
2.3.3 Equivalent hydrogen charging	9
2.4 Hydrogen diffusivity	13
2.4.1 Lattice diffusivity	13
2.4.2 Effective diffusivity	14
3 Experimental	17
3.1 Materials	17
3.1.1 Vintage	17
3.1.2 Modern QT	18
3.1.3 Modern TMCP	19
3.2 Hydrogen permeation	20
3.2.1 Sample preparation	20
3.2.2 Electrochemical permeation	21
3.2.3 Gas permeation	22
3.2.4 Analysis	23

TABLE OF CONTENTS

3.3	Hydrogen desorption	24
3.3.1	Diffusivity	24
3.3.2	Hot extraction	25
3.3.3	Choo-Lee method	25
3.3.4	Effect of Pd coating	26
4	Summary of publications and report	27
4.1	Paper 1	27
4.2	Paper 2	28
4.3	Paper 3	29
4.4	Report	30
5	Conclusion and further work	33
5.1	Conclusion	33
5.2	Further work	34
	Bibliography	44
	Appended papers	47
	Paper 1	48
	Paper 2	60
	Paper 3	69
	Report	105

List of Figures

1.1	Map of the pipelines for gas transport on the Norwegian continental shelf. Reproduced from [7].	2
2.1	Influencing parameters on hydrogen embrittlement. Reproduced from [24].	6
2.2	Comparison of stress-strain curves of Inconel 625 after ex-situ precharging in high pressure H ₂ gas and electrolyte. Reproduced from [59]	11
2.3	Illustration of potential hydrogen trapping sites. Reproduced from [73].	15
3.1	SEM micrographs of the Vintage steel, as included in Paper 1.	18
3.2	Optical micrographs of the outer, middle, and inner positions of the Vintage steel. The cross section is parallel to the longitudinal direction. Adapted from [82, 84].	18
3.3	Microstructure of the Modern QT steel. Reproduced from [85].”The optical microscopy image (a) and BSE image (b) showing the overall matrix. (c) and (d) are ECCI showing detailed information of bainite and ferrite, respectively. (e–f) are IPF map, IQ map and KAM map in a same area, respectively.”	19
3.4	Optical micrographs of the outer, middle, and inner positions of the Modern QT steel. The cross section is parallel to the longitudinal direction. Adapted from [82, 84].	19
3.5	SEM characterization of the Total material. (a)IPF map, (b)IQ map and (c) KAM map of the same area. Adapted from [84].	20
3.6	Optical micrographs of the outer, middle, and inner positions of the Modern TMCP steel. The cross section is parallel to the longitudinal direction. Adapted from [84].	20
3.7	Image of the electrochemical permeation cell.	22

LIST OF FIGURES

3.8	Illustration of the magnitude of applied cathodic potential or current density and the response signal of the permeation current density as a function of time for (a) Complete permeation transients and (b) Partial permeation transients.	22
3.9	Image of the gas permeation cell.	23
3.10	Schematic of the in-situ and ex-situ hydrogen desorption tests to determine the hydrogen diffusivity.	25
3.11	Image of the Bruker G4 Phoenix that was used for hot extraction. . . .	26

List of Tables

2.1	Reported values in the literature of the equivalent hydrogen fugacity. Charging conditions are given as cathodic current density or overpotential.	12
3.1	Chemical composition of the Vintage steel.	17
3.2	Chemical composition of the Modern QT steel.	18
3.3	Chemical composition of the Modern TMCP steel.	19

Nomenclature

α	Heating rate
A	Constant related to the hydrogen evolution reaction
API	American Petroleum Institute
bcc	Body centered cubic
BSE	Backscattered electron
C_H	Hydrogen concentration
C_{HD}	Residual diffusible hydrogen concentration
C_0	Sub-surface hydrogen concentration in lattice sites
C_{0R}	Sub-surface hydrogen concentration in lattice and reversible trap sites
CP	Cathodic protection
D	Diffusion coefficient
D_{eff}	Effective diffusion coefficient
D_0	Pre-exponential of Arrhenius relationship for diffusion
DFT	Density functional theory
ECCI	Electron channeling contrast
E_a	De-trapping activation energy
E_b	Trap binding energy
E_d	Activation energy of diffusion
f	Fugacity
f_{H_2}	Hydrogen fugacity
$f_{H_2}^{\text{eq}}$	Equivalent hydrogen fugacity
FCGR	Fatigue crack growth rate
GC-MS	Gas chromatography-mass spectrometer
H_{abs}	Absorbed hydrogen atom
H_{ads}	Adsorbed hydrogen atom
HAZ	Heat affected zone
HE	Hydrogen embrittlement

NOMENCLATURE

HER	Hydrogen evolution reaction
i_p	Permeation current density
i_p^∞	Steady-state permeation current density
i_p^0	Initial permeation current density
IPF	Inverse pole figure
IQ	Image quality
J	Flux
KAM	Kernel average misorientation
L	Thickness
(M)	Metal surface site
[M]	Metal interstitial site
OM	Optical microscope
p	Pressure
p_{H_2}	Hydrogen pressure
$p_{H_2}^{eq}$	Equivalent hydrogen pressure
R	Ideal gas constant, [8.314 J K ⁻¹ mol ⁻¹]
S	Constant in Sieverts' law
SCE	Saturated calomel electrode
SEM	Scanning electron microscope
T	Temperature
T_p	Peak temperature
t	Time
t_b	Breakthrough time during permeation
t_{lag}	Time lag during permeation
t_R	Holding time during desorption measurement
TDS	Thermal desorption spectroscopy
TMCP	Thermo-mechanical controlled processed
QT	Quenched and tempered
η	Overpotential
ξ	Constant related to the hydrogen evolution reaction

Chapter 1

Introduction

1.1 Background

Hydrogen can be utilized as a feedstock, fuel, and energy carrier, and it does not release carbon dioxide when used [1]. EU has recognized hydrogen as a key priority in decarbonizing the energy sector [1]. To utilize the full potential of hydrogen, developing a hydrogen distribution infrastructure is essential. Pipelines are regarded as an economically favored option for long-distance transportation of hydrogen [2]. The existing infrastructure of low alloy pipeline steels used for natural gas transportation has been suggested to be repurposed to transport H₂ gas [3–6]. A map of the network of subsea pipelines for gas transportation on the Norwegian continental shelf is presented in Fig. 1.1 [7]. The network has a total length of 8800 km, approximately the distance between Oslo and Bangkok [7]. Repurposing pipelines to transport hydrogen gas could be a cost-effective choice compared with the development of new infrastructure [3] and would facilitate the use of hydrogen as an energy carrier.

Before natural gas pipelines can be used to transport H₂ gas, it is essential to investigate how the pipelines behave under pressurized H₂ gas exposure. Hydrogen can be taken up in a steel and degrade its mechanical properties, a phenomenon termed hydrogen embrittlement (HE) [8]. Exposure to pressurized H₂ gas can degrade pipeline steel's fatigue and fracture behavior [9–11]. Pipelines carrying gas are subjected to cyclic stresses because of pressure fluctuations. Consequently, it is essential to ensure that the fatigue and fracture properties of the pipeline are within acceptable limits under exposure to H₂ gas [12]. However, because pressurized H₂ gas is associated with safety risks and requires complicated and expensive equipment, testing of HE susceptibility is mainly conducted using electrochemical hydrogen charging [13]. The degree of hydrogen-assisted material degradation is affected by the hydrogen concentration in the steel and, thus, on the hydrogen charging conditions [14, 15]. Hence, a comparison of HE susceptibility between studies using different charging conditions is most appropriate when the induced hydrogen concentrations are comparable [16].

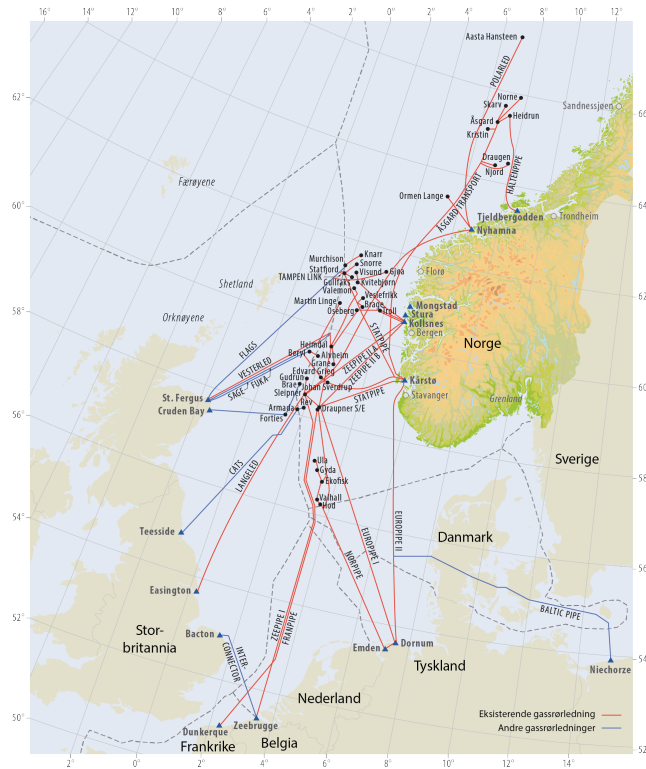


Figure 1.1: Map of the pipelines for gas transport on the Norwegian continental shelf. Reproduced from [7].

1.2 Objective

Before natural gas pipelines can be repurposed for H_2 gas transportation, it is essential to investigate the steel’s interaction with hydrogen and the susceptibility to hydrogen embrittlement under gaseous hydrogen exposure. If electrochemical charging could aid in the evaluation of repurposing pipelines, it could accelerate the development of the hydrogen economy. Hence, the emphasis in this PhD project was put on relating the hydrogen uptake from pressurized H_2 gas and electrochemical hydrogen charging. To determine the hydrogen concentration, diffusivity, and trapping-related parameters, both hydrogen permeation and desorption experiments were performed. Investigations were conducted using both gaseous and electrochemical hydrogen charging. Both vintage, existing, X65 pipeline steel and modern X65 pipeline steels were investigated to elucidate microstructural effects on the hydrogen-steel interaction.

The main objectives of this PhD project were to:

- Develop a method to determine a relationship between electrochemical and gaseous hydrogen sources in terms of hydrogen uptake.
- Use a systematic approach to determine an electrochemical charging condition that produces the same hydrogen uptake as exposure to H_2 gas at a pressure

relevant to hydrogen transportation in pipelines.

- Investigate the significance of microstructural differences between vintage and modern X65 pipeline steels on hydrogen uptake, diffusion, and trapping properties.
- Evaluate permeation and desorption techniques, in addition to charging conditions, for investigation of hydrogen uptake, diffusion, and trapping in X65 pipeline steels.

1.3 Thesis overview

In **Chapter 2**, relevant literature and theory will be presented. **Chapter 3** presents the materials and methods. **Chapter 4** contains a summary of each journal article and report. Lastly, in **Chapter 5**, the final conclusions and suggestions for further work are made.

The thesis consists of three journal papers and one report containing unpublished results, which are all included in the appendix.

Paper 1

Experimental comparison of gaseous and electrochemical hydrogen charging in X65 pipeline steel using the permeation technique

Authors: Erik Koren, Catalina M. H. Hagen, Dong Wang, Xu Lu, Roy Johnsen, Junichiro Yamabe

Corrosion Science 215 (2023) 111025

DOI: <https://doi.org/10.1016/j.corsci.2023.111025>

Contributions:

- Koren, Hagen, and Johnsen planned experiments.
- Koren performed electrochemical permeation. Hagen performed gas permeation. Wang performed scanning electron microscopy analysis.
- Koren conducted the data analysis. All authors contributed to the discussion of the results.
- Koren wrote the original draft. All authors contributed with reviewing and editing.

Paper 2

Investigating electrochemical charging conditions equivalent to hydrogen gas exposure of X65 pipeline steel

Authors: Erik Koren, Catalina M. H. Hagen, Dong Wang, Xu Lu, Roy Johnsen

Materials and Corrosion (2023) 1-7

DOI: <https://doi.org/10.1002/maco.202313931>

Contributions:

- Koren, Hagen, and Johnsen planned experiments.
- Koren performed electrochemical permeation. Hagen performed gas permeation.
- Koren conducted the data analysis. All authors contributed to the discussion of the results.
- Koren wrote the original draft. All authors contributed with reviewing and editing.

Paper 3

Hydrogen diffusivity in X65 pipeline steel: Desorption and permeation studies

Authors: Erik Koren, Junichiro Yamabe, Xu Lu, Catalina. M. H. Hagen, Dong Wang, Roy Johnsen

Under review in the International Journal of Hydrogen Energy

Contributions:

- Koren, Johnsen, and Yamabe planned experiments.
- Koren performed electrochemical permeation. Yamabe performed desorption experiments.
- Koren and Yamabe conducted the data analysis. All authors contributed to the discussion of the results.
- Koren wrote the original draft. All authors contributed with reviewing and editing.

Project report

Hydrogen uptake and diffusivity in X65 steel: Results included in a project report but are not published.

Contributions:

- Koren, Yamabe, and Johnsen planned experiments.
- Koren performed electrochemical permeation. Koren and Yamabe performed desorption experiments.
- Koren wrote the original draft. Johnsen contributed with reviewing and editing.

Chapter 2

Literature review

This chapter presents the relevant literature found over the course of this PhD project. Initially, an extensive literature review was conducted when a "state-of-the-art" report on hydrogen uptake and diffusivity in steels exposed to hydrogen gas was written [17]. The literature review has been extended during the work with papers and reports. The theory presented in this chapter is amended and elaborated from the literature presented in the authored papers and reports.

2.1 Pipeline steel

High strength low alloy steels are suitable as pipeline materials because of their good formability and weldability, in addition to exhibiting a good balance of strength and fracture resistance [18]. Due to the requirement of good weldability and formability, it is required to keep the carbon content low (<0.25 wt%) [19]. The main strengthening mechanisms are grain refinement, solid solution strengthening, and precipitation hardening, which are obtained by proper thermomechanical treatment and microalloying [20]. Mn is added to reduce the austenite-ferrite transformation temperature, and typical microalloying elements are Nb, V, Ti, and Mo [20]. During hot rolling, bands can form parallel to the rolling direction due to remnant interdendritic segregation from casting [18]. Various microstructures can be obtained, from ferrite-pearlite to bainite with martensite or retained austenite islands [20]. Modern steels typically have lower carbon content (0.03-0.06 %), reduced pearlite fraction, and more often a ferritic-bainitic microstructure compared with vintage steels where ferritic-pearlitic microstructure are more common [19, 20]. Low alloy pipeline steels are commonly denoted after their specified minimum yield strength, as described by the American Petroleum Institute (API) specification 5L [21], e.g., grades having a minimum yield strength of 450 MPa, which corresponds to 65 ksi, are denoted as API 5L X65 steels. For high-pressure subsea pipelines, API 5L X60 or X65 grade low carbon steels are commonly used [22]. The pipes are most commonly submerged arc-welded or seamless [22].

2.2 Hydrogen embrittlement

Hydrogen-induced degradation of mechanical properties was described already in the 1870s when Johnson [23] reported a reduction in ductility and toughness in iron and steels immersed in acids. As hydrogen-induced material degradation occurs as embrittlement, the phenomenon is referred to as hydrogen embrittlement (HE) [8]. HE of materials is dependent on a large number of parameters. The influencing parameters can be divided into those regarding mechanical, material, and environment, as summarized in Figure 2.1 [24]. Extensive research has been conducted to elucidate the root cause of HE, and several mechanisms have been proposed; however, these are still readily discussed [8, 25]. Hydrogen can be introduced to steels during manufacturing processes such as casting, welding, or electroplating [8]. Hydrogen can also be taken up during service from corrosion processes, cathodic protection, or exposure to H_2 gas [8]. Pressurized H_2 gas has been shown to reduce the fracture resistance and fatigue life of pipeline steels [10, 11, 26, 27].

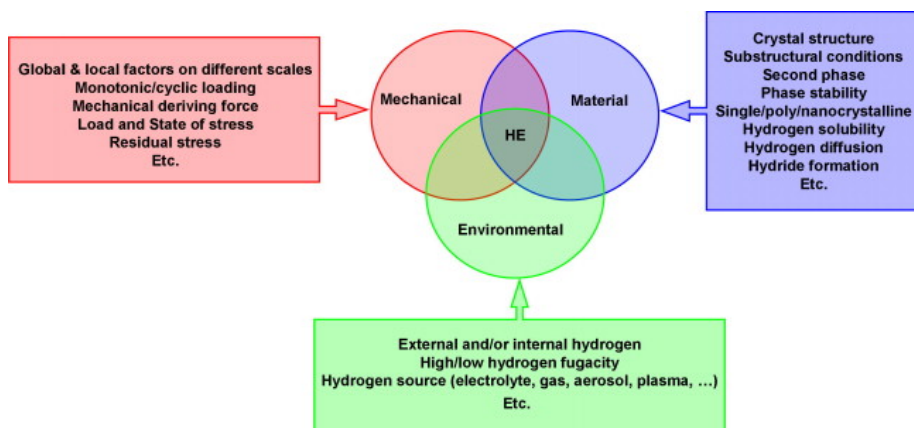


Figure 2.1: Influencing parameters on hydrogen embrittlement. Reproduced from [24].

2.2.1 Hydrogen embrittlement in pipeline steel

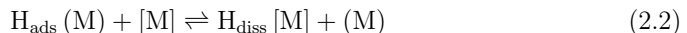
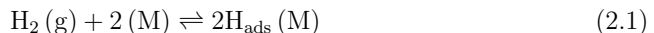
The growing interest in hydrogen gas transportation through pipelines has led to recent attention in investigating the hydrogen embrittlement susceptibility of pipeline steels under a gaseous hydrogen environment [9–11, 14, 26–28]. It is generally considered that higher-grades steels are more susceptible to hydrogen embrittlement [29]. Reduction in ductility during tensile tests in pressurized hydrogen gas is reported in X52, X65, X80, and X100 pipeline steels, and the degree of HE increases with increasing pressure [14, 30]. As will be further elaborated in Section 2.3.1, the presence of a surface oxide can act as a barrier to hydrogen uptake from H_2 gas. During tensile testing of pipeline steels in H_2 gas, an increased rate of hydrogen uptake can occur when the applied load is sufficient to break the oxide layer [14]. Gas pipelines are subjected to fatigue due to pressure fluctuations causing cyclic stresses [4, 5], which can cause breakage of the oxide layer and lead to local hydrogen uptake at the bare surface. Several studies have reported degradation in fatigue properties of pipeline steels. Ronevich et

al. [27] reported an increasing fatigue crack growth rate (FCGR) in X65 pipeline steel exposed to 210 bar H₂ gas [27]. For steels with banded ferrite-pearlite microstructure, the FCGR was lower perpendicular to the bands, attributed to crack branching and limited diffusion in pearlite [27]. In X70 pipeline steel, FCGR was one or two orders of magnitude higher in pressurized H₂ gas than in air [11]. A similar increase in FCGR was reported for X52 and X100 in [28]. An et al. reported an increasing FCGR with increasing H₂ gas pressure and a reduced fatigue life in X80 pipeline steel [10, 26].

2.3 Hydrogen uptake

2.3.1 Uptake from gas

Hydrogen uptake in steels from H₂ gas involves several steps [31, 32]. The first step is transport of a hydrogen molecule to the surface. Molecular adsorption proceeds via Van der Waals forces between a H₂ gas molecule and the steel surface, a process called physisorption. Subsequently, the molecule dissociates and a chemical bond forms between each hydrogen atom and a surface site, known as a chemisorption bond. The direct dissociation reaction is shown in Eq. 2.1 where (M) denotes a surface site and H_{ads} denotes an adsorbed hydrogen atom. The absorption process proceeds as shown in Eq. (2.2), where H_{diss} denotes dissolved hydrogen and [M] denotes an interstitial site in the metal. Eventually, the hydrogen atom diffuses into the bulk.



Sieverts' law

According to Sieverts' law, Eq. (2.3), the hydrogen dissolved in a steel, C_{H} , is proportional to the square root of the hydrogen fugacity, f_{H_2} [33]. S denotes Sieverts' constant. Fugacity can be regarded as the activity of a real gas [34]. Sieverts' law was first deduced empirically but has later been deduced from thermodynamics, as elaborated by Nagumo in [35]. f_{H_2} is commonly assumed to be equal to the hydrogen pressure, p_{H_2} , at pressures below 200 bar at ambient temperature; hence, Sieverts' law is often expressed using p_{H_2} . In well-annealed iron, S is reported to be 5×10^{-4} wppm bar^{-1/2} [36, 37].

$$C_{\text{H}} = S \sqrt{f_{\text{H}_2}} \quad (2.3)$$

Gas impurities

Density functional theory (DFT) simulations have shown that bcc iron surfaces have a catalytic activity that easily dissociates H₂ gas molecules [38]. However, gas impurities, such as O₂ and CO, that have greater attractive force towards the surface can preferentially adsorb and suppress hydrogen dissociation [38, 39]. O₂ and CO gas impurities have also been reported to reduce the susceptibility to HE during mechanical testing [40–43]. Komoda et al. reported that the hydrogen-induced

reduction of the fracture toughness of pipeline steel was completely inhibited with the addition of 100 volume ppm O_2 [42]. Because gas impurities can suppress hydrogen dissociative adsorption, it is essential to use H_2 gas of high purity during gaseous hydrogen charging.

Oxide layer

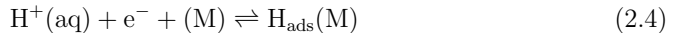
Hydrogen uptake from H_2 gas will be affected by native oxide layers on the surface. Turnbull [13] reported that the hydrogen uptake in oxide-covered steel will depend on the surface coverage of hydrogen atoms, the relative rates of adsorption and desorption, and the relative rates of hydrogen transfer between oxide and steel. The hydrogen diffusion coefficient in an oxide layer can be about 11-12 orders of magnitude lower than in iron [44, 45], which will reduce the rate of hydrogen uptake [13]. Nagao et al. [46] proposed that the energy barrier between the physisorbed and chemisorbed state is higher in the presence of an iron oxide layer. In addition, the chemisorbed state is more stable, such that hydrogen uptake occurs less readily. Their study observed that hydrogen uptake did not occur in two low alloy steels exposed to pressurized H_2 gas at room temperature. However, hydrogen uptake occurred in a stainless steel (API5CT-L80-13Cr) under the same charging conditions, suggesting that the oxide layer's nature is important for the hydrogen uptake [46]. Zhang et al. [47] investigated different oxide films prepared on X80 steel exposed to H_2 gas. They found that the prepared oxides reduced the hydrogen uptake and the degree of HE. The reduced hydrogen uptake was dependent on the oxide properties, such as porosity.

Two methods are commonly used to overcome any surface impedance caused by surface oxides: reduce the oxide layer or apply a Pd coating on the surface. Nagao et al. [46] suggested, based on H_2 permeation at ascending and descending temperature with continuous measurement of permeation flux, that a reduction of oxide layer takes place in H_2 gas at 200 °C. Venezuela et al. [48, 49] performed a surface activation process by applying a high temperature (200 °C) initially during charging and later reduced the temperature to that of interest. Liu et al. [50] initially applied a high H_2 gas pressure (200 bar) to reduce the surface oxide layer before reducing the pressure to the target charging pressure. The reported results indicate that either high temperature or high H_2 gas pressure can be used to reduce an oxide layer. Kumnick and Johnson [51] performed hydrogen permeation tests with H_2 gas charging using a Pd coating on the iron surface exposed to hydrogen gas at room temperature. Using a Pd-coated surface has become a regular practice to determine hydrogen diffusivity in steels using desorption or permeation measurements with H_2 gas charging at room temperature [52, 53]. Nagao et al. [46] investigated the effect of Pd on hydrogen uptake and suggested that Pd reduces the activation energy between the physisorbed and chemisorbed state. In addition, hydrogen entry occurs readily due to a less stable chemisorbed state. However, it was emphasized that Pd only affects the hydrogen entry rate and not the hydrogen flux at steady-state value.

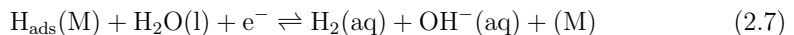
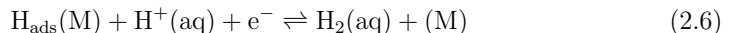
2.3.2 Uptake from electrolyte

Hydrogen uptake from aqueous electrolytes can proceed through a series of reactions [13, 31]. In the Volmer reaction, a hydrogen atom adsorbs onto a metal surface site

through an electrochemical reaction. In acidic solution, the reaction proceeds as shown in Eq. (2.4), while in neutral or basic solution, the reaction proceeds through (2.5).



Several reactions are possible when the hydrogen atom is adsorbed at the surface site. Two adsorbed hydrogen atoms can chemically recombine and desorb as a H_2 gas molecule, the backward reaction of Eq. (2.1). Alternatively, an adsorbed hydrogen atom and a hydrogen cation can react and desorb as a H_2 gas molecule. The reaction is referred to as the Heyrovsky reaction and proceeds as shown in Eq. (2.6) and Eq. (2.7) in acid and basic or neutral electrolyte, respectively. The third alternative is hydrogen absorption into the metal through the same reaction as shown in Eq. (2.2).



The magnitude of hydrogen absorption depends on the relative rates of hydrogen adsorption and recombination of hydrogen to gas molecules [13]. The hydrogen concentration, C_{H} , is reported to be proportional to the square root of the charging current density [37, 54, 55], which has been attributed to a balance between evolved hydrogen and chemical recombination [55]. However, at high cathodic overpotentials, η , an increased influence of electrochemical recombination by the Heyrovsky reaction will lead to a larger fraction of the adsorbed hydrogen to desorb as hydrogen molecules rather than being absorbed [37, 56, 57]. Chemical additives, known as hydrogen recombination poisons, are frequently used in hydrogen charging electrolytes to enhance hydrogen uptake. These additives poison the hydrogen recombination reactions such that a larger fraction of the adsorbed hydrogen absorbs into the material [58].

2.3.3 Equivalent hydrogen charging

Traditionally, electrochemical hydrogen charging has been used to investigate hydrogen-induced material degradation. Advanced lab infrastructure is necessary to expose materials to pressurized H_2 gas due to strict safety requirements. As a result, electrochemical hydrogen charging has been used as a substitute for hydrogen gas exposure when evaluating materials aimed at hydrogen gas applications [13, 59]. The degree of HE is dependent on the C_{H} in the material [14, 30]. Hence, to compare studies using different hydrogen charging conditions, it must be ensured that the induced C_{H} are comparable [16].

Based on Nernst equation for the hydrogen evolution reaction, HER, Bockris and Subramanyan [60] deduced a relationship between f_{H_2} in cavities as a function

of η . η is the difference between the applied and equilibrium potential under standard state conditions. They deduced relationships for different mechanisms of the HER [60]; however, the relationships were not confirmed experimentally. Atrens et al. [16] and Liu et al. [37] further improved the understanding of equivalent charging conditions by determining an equivalent hydrogen fugacity, $f_{\text{H}_2}^{\text{eq}}$, of electrochemical charging conditions based on electrochemical hydrogen permeation and thermodynamic relationships. The deduced relationship between $f_{\text{H}_2}^{\text{eq}}$ and η is shown in Eq. (2.8). The parameters A and ξ depend on the HER mechanism and can be determined experimentally. R and T denotes the gas constant (8.314 kJ mol⁻¹) and temperature, respectively.

$$f_{\text{H}_2} = A \exp\left(-\frac{\eta F}{\xi R T}\right) \quad (2.8)$$

Table 2.1 presents reported values of $f_{\text{H}_2}^{\text{eq}}$ for electrochemical and chemical charging conditions. Kumnick and Johnson [51] reported relationships between gaseous and electrochemical hydrogen charging for iron. They utilized their results from gaseous hydrogen permeation and compared the permeability with reported values from electrochemical hydrogen permeation. Similarly, Oriani and Josephic [61] compared permeability obtained by electrochemical permeation to reported values for gas permeability. The charging performed in 0.1 N NaOH with 10 mg l⁻¹ As₂O₃ with charging current densities in the range 0-0.6 mA cm⁻² were equivalent to fugacities between 20 and 3000 bar at room temperature.

Thermal desorption spectroscopy (TDS) has also been used to investigate the equivalent hydrogen fugacity of electrochemical hydrogen charging conditions [48–50]. The method was first described by Venezuela et al. [48] who measured C_{H} after gaseous or electrochemical hydrogen charging. Based on a Sieverts' relationship determined from gas charged samples, $f_{\text{H}_2}^{\text{eq}}$ of different electrochemical charging conditions were determined. Reported S values at room temperature determined by TDS, are: 2.72×10^{-2} wppm bar^{-1/2} for 3.5NiCrMoV steel [49], 3.6×10^{-3} wppm bar^{-1/2} for martensitic high-strength steel [48] and 2.6×10^{-3} wppm bar^{-1/2} for dual phase steel [50]. Reported values of $f_{\text{H}_2}^{\text{eq}}$ for the same materials range from 1.6 to 5053 bar based on the charging condition [48–50].

Yaktiti et al. [62] determined $f_{\text{H}_2}^{\text{eq}}$ by estimating the f_{H_2} that developed inside porosities in a steel during chemical charging. The charging was performed by immersing samples in a 5 wt% ammonium thiocyanate (NH₄SCN) solution at 50 °C, and the hydrogen content was measured by TDS. $f_{\text{H}_2}^{\text{eq}}$ was between 65 and 88 bar, and the S was 0.022 wppm bar^{-1/2} at 50 °C.

Crolet and Maisonneuve performed a more direct approach [63]. They developed a hollow sensor immersed in an electrolyte that measured the p_{H_2} resulting from electrochemical hydrogen charging. The determined p_{H_2} developed in carbon steel under conditions similar to cathodic protection (5 wt% NaCl, -1100 mV_{SCE}, pH = 6.5) was 5.5 bar. In sour service simulated conditions (5 wt% NaCl, bubbled with H₂S at partial pressures of 1-1000 mbar), p_{H_2} inside the hollow sensor increased with decreasing pH, which at a pH of 4.5 exceeded 350 bar.

The reported results above lacks discussion of transferability to mechanical, HE susceptibility testing. Murakami et al. [59] determined an equivalency between gaseous and electrochemical charging of Inconel 625 and SUS316L in terms of hydrogen uptake by TDS. They performed stress-strain testing after ex-situ gaseous and electrochemical precharging at the same C_H , and found that the behavior were close to identical as shown in Figure 2.2. The conclusion was that electrochemical charging could be used as a substitute for hydrogen gas charging.

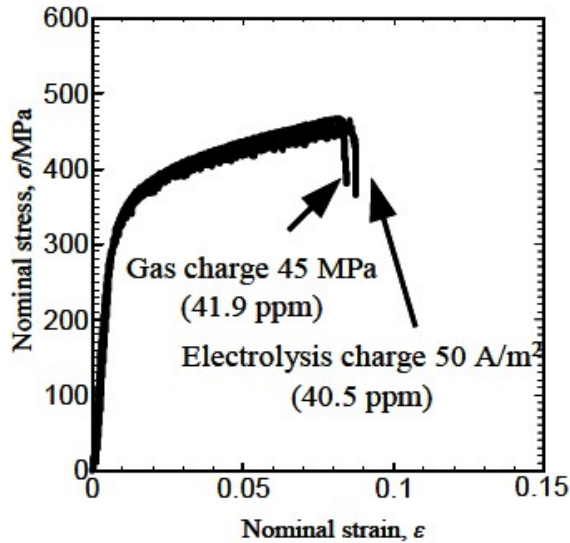


Figure 2.2: Comparison of stress-strain curves of Inconel 625 after ex-situ precharging in high pressure H_2 gas and electrolyte. Reproduced from [59]

Table 2.1: Reported values in the literature of the equivalent hydrogen fugacity. Charging conditions are given as cathodic current density or overpotential.

Method	Material	Charging condition	Equivalent fugacity [bar]	Ref.
Comparing gas and electrochemical permeability	Armco Fe	8.1 mA cm ⁻² 0.1 M NaOH	22	[51]
		8.1 mA cm ⁻² 0.1 M NaOH +0.1 N NaCN	2500	
		10 mA cm ⁻² 0.1 M NaOH +0.1 N KCN	1900	
		0.4 mA cm ⁻² 0.1 N H ₂ SO ₄	540	
	99.9965 Fe	4.5 mA cm ⁻² 1 N H ₂ SO ₄ + 5 g m ⁻³ As ₂ O ₃	1.2 × 10 ⁸	
	99.8 Fe	1.8 mA m ⁻² 0.1 M NaOH	1.1	
	99.8 Ferrovac E	11.3 mA m ⁻² 0.1 M NaOH	29	
	99.5 Fe	- Distilled H ₂ O	5.7 × 10 ⁻⁵	
	AISI 1045	0-0.6 mA cm ⁻² 0.1 N NaOH + 10 mg l ⁻¹ As ₂ O ₃	20-3000	[61]
	Electrochemical permeation	ULCS ^a	-357 to -755 mV 0.1 M NaOH	1500-4500
-883 to -1385 mV 0.1 M Na ₂ SO ₄ (pH = 2)			90-280	
TDS	3.5NiCrMoV	-145 to -845 mV 0.1 M NaOH	10-50	[48, 49]
		-322 to -922 mV 0.1 M Na ₂ SO ₄ (pH=2)	30-680	
	MAHSS ^b	-269 to -869 mV 0.1 M NaOH	523-5053	[48]
		-46 to -399 mV 3.5 wt% NaCl	1.9-136	
	980 DP ^c	-257 to -857 mV 0.1 M NaOH	1129-2702	[50]
		-39 to -322 3.5 wt% NaCl	1.6-126	

Continuation of Table 2.1

Method	Material	Charging condition	Equivalent fugacity [bar]	Ref.
Porosity +TDS	LACS	- 5 wt% NH ₄ SCN aqueous solution 50 °C	65-88	[62]
Hollow sensor	CS ^e	-958 mV 5 wt% NaCl (pH = 6.5)	5.5	[63]
		- 5 wt% NaCl +H ₂ S bubbling, (pH = 6.5)	3-8	
		- -5 wt% NaCl +H ₂ S bubbling (pH = 5.5)	110-250	
		- -5 wt% NaCl +H ₂ S bubbling (pH = 4.5)	>>350	

^a Ultra Low carbon steel

^b Martensitic advanced high-strength steel

^c Dual phase steel

^d Low alloy cast steel

^e Carbon steel

2.4 Hydrogen diffusivity

2.4.1 Lattice diffusivity

In bcc steels, lattice diffusion at ambient temperature proceeds by jumping between tetrahedral sites, while at elevated temperatures, octahedral sites are also filled [36]. For diffusion through a thin plate where the concentrations at both sides are kept constant and where hydrogen does not accumulate in the plate, the diffusion can be described by Fick's 1st law of diffusion [64]. Fick's first law of diffusion states that the flux of diffusion species, J , is proportional to the concentration gradient, dC/dx , as shown in Eq. (2.9) [64].

$$J = -D \frac{dC}{dx} \quad (2.9)$$

Under nonsteady-state conditions, where dC/dx and J at a particular position are changing with time, which leads to an accumulation or depletion of the diffusing

species, Fick's 2nd law of diffusion can be used [64]. When the diffusion coefficient is independent of composition, Fick's 2nd law can be expressed as shown in Eq. (2.10).

$$\frac{\delta C}{\delta t} = D \frac{\delta^2 C}{dx^2} \quad (2.10)$$

Diffusion follows an Arrhenius relation, as shown in Eq. (2.11), where E_d denotes the activation energy of diffusion and D_0 is a pre-exponential factor. Kiuchi and McLellan [36] evaluated a large number of reported data for hydrogen solubility and diffusivity in annealed iron, and their deduced relationship is often quoted as the lattice diffusion in iron. Between -40 and 80 °C, D_0 is $7.23 \times 10^{-4} \text{ cm}^2 \text{ s}^{-1}$, and E_d is 5.69 kJ mol^{-1} , which represents the activation energy necessary to jump between two tetrahedral sites.

$$D = D_0 \exp\left(-\frac{E_d}{RT}\right) \text{ cm}^2 \text{ s}^{-1} \quad (2.11)$$

2.4.2 Effective diffusivity

Hydrogen will have a longer residence time in some lattice defects compared with interstitial sites [65]; hence, trapping of hydrogen in such defects will slow down the transport of hydrogen. The residence time in a trap will depend upon the binding energy, E_b , which will vary between different trap sites. When the hydrogen transport through a metal is affected by trapping, the diffusion coefficient will be an effective value, D_{eff} [66]. If the fraction of occupied traps is low, the effective hydrogen diffusivity can be represented by Fick's laws of diffusion, and D_{eff} will have a lower value than lattice diffusion coefficient, D_L [13]. However, if under nonsteady-state conditions, the trap occupancy becomes significant, then D_{eff} will appear to change with time and no longer has a theoretical basis in Fick's 2nd law [13]. The effective diffusivity depends on the trap density and E_b of the trap sites [66, 67]. Because the trap occupancy is dependent on the lattice hydrogen concentration, D_{eff} is dependent on C_H [68]. Examples of trap sites are dislocations, grain boundaries, vacancies, and particle-matrix interfaces [69–72]. An illustration of lattice defects which can act as hydrogen trapping sites are shown in Figure 2.3 [73]. Trap sites are often classified as reversible versus irreversible or weak versus strong depending on the binding energy or hydrogen residence time; however, there are no strict cut-off values [13].

Effective diffusivity in pipeline steels

Hydrogen diffusivity in pipeline steel is typically investigated by hydrogen permeation or desorption methods, which will be explained in detail in Chapter 3. Reported effective diffusivities in X65 pipeline steels contain discrepancies, where the scatter in D_{eff} is about two orders of magnitude between 1.5×10^{-7} and $2 \times 10^{-5} \text{ cm}^2 \text{ s}^{-1}$ [74–78]. E_d is reported to be 25.5 and 32.2 kJ mol^{-1} for X65 and X60 pipeline steels, respectively [52, 79]. The higher E_d compared to that of well-annealed iron is attributed to trap sites increasing the energy barrier for hydrogen diffusion. Hydrogen diffusivity is higher in ferrite than in pearlite; hence, in banded ferritic-pearlitic microstructures, the pearlite grains can cause a tortuous diffusion path, and the

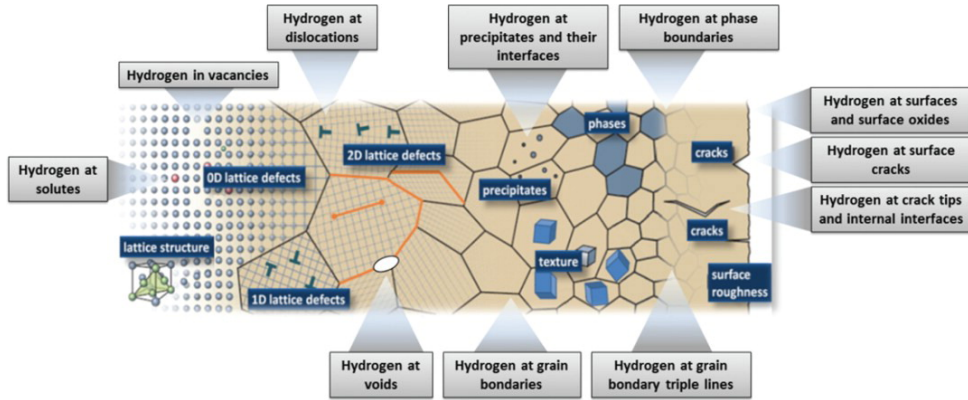


Figure 2.3: Illustration of potential hydrogen trapping sites. Reproduced from [73].

diffusivity will be higher parallel to the banded direction than perpendicular to the banded direction [80, 81].

Chapter 3

Experimental

3.1 Materials

The three X65 pipeline steels investigated during this PhD project were characterized in the initial stage of the HyLINE project by other work packages. The main results have been summarized in a technical report [82], presentations [83, 84], and publications [85–87] during the course of the project, and the main findings are presented in this section.

3.1.1 Vintage

The steel, denoted as Vintage, is from a hot rolled and arc-welded steel pipe. The chemical composition is listed in Table 3.1. The wall thickness was 26 mm. Figure 3.1 shows scanning electron microscope (SEM) micrographs of the Vintage steel. The microstructure mainly consists of polygonal ferrite and some pearlite and bainite. The phase volume of ferrite is approximately 83-87%, while the combined phase volume of pearlite and bainite is approximately 13-17%. The optical micrographs shown in Figure 3.2 reveal a banded appearance, which is most prominent towards the inner and outer surfaces. The average grain sizes are 3.7, 4.2, and 3.5 μm in the inner, middle, and outer positions, respectively. The yield strength is 450 MPa, and the ultimate tensile strength is 577 MPa.

Table 3.1: Chemical composition of the Vintage steel.

Element	C	Si	Mn	P	S	Cu	Cr
wt%	0.1	0.15	<1.6	<0.025	<0.015	<0.25	<0.25
Element	Ni	Mo	V	Nb	Ti	N	Fe
wt%	<0.25	<0.05	<0.1	<0.05	<0.02	<0.01	Bal.

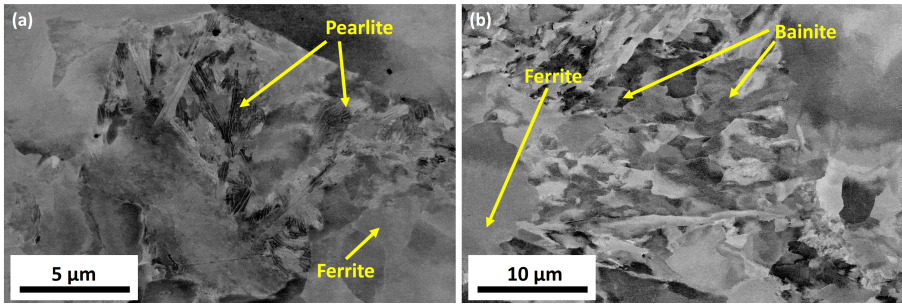


Figure 3.1: SEM micrographs of the Vintage steel, as included in Paper 1.

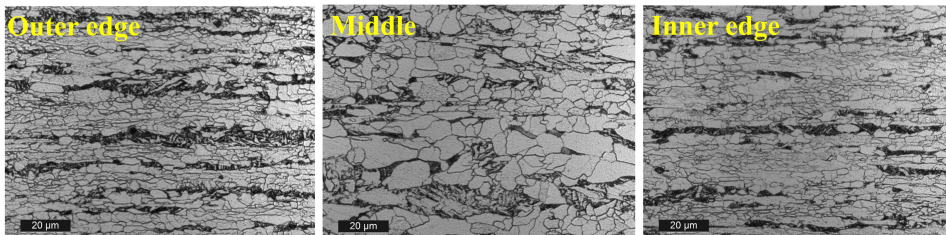


Figure 3.2: Optical micrographs of the outer, middle, and inner positions of the Vintage steel. The cross section is parallel to the longitudinal direction. Adapted from [82, 84].

3.1.2 Modern QT

The steel, denoted as Modern QT, is a quenched and tempered steel from a seamless pipe. The chemical composition of the QT steel is listed in Table 3.1. The wall thickness was 15.4 mm. Figures 3.3 and 3.4 show the microstructure of the Modern QT steel characterized by SEM (BSE - Backscattered electron, ECCI - Electron channeling contract image, IPF - Inverse pole figure, IQ - image quality, KAM - Kernel average misorientation) and optical microscope (OM). The microstructure consists of homogeneously distributed ferrite and bainite grains. The phase volume of ferrite differs between 76% in the outer part and 89% in the inner part. The grain size is approximately 7 μm. The yield strength is 474 MPa, and the ultimate tensile strength is 564 MPa.

Table 3.2: Chemical composition of the Modern QT steel.

Element	C	Si	Mn	P	S	Cu	Cr
wt%	0.07	0.23	1.17	0.01	0.002	0.14	0.17
Element	Ni	Mo	V	Nb	Ti	N	Fe
wt%	0.15	0.13	0.03	0.02	0.002	0.07	Bal.

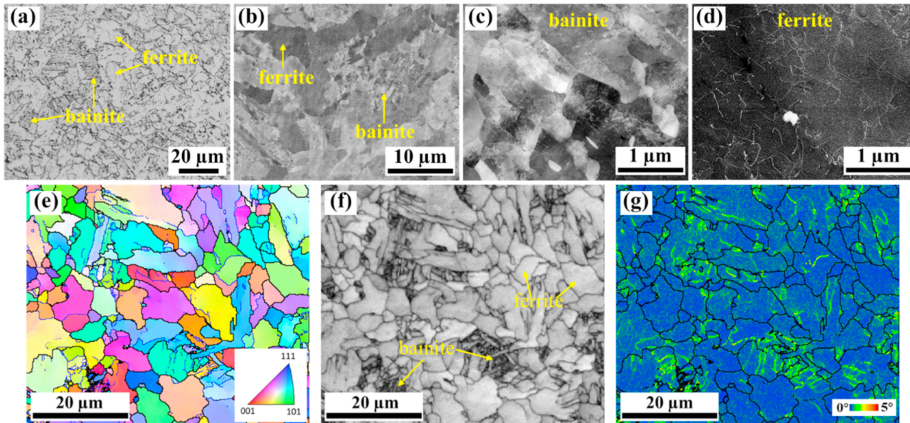


Figure 3.3: Microstructure of the Modern QT steel. Reproduced from [85].”The optical microscopy image (a) and BSE image (b) showing the overall matrix. (c) and (d) are ECCI showing detailed information of bainite and ferrite, respectively. (e–f) are IPF map, IQ map and KAM map in a same area, respectively.”

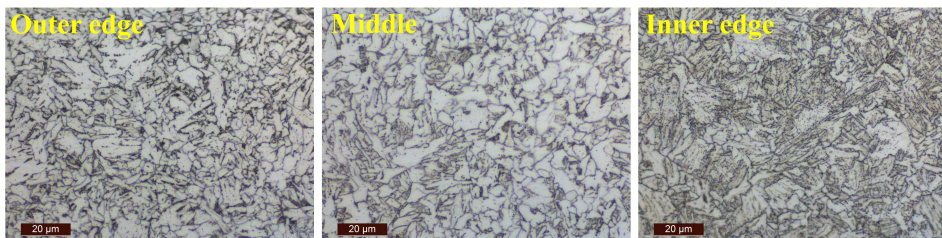


Figure 3.4: Optical micrographs of the outer, middle, and inner positions of the Modern QT steel. The cross section is parallel to the longitudinal direction. Adapted from [82, 84].

3.1.3 Modern TMCP

The steel, denoted as Modern TMCP, is a thermo-mechanical controlled processed steel. The chemical composition is listed in Table 3.1. Figures 3.5 and 3.6 show the SEM and OM characterization of the Modern TMCP steel, respectively. The microstructure consists of ferrite and bainite. The phase volume of ferrite and bainite is approximately 76% and 24%, respectively. The average ferrite grain size is about $12.8 \mu\text{m}$. The yield strength is 407 MPa, and the ultimate tensile strength is 502 MPa.

Table 3.3: Chemical composition of the Modern TMCP steel.

Element	C	Si	Mn	P	S	Cu	Cr
wt%	0.04	0.3	1.45	0.011	0.001	0.23	0.04
Element	Ni	Mo	V	Nb	Ti	N	Fe
wt%	0.267	0.01	0.002	0.042	0.014	?	Bal.

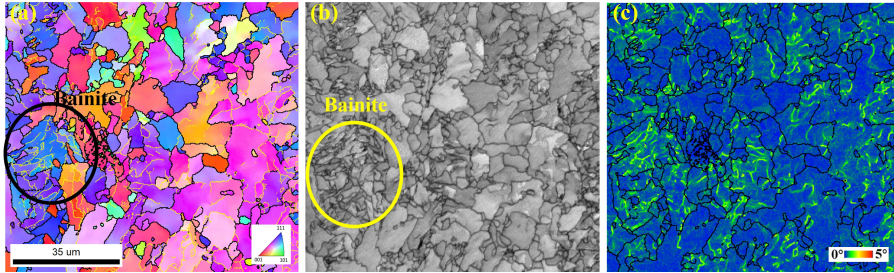


Figure 3.5: SEM characterization of the Total material. (a)IPF map, (b)IQ map and (c) KAM map of the same area. Adapted from [84].

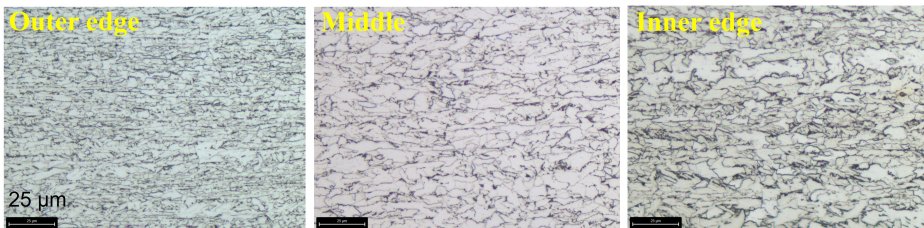


Figure 3.6: Optical micrographs of the outer, middle, and inner positions of the Modern TMCP steel. The cross section is parallel to the longitudinal direction. Adapted from [84].

3.2 Hydrogen permeation

The hydrogen permeation technique was first described by Devanathan and Stachurski [88]. They used a double electrochemical cell consisting of one charging compartment and one detection compartment, which were separated by the sample. The hydrogen permeation technique has been standardized in the ISO 17081(2014) [89] and the ASTM G148-97(2018) [90]. In this technique, hydrogen is introduced to the sample in the charging compartment. It diffuses through the sample and is detected as it reaches the sample's surface in the detection chamber. The most common detection method is to apply an anodic potential to oxidize the hydrogen atoms reaching the exit side of the sample. The measured oxidation current density, or permeation current density, is a measure of the hydrogen flux through the sample. Solutions to Fick's laws of diffusion can be used to estimate the diffusion coefficient and the sub-surface hydrogen concentration. In the charging chamber, different types of hydrogen charging can be utilized, e.g., gaseous and electrochemical charging. The most common charging method is electrochemical hydrogen charging due to its ease of application [91].

3.2.1 Sample preparation

Samples were machined parallel to the longitudinal direction from a position close to the inner side of the pipe wall. Samples used for electrochemical permeation were disks with a diameter of 30 mm. The thickness of the disks used was between 1.0 and

1.9 mm. Samples used for gas permeation were plates with dimensions of $50 \times 150 \times 1.9$ mm (width \times length \times thickness). Both sides of the samples were ground with SiC grinding papers to a final grade of #P1000 grit. A Pd-coating was applied to the detection side of the samples to ensure complete oxidation of hydrogen atoms [92]. The Pd-coating was applied by electroplating following the method used by Husby et al. [93]. For gas permeation, the samples were also coated with Pd on the charging side. As discussed in Section 2.3.1, hydrogen uptake from hydrogen gas can be impeded because of an oxide layer on the surface, and in such case, a Pd-coating can facilitate hydrogen uptake [46, 53]. Pd plating was not considered necessary on the charging side during electrochemical permeation, as a reduction of the oxide layer would occur under cathodic conditions.

3.2.2 Electrochemical permeation

An image of the permeation cell used for electrochemical hydrogen permeation is shown in Figure 3.7. The exposed sample area was 3.7 cm^2 . In the detection chamber, the electrolyte was a 0.1 M NaOH solution ($\text{pH} = 12.6$), and a $\text{Hg}/\text{Hg}_2\text{SO}_4$ (sat. K_2SO_4) electrode was used as the reference electrode. The electrolyte was continuously purged with N_2 gas. A potential of $-80 \text{ mV}_{\text{Hg}/\text{Hg}_2\text{SO}_4}$ ($+315 \text{ mV}_{\text{SCE}}$) was applied to oxidize the hydrogen diffusing through the sample. Pt-sheets were used as counter electrodes in both chambers. During stabilization of the permeation current density, i_p , the charging chamber was purged with N_2 gas to avoid oxidation of the sample. Once the i_p stabilized below $0.1 \mu\text{A cm}^{-2}$, the electrolyte was added to the charging chamber, and the N_2 gas purging was terminated. Different electrochemical charging conditions were used in this work. Both galvanostatic and potentiostatic charging were conducted, and the specific values are specified in each paper and report. The electrolytes that have been used are:

- A 3.5 wt% sodium chloride (NaCl) solution. The 3.5 wt% NaCl solution was also used with the addition of thiourea ($\text{CH}_4\text{N}_2\text{S}$) with various concentrations ($0.5\text{--}3 \text{ g l}^{-1}$).
- A 0.1 M sodium sulfate (Na_2SO_4) solution.
- A glycerol ($\text{C}_3\text{H}_8\text{O}_3$) based solution containing 600 g l^{-1} borax (sodium tetraborate decahydrate) and 0.002 M sodium thiosulfate ($\text{Na}_2\text{S}_2\text{O}_3$). The solution was diluted with 20% distilled water to enhance conductivity. The solution was denoted as GBST.

The method described above was used for both complete transient and partial transients. The complete and partial permeation transient methods are illustrated in Fig 3.8. For complete transients, the charging was terminated once a steady-state permeation current density, i_p^∞ , was obtained. The cell was then dismantled, and the sample was kept in a desiccator overnight. The charging side of the sample was ground to remove any corrosion products before a new complete transient was performed. Three complete transients were performed per test. In stepwise partial transients experiments, when the i_p^∞ was reached, the charging current density or applied potential was changed while continuously measuring i_p . Both build-up and decay partial transients were performed.

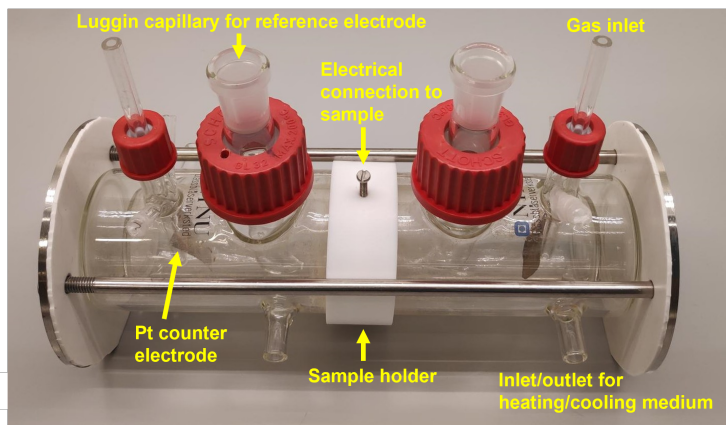


Figure 3.7: Image of the electrochemical permeation cell.

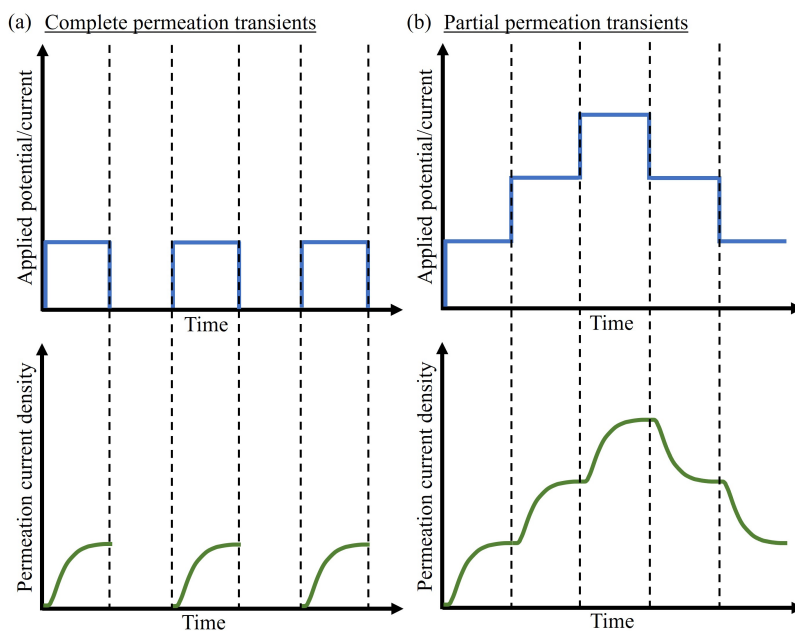


Figure 3.8: Illustration of the magnitude of applied cathodic potential or current density and the response signal of the permeation current density as a function of time for (a) Complete permeation transients and (b) Partial permeation transients.

3.2.3 Gas permeation

An image of the permeation cell used for hydrogen gas permeation is shown in Figure 3.9. The exposed sample area was 16 cm^2 . Similar to electrochemical permeation, a 0.1 M NaOH solution ($\text{pH} = 12.6$) was used as the electrolyte in the detection chamber. An Ag/AgCl (sat. KCl) electrode was used as the reference. A potential

of $+360 \text{ mV}_{\text{Ag}/\text{AgCl}}$ ($+315 \text{ mV}_{\text{SCE}}$) was applied. Once the i_p was stable, hydrogen gas was introduced into the charging autoclave. Three different charging pressures were used: 10, 50, and 100 bar. Three charging and discharging cycles were performed while keeping the sample in the cell.

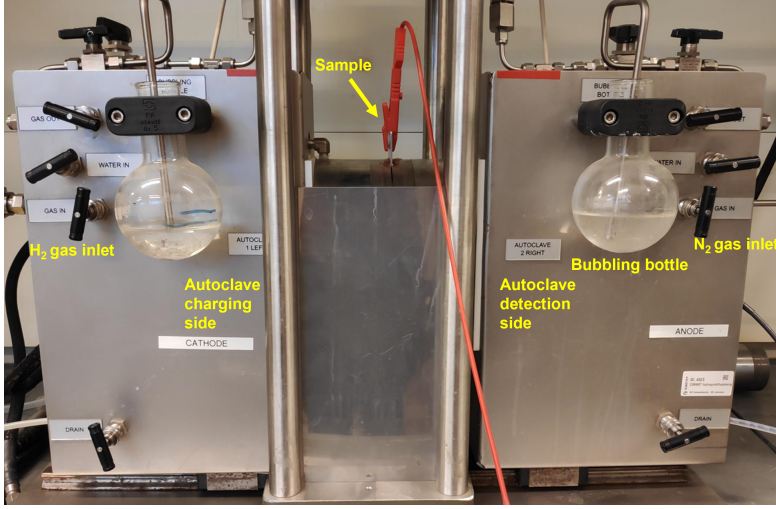


Figure 3.9: Image of the gas permeation cell.

3.2.4 Analysis

Complete transients

The effective diffusion coefficient, D_{eff} , was determined using the breakthrough time method and the time lag method [89, 90, 94]. The breakthrough time, t_b , is defined as the intercept between an extrapolation of the linear region of the permeation transient and the time-axis. D_{eff} determined by the t_b method is denoted as $D_{\text{eff}}(t_b)$, and was calculated using Eq. (3.1) where L denotes the thickness of the sample. The time lag, t_{lag} , is defined as the time it takes to reach a permeation current value equal to 63% of i_p^∞ . $D_{\text{eff}}(t_{\text{lag}})$ was calculated using Eq. (3.2).

$$D_{\text{eff}}(t_b) = \frac{L^2}{19.8t_b} \quad (3.1)$$

$$D_{\text{eff}}(t_{\text{lag}}) = \frac{L^2}{6t_{\text{lag}}} \quad (3.2)$$

The sub-surface hydrogen concentration in lattice and reversible trap sites, C_{0R} was calculated using Eq. (3.3) [89].

$$C_{0R} = \frac{Li_p^\infty}{D_{\text{eff}}} \quad (3.3)$$

Stepwise partial transients

For stepwise partial permeation transients, analytical solutions of Fick's 2nd law of diffusion were fit to the obtained data. The build-up and decay transients were fitted to Eq. (3.4) and Eq. (3.5), respectively. t denotes time and i_p^0 denotes the starting value of i_p [95].

$$\frac{i_p - i_p^0}{i_p^\infty - i_p^0} = \frac{2L}{\sqrt{\pi Dt}} \sum_{n=0}^{\infty} \exp\left(-\frac{(2n+1)^2 L^2}{4Dt}\right) \quad (3.4)$$

$$\frac{i_p - i_p^\infty}{i_p^0 - i_p^\infty} = 1 - \frac{2L}{\sqrt{\pi Dt}} \sum_{n=0}^{\infty} \exp\left(-\frac{(2n+1)^2 L^2}{4Dt}\right) \quad (3.5)$$

3.3 Hydrogen desorption

3.3.1 Diffusivity

Cylindrical samples with a length of 19 mm were used in this test. The diameter was 19 mm for the Vintage and Modern TMCP steels and 15 mm for the Modern QT steel due to lower wall thickness. Large samples ensure a diffusion-limited process, and that the measured hydrogen content is not size dependent [53]. The samples were ground to a finish of #P600 grit paper and coated with Pd using ion sputtering. H₂ gas charging was performed in a high-pressure H₂ pressure vessel at 85 °C and 1000 bar. 85 °C has been reported to ensure hydrogen uptake during charging in H₂ gas in cases where hydrogen uptake at room temperature is limited [46, 53]. After charging, the samples were stored in liquid nitrogen to avoid unwanted hydrogen desorption. A gas chromatography-mass spectrometer (GC-MS) was used to detect the desorbed hydrogen.

Two methods were employed to determine diffusivity from desorption measurements. One method, denoted as in-situ desorption, involved placing charged samples in the furnace connected to the GC-MS, holding the temperature constant, and continuously measuring the desorbing hydrogen content. In the method denoted as ex-situ desorption, several charged samples were kept at constant temperature in a thermostatic chamber. The samples were kept for different holding times, and subsequently, the residual hydrogen content in the sample was measured by GC-MS by heating the sample at a heating rate of 100 °C/h. A schematic of the two methods is shown in Figure 3.10. In both methods, the effective diffusion coefficient was determined by fitting the desorption data of residual diffusible hydrogen concentration, C_{HD} , as a function of holding time, t_R to a three-dimensional solution of Fick's 2nd law, Eq. (3.6) [53, 96, 97]. A is a constant that accounts for hydrogen that desorbs in the dwell time before GC-MS analysis. β_m is the root of the zero-order Bessel function, while L and r are the length and radius of the cylindrical samples, respectively. More detailed descriptions can be found in [53, 96, 97].

$$C_{\text{HD}} = A \frac{32}{\pi^2} \times \sum_{n=0}^{\infty} \frac{\exp \left[-\frac{(2n+1)^2 \pi^2 D t_{\text{R}}}{L^2} \right]}{(2n+1)^2} \times \sum_{m=1}^{\infty} \frac{\exp \left[-\frac{D \beta_m t_{\text{R}}}{r^2} \right]}{\beta_m^2} \quad (3.6)$$

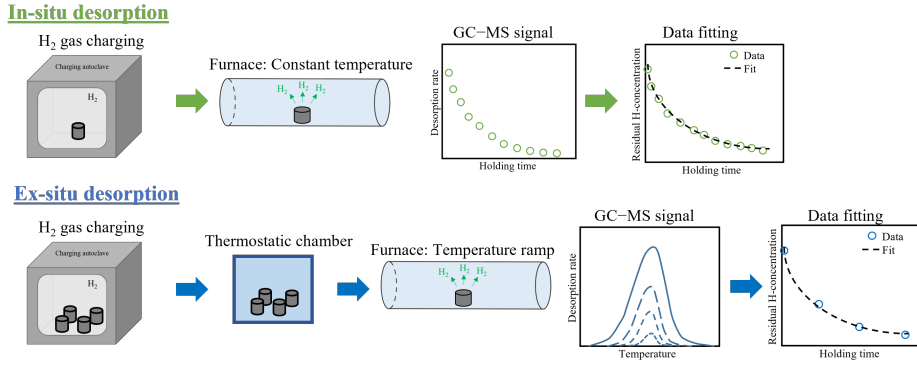


Figure 3.10: Schematic of the in-situ and ex-situ hydrogen desorption tests to determine the hydrogen diffusivity.

3.3.2 Hot extraction

Hot extraction was performed to measure the hydrogen content of electrochemically charged samples. The samples were plates with dimensions $10 \times 15 \times 2$ mm (width \times length \times thickness). The analysis was performed using a Bruker G4 Phoenix, as shown in Figure 3.11, in combination with an InProcess Instrument mass spectrometer. The hydrogen charging was performed in a beaker with a Pt counter electrode. The samples were charged in 3.5 wt% NaCl, 0.1 M Na₂SO₄, and GBST solution. After charging, the samples were immediately removed from the electrolyte, rinsed in distilled water and ethanol, and quickly dried. The samples were inserted into a pre-heated furnace, which was kept at a constant temperature of 600 °C. The dwell time between charging and hot extraction analysis was approximately 2 minutes. A short dwell time is desirable to avoid hydrogen desorption before the analysis.

3.3.3 Choo-Lee method

The Choo-Lee method [72], which is based on the work by Kissinger [98], was utilized to determine trap binding energies, E_b . Disk samples with a thickness of 2 mm were used in this test. The diameter was 19 mm for the Vintage and Modern TMCP steels and 15 mm for the Modern QT steel. The samples were ground with SiC grinding papers until #P600 grit. Charging was performed in a high-pressure H₂ pressure vessel at 1000 bar and 85 °C. The samples were stored in liquid nitrogen between charging and analysis. The desorbing hydrogen was measured by GC-MS at four different heating rates, α : 50, 100, 150, and 200 °C/h.

The desorption spectrum (desorption rate vs. temperature) at each α was analyzed to determine the peak temperatures, T_p . The de-trapping activation energy, E_a , was



Figure 3.11: Image of the Bruker G4 Phoenix that was used for hot extraction.

calculated according to Eq. (3.7) [72, 99]. E_a was determined from the slope of a plot of $\ln(T_p^2/\alpha)$ versus $(1/T_p)$. E_b can be approximated as E_a minus the activation energy of hydrogen jumping between lattice sites (5.69 kJ mol^{-1} [36]) [100].

$$\frac{\delta \ln(T_p^2/\alpha)}{\delta(1/T_p)} = \frac{E_a}{R} \quad (3.7)$$

3.3.4 Effect of Pd coating

Cylindrical samples of the Modern QT and Vintage steels were used to investigate the effect of Pd coating on hydrogen uptake in H_2 gas at room temperature. The thickness was 12 mm. The diameter was 19 mm and 15 mm for the Vintage and Modern QT steels, respectively. The samples were ground with SiC paper to a finish of #P600 grit. Half of the samples were coated with Pd by ion sputtering, while the other half remained uncoated. The charging was performed at room temperature and two H_2 charging pressures were applied: 100 and 1000 bar. After charging, the samples were stored in liquid nitrogen. The hydrogen concentration was measured using GC-MS at a heating rate of $100 \text{ }^\circ\text{C/h}$.

Chapter 4

Summary of publications and report

Three scientific papers and one report containing unpublished data were written to realize this PhD project's main objectives. In **Paper 1**, the objective of developing a method to determine a relationship between gaseous and electrochemical charging was accomplished by performing hydrogen permeation with both charging methods. In **Paper 2**, the method developed in Paper 1 was utilized to fulfill the objective of determining an electrochemical charging condition that produces the same hydrogen concentration as a H₂ gas pressure relevant to hydrogen transport. **Paper 3** aimed to compare permeation and desorption techniques focusing on hydrogen diffusivity. The objective of investigating microstructural differences and their effect on hydrogen uptake, diffusion, and trapping was mainly handled in the **Report** and **Paper 3**.

A summary of each paper and the report are given in the following sections.

4.1 Paper 1

Experimental comparison of gaseous and electrochemical hydrogen charging in X65 pipeline steel using the permeation technique

The aim of this study was to compare the hydrogen uptake and diffusivity determined by permeation using different hydrogen sources. The emphasis was put on determining a relationship between gaseous and electrochemical charging.

Hydrogen permeation was performed using both gaseous and electrochemical hydrogen charging on the Vintage steel. Gaseous permeation was performed at 10, 50, and 100 bar. A Pd coating was used on the charging side of the sample during gas permeation to overcome any surface impedance caused by the presence of an oxide layer. Electrochemical permeation was conducted in a 3.5 wt% NaCl solution, at charging current densities of -1 , -15 , and -50 mA cm⁻². Partial permeation transients were also performed by stepwise increasing the charging current density. All tests were performed at room temperature.

The method to determine an equivalency between gaseous and electrochemical

charging was based on the assumption that charging conditions are equivalent if they produce the same sub-surface hydrogen concentration in lattice and reversible trap sites, C_{0R} . A good measure of the hydrogen diffusivity is necessary to determine C_{0R} by hydrogen permeation. The determined effective diffusion coefficient, D_{eff} , by the time lag, t_{lag} , method were all larger than the ones determined by the breakthrough time, t_b , method. In addition, the normalized permeation transients were steeper than the normalized permeation transient predicted by Fick's 2nd law of diffusion. These are indications that significant reversible causes an increasing effective diffusivity during the permeation transients. Under such conditions, the use of t_{lag} and t_b methods does not have a theoretical basis in Fick's 2nd law of diffusion. Stepwise partial permeation transients were performed to determine D_{eff} where the effect of trap occupancy is limited because of a smaller perturbation of the equilibrium between lattice and reversibly trapped hydrogen. The partial permeation transients obtained good fits with the analytical solutions of Fick's 2nd law. Thus, D_{eff} determined by partial permeation transients, $1.6 \times 10^{-6} \text{ cm}^2 \text{ s}^{-1}$, was used to calculate C_{0R} .

Sieverts' constant, S , was determined by plotting C_{0R} obtained by gas permeation versus the square root of the hydrogen fugacity, f_{H_2} , which obtained a good linear fit. The value of S was $0.0125 \text{ wppm bar}^{-1/2}$. The equivalent hydrogen fugacity, $f_{\text{H}_2}^{\text{eq}}$, was determined by inserting the C_{0R} determined by electrochemical permeation into the relationship deduced for Sieverts' law and solving for f_{H_2} . A relationship was deduced between $f_{\text{H}_2}^{\text{eq}}$ and the overpotential, η . Electrochemical charging in 3.5 wt% NaCl solution at -1 , -15 , and -50 mA cm^{-2} were equivalent to f_{H_2} of 49.1, 101.9 and 222.7 bar, respectively.

4.2 Paper 2

Investigation electrochemical charging conditions equivalent to hydrogen gas exposure of X65 pipeline steel

The objective of this work was to utilize the method developed in Paper 1 to systematically determine an electrochemical charging condition equivalent to a H_2 gas pressure relevant for potential H_2 gas transportation in pipelines with 200 bar pressure.

The material investigated was the Modern QT steel. Gas permeation was performed at 10, 50, and 100 bar H_2 gas pressure. Electrochemical permeation was performed in a 3.5 wt% NaCl solution at different applied cathodic potentials (-1050 to $-1275 \text{ mV}_{\text{Ag}/\text{AgCl}}$). Thiourea ($\text{CH}_4\text{N}_2\text{S}$), a hydrogen recombination poison, was added in various concentrations (0.5 – 3 g l^{-1}).

Initially, stepwise partial permeation transients were performed to determine D_{eff} , which was $2.3 \times 10^{-6} \text{ cm}^2 \text{ s}^{-1}$. D_{eff} was used to calculate C_{0R} for both gaseous and electrochemical permeation. C_{0R} was proportional to f_{H_2} , and the determined S was $0.0095 \text{ wppm bar}^{-1/2}$. Cathodic protection (CP) simulated conditions, $-1050 \text{ mV}_{\text{Ag}/\text{AgCl}}$ in a 3.5 wt% NaCl solution, was used as the initial condition to determine the equivalent pressure, $p_{\text{H}_2}^{\text{eq}}$. $p_{\text{H}_2}^{\text{eq}}$ of the CP simulated condition was 12.3 bar, which was well below the desired pressure of 200 bar. To increase $p_{\text{H}_2}^{\text{eq}}$, thiourea was added to

the solution. $p_{\text{H}_2}^{\text{eq}}$ as a function of thiourea concentration went through a maximum at 2 g l^{-1} , which corresponded to a $p_{\text{H}_2}^{\text{eq}}$ of 111.5 bar. To further increase $p_{\text{H}_2}^{\text{eq}}$, the applied potential was changed in the cathodic direction in steps of 75 mV until a $p_{\text{H}_2}^{\text{eq}}$ above 200 bar was reached. The relationship for $f_{\text{H}_2}^{\text{eq}}$ as a function of η was solved for 227.2 bar (equivalent to 200 bar p_{H_2}), which was $-1225 \text{ mV}_{\text{Ag}/\text{AgCl}}$. To confirm that a $p_{\text{H}_2}^{\text{eq}}$ of 200 bar could be obtained under those conditions, a permeation test in 3.5 wt% NaCl solution with addition of 2 g l^{-1} thiourea at $-1225 \text{ mV}_{\text{Ag}/\text{AgCl}}$ was performed. The obtained $p_{\text{H}_2}^{\text{eq}}$ was 201.9 bar.

4.3 Paper 3

Hydrogen diffusivity in X65 pipeline steel: Desorption and permeation studies

This work was performed with the objective of comparing the diffusion properties of X65 pipeline steels, which were conducted using permeation and desorption methods. There is a large scatter in diffusivity values reported for X65 pipeline steels, and an aim was to look into reasons for the large scatter, such as techniques, charging conditions, and microstructural differences.

Hydrogen diffusivity in the Vintage and Modern QT steels was investigated by desorption and permeation methods. Hydrogen samples for desorption methods were charged in H_2 gas at 1000 bar and $85 \text{ }^\circ\text{C}$. Hydrogen desorption was performed by keeping the samples at constant temperatures, which were 25, 50, and $75 \text{ }^\circ\text{C}$ during in-situ desorption and -2 and $24 \text{ }^\circ\text{C}$ during ex-situ desorption. Electrochemical permeation was performed by both complete and partial transients in a 3.5 wt% NaCl. Three subsequent complete transients were performed at a current density of -1 mA cm^{-2} at 7, 21, 50, and $75 \text{ }^\circ\text{C}$. Partial decay and build-up transients between -0.5 and -1 mA/cm^2 were conducted at 7, 21, and $50 \text{ }^\circ\text{C}$. Partial build-up transients were performed at $21 \text{ }^\circ\text{C}$ in the following steps: -0.5 to -1 , -1 to -1.5 , and -1.5 to -2 mA cm^{-2} .

Both the desorption and permeation methods revealed strong traps where hydrogen has a long residence time in the Vintage steel. Increasing the temperature reduced the significance of strong trapping due to a reduction in residence time. For the Vintage steel, strong traps caused a poor fit of the desorption data to the solution of Fick's 2nd law of diffusion. A term representing the strongly trapped hydrogen was added to the solution of Fick's 2nd law. The modified equation fit the desorption data well, and the diffusivity results were in good agreement between ex-situ and in-situ hydrogen desorption. Partial permeation transients with stepwise increasing charging current density revealed that D_{eff} of the Vintage steel increased with current density. In contrast, D_{eff} was independent of the charging current density in the Modern QT steel. At room temperature, the determined D_{eff} for all the methods in the Modern QT steel was between 8.56×10^{-7} and $2.70 \times 10^{-6} \text{ cm}^2 \text{ s}^{-1}$, while in the Vintage steel between 1.95×10^{-7} and $3.34 \times 10^{-6} \text{ cm}^2 \text{ s}^{-1}$. The larger scatter in D_{eff} observed in the Vintage steel compared with the Modern QT steel was attributed to tortuosity effects which can be caused by the banded ferrite-pearlite layers. A tortuosity effect is likely more prominent in the thin samples used in permeation tests than in the large samples

used for desorption tests where three-dimensional diffusion was assumed. In addition, different charging conditions were used for permeation and desorption tests, and an effect of multiple dominant trap sites could cause the concentration-dependency of D_{eff} .

Trap binding energies, E_b , and trap density, N_T , of the Vintage and Modern QT steel were estimated from the diffusivity results. For the Modern steel E_b was 28.2 and 28.9 kJ/mol, and for the Vintage steel, 26.0 and 20.4 kJ/mol, determined by desorption and partial permeation methods, respectively. N_T was 1.1×10^{20} and 9.3×10^{19} sites/cm³ in the Modern QT steel and 3.6×10^{20} and 1.7×10^{22} sites/cm³ in the Vintage steel. E_b and N_T determined from diffusivity tests will represent the most dominant trap site but can be influenced by multiple trap sites if several sites are present.

4.4 Report

The report contains the unpublished results obtained during the PhD project.

Electrochemical hydrogen charging was performed in three different electrolytes: 3.5 wt% NaCl, 0.1 M Na₂SO₄, and glycerol-borax solution containing sodium thiosulfate (GBST), which is a hydrogen recombination poison. The electrochemical charging conditions were applied to both permeation tests and samples used for hot extraction analysis. Samples used for the Choo-Lee method were charged at 85 °C and 1000 bar H₂ gas. Samples used to study the effect of Pd on hydrogen uptake were charged at room temperature and pressures of 100 and 1000 bar H₂ gas.

The charging condition utilized significantly affected the hydrogen uptake measured by both hot extraction test and electrochemical permeation. The measured hydrogen concentration, C_H , by hot extraction tests after charging in the GBST solution at constant current density of -5 mA cm^{-2} was 0.67 wppm. C_H in the Na₂SO₄ and NaCl solutions, both charged at a constant potential of $-1050 \text{ mV}_{\text{Ag}/\text{AgCl}}$, were 0.136 and 0.092 wppm, respectively. The higher hydrogen uptake in GBST was attributed to the effect of the hydrogen recombination poison and the higher viscosity of the electrolyte. The charging current density also significantly affected C_H . During charging in the 3.5 wt.% NaCl solution, C_H was proportional to the square root of the charging current density.

In permeation, the first transient was less affected by strong trapping during charging in GBST than in the other two charging conditions. This was attributed to traps filling at a faster rate when the charging condition is severe and C_H is higher. D_{eff} of the Vintage steel depended on the charging condition. The effect of reversible trapping on D_{eff} was also reduced when using the most severe electrolyte. For the Vintage steel D_{eff} determined by the t_{lag} method was $1.26 \times 10^{-6} \text{ cm}^2 \text{ s}^{-1}$, which is comparable to the value determined by partial transients $1.6 \times 10^{-6} \text{ cm}^2 \text{ s}^{-1}$. Using the t_{lag} and t_b methods, the diffusivity rank from highest to lowest was the Modern QT steel, the Modern TMCP, and the Vintage steel. Due to the effect of trapping on D_{eff} and C_{0R} , it was challenging to rank the materials based on C_{0R} .

The Choo-Lee method was used to determine the E_b values for the three steels. As observed in Paper 3, the QT steel exhibited a normalized desorption curve, while the

desorption curve of the Vintage steel was broader and asymmetric. The desorption curve of the TMCP steel had a similar shape to that of the Vintage steel. E_b of the QT steel was 21 kJ/mol. The Vintage and TMCP steels' desorption curves were deconvoluted into two peaks. E_b were 11.7 and 40.4 kJ mol⁻¹ for the TMCP steel and 12.6 and 14.0 kJ mol⁻¹ for the Vintage steel. Overlapping of the peaks likely caused an underestimation of the E_b of the high-temperature peak in the Vintage steel.

A Pd coating affected the hydrogen uptake in samples exposed to H₂ gas at room temperature. The effect was most significant at 100 bar charging pressure, where the hydrogen uptake was 3.9-4.9 times higher in the Pd-coated samples. At 1000 bar charging pressure, the hydrogen concentration in the Pd-coated samples was 1.06-1.1 times higher than those of the non-coated samples. The lower significance of Pd at elevated pressure was attributed to the oxide layer being reduced at the higher pressure.

Chapter 5

Conclusion and further work

5.1 Conclusion

In this PhD project, hydrogen uptake, diffusion, and trapping in vintage and modern X65 pipeline steels have been investigated using hydrogen permeation and desorption techniques. Emphasis was put on relating electrochemical and gaseous hydrogen charging in terms of hydrogen uptake. Different techniques and charging conditions to determine hydrogen concentration, diffusivity, and trapping parameters were evaluated. The main findings can be summarized as follows:

- The sub-surface hydrogen concentration in lattice and reversible trap sites, C_{0R} , was proportional to the square root of the hydrogen charging fugacity, in agreement with Sieverts' law. At room temperature, the Sieverts' constants of the Vintage and the Modern QT steel were 0.0125 and 0.0095 wppm bar^{-1/2}, respectively. The Sieverts' relationships formed the basis of determining the equivalent hydrogen fugacity, $f_{H_2}^{eq}$, and pressure, $p_{H_2}^{eq}$, of electrochemical charging conditions.
- $f_{H_2}^{eq}$ and $p_{H_2}^{eq}$ were determined for different electrochemical charging conditions based on the assumption that two charging conditions are equivalent if they produce the same C_{0R} . A relationship between the $f_{H_2}^{eq}$ and the overpotential in 3.5 wt% NaCl was determined for the Vintage steel. $f_{H_2}^{eq}$ of electrochemical charging in 3.5 wt% NaCl solution at -1, -15, and -50 mA cm⁻² were 49.1, 101.9 and 222.7 bar, respectively.
- A systematic approach was used to determine an electrochemical charging condition equivalent to a H₂ gas pressure relevant for hydrogen transport in pipelines (200 bar). Cathodic protection simulated condition, -1050 mV_{Ag/AgCl} in 3.5 wt% NaCl, was chosen as a starting point and yielded a $p_{H_2}^{eq}$ of 12.3 bar for the Modern QT steel. Addition of 2 g l⁻¹ thiourea, a hydrogen recombination poison, increased $p_{H_2}^{eq}$ to 111.5 bar. $p_{H_2}^{eq}$ was further increased by changing the applied potential in the cathodic direction. A $p_{H_2}^{eq}$ of 201.9 bar was obtained at an applied potential of -1225 mV_{Ag/AgCl} in 3.5 wt% NaCl with addition of 2 g l⁻¹ thiourea.

- The lowest and highest measured effective diffusion coefficient, D_{eff} , of the Modern QT steel at room temperature were 8.56×10^{-7} and 2.70×10^{-6} $\text{cm}^2 \text{s}^{-1}$, about a three-time difference. For the Vintage steel, there was about a 17 times difference between the lowest and highest D_{eff} , which were 1.95×10^{-7} and 3.34×10^{-6} $\text{cm}^2 \text{s}^{-1}$, respectively. The larger scatter observed for the Vintage steel was attributed to a tortuous diffusion path and concentration-dependent effective diffusivity. A tortuous diffusion path would be most prominent in permeation tests for the Vintage steel because one-dimensional diffusion is assumed in the direction perpendicular to the ferrite-pearlite bands. The concentration dependency could be caused by differences in trap occupancy and dominating trap sites under different charging conditions.
- From diffusivity tests using permeation and desorption techniques, it was observed that strong hydrogen trapping was more prominent in the Vintage steel than in the Modern steel. In permeation tests, strong traps can be accounted for by performing subsequent transients, while in desorption methods, a modification to the solution of Fick's 2nd law was made to obtain a good fit to the desorption data. Partial permeation transients gave better representations of Fick's 2nd law than complete transients, mainly attributed to a smaller change in trap occupancy. The trap occupancy can change with the charging condition, leading to a concentration dependency of the D_{eff} . Using severe charging conditions can reduce the effect of traps on the transients attributed to traps being filled at a higher rate.
- The trap binding energy, E_b , was estimated from the diffusivity results. Using desorption and partial permeation methods, E_b were 28.2 and 28.9 kJ mol^{-1} in the Modern QT steel, and 26.0 and 20.4 kJ mol^{-1} in the Vintage steel. E_b was also determined using thermal desorption analysis and the Choo-Lee method. A normalized peak was observed in the Modern QT steel, having an E_b value of 21 kJ mol^{-1} . A broad asymmetric curve was observed in the Vintage and Modern TMCP steels, which was deconvoluted into two peaks. In the Modern TMCP steel, E_b were 11.7 and 40.4 kJ mol^{-1} . In the Vintage steel, E_b were 12.6 and 14.0 kJ mol^{-1} . An influence of multiple trap sites complicated the determination of E_b , e.g., overlapping peaks likely caused an underestimation of the E_b value of the second peak in the Vintage steel using the Choo-Lee method.

5.2 Further work

- Gas permeation used to determine Sieverts' constant was performed with a Pd-coating on the charging side of the sample. The Pd-coating was used to overcome any surface impedance that a naturally formed oxide layer could cause. It was discussed that the uptake on the Pd-coated surface could represent the uptake on the bare steel surface after the breakage of an oxide layer, e.g., from cyclic stresses due to pressure fluctuations. The catalytic effects of Pd, oxide, and bare steel surface should be evaluated. In addition, in-service surface conditions should be investigated, such as the effect of an internal flow coating.
- This work investigated the equivalency between electrochemical and gaseous

hydrogen charging in terms of hydrogen uptake. An overall aim is that electrochemical charging can aid in evaluating hydrogen-assisted material degradation of materials for hydrogen gas application. The transferability of the equivalency to mechanical testing for hydrogen embrittlement (HE) susceptibility must be verified, e.g., by fracture toughness and fatigue testing.

- There is a large scatter in reported values for $f_{\text{H}_2}^{\text{eq}}$ and $p_{\text{H}_2}^{\text{eq}}$ in the literature, which could be caused by a dependency on techniques utilized and materials investigated. It would be of interest to investigate what the main parameters are. To realize that, the equivalency should be examined by several methods, such as permeation, desorption, and hollow sensor methods on the same steel.
- Pipeline steels can be more susceptible to HE in the heat-affected zone (HAZ), where the microstructure can contain martensite. Hence, it would be valuable to test the hydrogen interaction with a HAZ microstructure and investigate to what degree $p_{\text{H}_2}^{\text{eq}}$ is affected.
- Gas impurities may be present in the H_2 gas stream during in-service conditions. It has been reported in the literature that gas impurities, such as O_2 and CO , can suppress the HE effect on steels. Further investigation of the effect of gas impurities on hydrogen uptake and the influence on equivalent charging conditions would be of interest.

Bibliography

- [1] European Commission. A hydrogen strategy for a climate-neutral Europe, 2020. URL https://knowledge4policy.ec.europa.eu/publication/communication-com2020301-hydrogen-strategy-climate-neutral-europe_en.
- [2] C. Yang and J. Ogden. Determining the lowest-cost hydrogen delivery mode. *International Journal of Hydrogen Energy*, 32(2):268–286, 2007.
- [3] S. Cerniauskas, A. Jose Chavez Junco, T. Grube, M. Robinius, and D. Stolten. Options of natural gas pipeline reassignment for hydrogen: Cost assessment for a Germany case study. *International Journal of Hydrogen Energy*, 45(21):12095–12107, 2020.
- [4] A. Laureys, R. Depraetere, M. Cauwels, T. Depover, S. Hertelé, and K. Verbeken. Use of existing steel pipeline infrastructure for gaseous hydrogen storage and transport: A review of factors affecting hydrogen induced degradation. *Journal of Natural Gas Science and Engineering*, 101, 2022.
- [5] S. Lipiäinen, K. Lipiäinen, A. Ahola, and E. Vakkilainen. Use of existing gas infrastructure in European hydrogen economy. *International Journal of Hydrogen Energy*, 48(80):31317–31329, 2023.
- [6] C. Tsiklios, M. Hermesmann, and T.E. Müller. Hydrogen transport in large-scale transmission pipeline networks: Thermodynamic and environmental assessment of repurposed and new pipeline configurations. *Applied Energy*, 327:120097, 2022.
- [7] Norwegian Petroleum. The oil and gas pipeline system, May 2023. URL <https://www.norskipetroleum.no/produksjon-og-eksport/rortransportsystemet/>.
- [8] S. Lynch. Hydrogen embrittlement phenomena and mechanisms. *Corrosion reviews*, 30(3):105–123, 2012.
- [9] L. Briottet, I. Moro, and P. Lemoine. Quantifying the hydrogen embrittlement of pipeline steels for safety considerations. *International Journal of Hydrogen Energy*, 37(22):17616–17623, 2012.
- [10] T. An, H. Peng, P. Bai, S. Zheng, X. Wen, and L. Zhang. Influence of hydrogen pressure on fatigue properties of X80 pipeline steel. *International Journal of Hydrogen Energy*, 42(23):15669–15678, 2017.

- [11] E. S. Drexler, A. J. Slifka, R. L. Amaro, N. Barbosa, D. S. Lauria, L. E. Hayden, and D. G. Stalheim. Fatigue crack growth rates of API X70 pipeline steel in a pressurized hydrogen gas environment. *Fatigue & Fracture of Engineering Materials & Structures*, 37(5):517–525, 2014.
- [12] M. L. Martin, M. Connolly, Z. N. Buck, P. E. Bradley, D. Lauria, and A. J. Slifka. Evaluating a natural gas pipeline steel for blended hydrogen service. *Journal of Natural Gas Science and Engineering*, 101:104529, 2022.
- [13] A. Turnbull. 4 - Hydrogen diffusion and trapping in metals. In R. P. Gangloff and B. P. Somerday, editors, *Gaseous Hydrogen Embrittlement of Materials in Energy Technologies*, volume 1 of *Woodhead Publishing Series in Metals and Surface Engineering*, pages 89 – 128. 2012.
- [14] N.E Nanninga, Y.S Levy, E.S Drexler, R.T. Condon, A.E Stevenson, and A.J Slifka. Comparison of hydrogen embrittlement in three pipeline steels in high pressure gaseous hydrogen environments. *Corrosion science*, 59:1–9, 2012.
- [15] P. Zhang, M. Laleh, A. E. Hughes, R. K.W. Marceau, T. Hilditch, and M. Y. Tan. A systematic study on the influence of electrochemical charging conditions on the hydrogen embrittlement behaviour of a pipeline steel. *International Journal of Hydrogen Energy*, 48(43):16501–16516, 2023.
- [16] A. Atrens, D. Mezzanotte, N.F Fiore, and M.A Genshaw. Electrochemical studies of hydrogen diffusion and permeability in Ni. *Corrosion science*, 20(5):673–684, 1980.
- [17] E. Koren. Hydrogen uptake and concentration in steel exposed to H₂ gas, Report 90481700-01, 2021. NTNU/MTP Report.
- [18] G. Krauss. *Steels: Processing, Structure, and Performance*. ASM International, Materials Park, 2 edition, 2015.
- [19] S. Vervynckt, K. Verbeken, B. Lopez, and J. J. Jonas. Modern HSLA steels and role of non-recrystallisation temperature. *International Materials Reviews*, 57(4):187–207, 2012.
- [20] R. H. Petrov, J. J. Jonas, L. A. I. Kestens, and J. M. Gray. Microstructure and texture development in pipeline steels. In R. W. Revie, editor, *Oil and gas pipelines: Integrity and safety handbook*, pages 157–186. John Wiley & Sons, 2015.
- [21] American Petroleum Institute. API Specification 5L, Specifications for Line Pipe, 2012.
- [22] B. Guo, S. Song, A. Ghalambor, and T. R. Lin. *Offshore pipelines: Design, installation and Maintenance*. Gulf Professional Publishing, 2 edition, 2014.
- [23] W. H. Johnson. On Some Remarkable Changes Produced in Iron and Steel by the Action of Hydrogen and Acids. *Proceedings of the Royal Society of London*, 23(156-163):168–179, 1874.
- [24] A. Barnoush and H. Vehoff. Recent developments in the study of hydrogen

- embrittlement: Hydrogen effect on dislocation nucleation. *Acta Materialia*, 58 (16):5274–5285, 2010.
- [25] I. M. Robertson, P. Sofronis, A. Nagao, M. L. Martin, S. Wang, D. W. Gross, and K. E. Nygren. Hydrogen Embrittlement Understood. *Metallurgical and Materials Transactions A*, 46:2323–2341, 2015.
- [26] T. An, S. Zheng, H. Peng, X. Wen, L. Chen, and L. Zhang. Synergistic action of hydrogen and stress concentration on the fatigue properties of X80 pipeline steel. *Materials Science and Engineering: A*, 700:321–330, 2017.
- [27] J. A. Ronevich, B. P. Somerday, and C. W. San Marchi. Effects of microstructure banding on hydrogen assisted fatigue crack growth in X65 pipeline steels. *International Journal of Fatigue*, 82(P3):497–504, 2016.
- [28] A. J. Slifka, E. S. Drexler, N. E. Nanninga, Y. S. Levy, J. D. McColskey, R. L. Amaro, and A. E. Stevenson. Fatigue crack growth of two pipeline steels in a pressurized hydrogen environment. *Corrosion Science*, 78:313–321, 2014.
- [29] X. Wu, H. Zhang, M. Yang, W. Jia, Y. Qiu, and L. Lan. From the perspective of new technology of blending hydrogen into natural gas pipelines transmission: Mechanism, experimental study, and suggestions for further work of hydrogen embrittlement in high-strength pipeline steels. *International Journal of Hydrogen Energy*, 47(12):8071–8090, 2022.
- [30] I. Moro, L. Briottet, P. Lemione, E. Andrieu, C. Blanc, G. Odemer, J. Chene, and F. Jambon. Damage under high pressure hydrogen environment of a high strength pipeline steel X80. In B. Somerday, P. Sofronis, and R. Jones, editors, *Proceedings of the 2008 International Hydrogen Conference*, pages 357–364. ASM International, 2008.
- [31] P. Marcus and E. Protopopoff. *Corrosion Mechanisms in Theory and Practice*. Corrosion technology. CRC Press, 3rd edition, 2012.
- [32] R. Kirchheim and A. Pundt. Hydrogen in Metals. In D. E. Laughlin and K. Hono, editors, *Physical Metallurgy*, pages 2597–2705. Elsevier, 5th edition, 2015.
- [33] C. K. Gupta. *Chemical metallurgy : principles and practice*. Wiley-VCH, Weinheim, 2003.
- [34] C. San Marchi and B. P. Somerday. Effects of High-Pressure Gaseous Hydrogen on Structural Metals. *SAE Transactions*, 116:94–109, 2007.
- [35] M. Nagumo. *Fundamentals of Hydrogen Embrittlement*. Springer, Singapore, 2016.
- [36] K. Kiuchi and R.B. McLellan. The solubility and diffusivity of hydrogen in well-annealed and deformed iron. *Acta Metallurgica*, 31(7):961–984, 1983.
- [37] Q. Liu, A. D. Atrens, Z. Shi, K. Verbeken, and A. Atrens. Determination of the hydrogen fugacity during electrolytic charging of steel. *Corrosion Science*, 87: 239–258, 2014.

- [38] A. Staykov, J. Yamabe, and B. P. Somerday. Effect of hydrogen gas impurities on the hydrogen dissociation on iron surface. *International Journal of Quantum Chemistry*, 114(10):626–635, 2014.
- [39] A. Staykov, R. Komoda, M. Kubota, P. Ginet, F. Barbier, and J. Furtado. Coadsorption of CO and H₂ on an Iron Surface and Its Implication on the Hydrogen Embrittlement of Iron. *The Journal of Physical Chemistry C*, 123(50):30265–30273, 2019.
- [40] R. Komoda, M. Kubota, S. Yoshida, A. Staykov, P. Ginet, F. Barbier, and J. Furtado. Inhibition of Hydrogen Embrittlement of Cr-Mo Steel by the Addition of Impurities to Hydrogen Environment and the Effect of Material Strength. Sapporo, Japan, 2018. ISOPE.
- [41] R. Komoda, K. Yamada, M. Kubota, P. Ginet, F. Barbier, J. Furtado, and L. Prost. The inhibitory effect of carbon monoxide contained in hydrogen gas environment on hydrogen-accelerated fatigue crack growth and its loading frequency dependency. *International Journal of Hydrogen Energy*, 44(54):29007–29016, 2019.
- [42] R. Komoda, M. Kubota, A. Staykov, P. Ginet, F. Barbier, and J. Furtado. Inhibitor effect of oxygen on hydrogen-induced fracture of A333 pipe steel. *Fatigue & Fracture of Engineering Materials & Structures*, 42(6):1387–1401, 2019.
- [43] B. P. Somerday, P. Sofronis, K. A. Nibur, C. San Marchi, and R. Kirchheim. Elucidating the variables affecting accelerated fatigue crack growth of steels in hydrogen gas with low oxygen concentrations. *Acta materialia*, 61(16):6153–6170, 2013.
- [44] R. Song, S. Pyun, and R.A. Oriani. The hydrogen permeation through passivating film on iron by modulation method. *Electrochimica Acta*, 36(5):825–831, 1991.
- [45] P. Bruzzoni and R. Garavaglia. Anodic iron oxide films and their effect on the hydrogen permeation through steel. *Corrosion Science*, 33(11):1797–1807, 1992.
- [46] A. Nagao, N. Ishikawa, S. Takagi, and M. Kimura. Hydrogen uptake in steels exposed to high pressure H₂ gas. In *Materials Performance in Hydrogen Environment*, Wyoming, USA, 2017. ASME.
- [47] T. Zhang, W. Zhao, Y. Zhao, K. Ouyang, Q. Deng, Y. Wang, and W. Jiang. Effects of surface oxide films on hydrogen permeation and susceptibility to embrittlement of X80 steel under hydrogen atmosphere. *International Journal of Hydrogen Energy*, 43(6):3353 – 3365, 2018.
- [48] J. Venezuela, E. Gray, Q. Liu, Q. Zhou, C. Tapia-Bastidas, M. Zhang, and A. Atrens. Equivalent hydrogen fugacity during electrochemical charging of some martensitic advanced high-strength steels. *Corrosion Science*, 127:45–58, 2017.
- [49] J. Venezuela, C. Tapia-Bastidas, Q. Zhou, T. Depover, K. Verbeken, E. Gray,

- Q. Liu, Q. Liu, M. Zhang, and A. Atrens. Determination of the equivalent hydrogen fugacity during electrochemical charging of 3.5NiCrMoV steel. *Corrosion Science*, 132:90–106, 2018.
- [50] Q. Liu, E. Gray, J. Venezuela, Q. Zhou, C. Tapia-Bastidas, M. Zhang, and A. Atrens. Equivalent Hydrogen Fugacity during Electrochemical Charging of 980DP Steel Determined by Thermal Desorption Spectroscopy. *Advanced Engineering Materials*, 20(1), 2018.
- [51] A. J. Kumnick and H. H. Johnson. Steady state hydrogen transport through zone refined irons. *Metallurgical Transactions A*, 6:1087–1091, 1975.
- [52] P. Castaño Rivera, V.P. Ramunni, and P. Bruzzoni. Hydrogen trapping in an API 5L X60 steel. *Corrosion Science*, 54:106–118, 2012.
- [53] J. Yamabe, T. Awane, and S. Matsuoka. Investigation of hydrogen transport behavior of various low-alloy steels with high-pressure hydrogen gas. *International Journal of Hydrogen Energy*, 40(34):11075–11086, 2015.
- [54] L. Zhang, W. Cao, K. Lu, Z. Wang, Y. Xing, Y. Du, and M. Lu. Effect of the cathodic current density on the sub-surface concentration of hydrogen in X80 pipeline steels under cathodic protection. *International Journal of Hydrogen Energy*, 42(5):3389–3398, 2017.
- [55] A. Turnbull and L. Wright. Hydrogen permeation modelling with generalised boundary conditions at the charging surface. *NPL Report Mat 69*, 2014.
- [56] J. O’M. Bockris, J. McBreen, and L. Nanis. The Hydrogen Evolution Kinetics and Hydrogen Entry into α -Iron. *Journal of The Electrochemical Society*, 112(10):1025, 1965.
- [57] X. Lu, D. Wang, and R. Johnsen. Hydrogen diffusion and trapping in nickel-based alloy 625: An electrochemical permeation study. *Electrochimica Acta*, 421:140477, 2022.
- [58] B. J. Berkowitz, J. J. Burton, C. R. Helms, and R. S. Polizzotti. Hydrogen dissociation poisons and hydrogen embrittlement. *Scripta Metallurgica*, 10(10): 871–873, 1976.
- [59] K. Murakami, N. Yabe, H. Suzuki, K. Takai, Y. Hagihara, and Y. Wada. Substitution of High-Pressure Charge by Electrolysis Charge and Hydrogen Environment Embrittlement Susceptibilities for Inconel 625 and SUS 316L. pages 563–570, Vancouver, Canada, 2006. ASME.
- [60] J. O’M. Bockris and P.K. Subramanian. The equivalent pressure of molecular hydrogen in cavities within metals in terms of the overpotential developed during the evolution of hydrogen. *Electrochimica Acta*, 16(12):2169–2179, 1971.
- [61] R. A. Oriani and P. H. Josephic. Hydrogen-enhanced load relaxation in a deformed medium-carbon steel. *Acta Metallurgica*, 27(6):997–1005, 1978.
- [62] A. Yaktiti, A. Dreano, J.F. Carton, and F. Christien. Hydrogen diffusion and trapping in a steel containing porosities. *Corrosion Science*, 199:110208, 2022.

- [63] J. L. Crolet and G. Maisonneuve. Construction of a universal scale of severity for hydrogen cracking. In *CORROSION*, pages NACE-00127, 2000.
- [64] W. D. Callister and D. G. Retwisch. *Material Science and Engineering*. Wiley, 9th edition, 2014.
- [65] G. M. Pressouyre and I. M. Bernstein. A quantitative analysis of hydrogen trapping. *Metallurgical Transactions A*, 9(11):1571–1580, 1978.
- [66] R.A Oriani. The diffusion and trapping of hydrogen in steel. *Acta metallurgica*, 18(1):147–157, 1970.
- [67] L. Cheng, L. Li, X. Zhang, J. Liu, and K. Wu. Numerical simulation of hydrogen permeation in steels. *Electrochimica Acta*, 270:77–86, 2018.
- [68] A. J. Griffiths and A. Turnbull. On the effective diffusivity of hydrogen in low alloy steels. *Corrosion Science*, 37(11):1879–1881, 1995.
- [69] F. G. Wei and K. Tsuzaki. Quantitative analysis on hydrogen trapping of TiC particles in steel. *Metallurgical and Materials Transactions A*, 37(2):331–353, 2006.
- [70] W Y Choo and J. Y. Lee. Hydrogen trapping phenomena in carbon steel. *Journal of Materials Science*, 17:1930–1938, 1982.
- [71] W. Y. Choo and J. Y. Lee. Effect of cold working on the hydrogen trapping phenomena in pure iron. *Metallurgical Transactions A*, 14(7):1299–1305, July 1983.
- [72] W. Y. Choo and J. Y. Lee. Thermal analysis of trapped hydrogen in pure iron. *Metallurgical and Materials Transactions A*, 13:135–140, 1982.
- [73] M. Koyama, M. Rohwerder, C. C. Tasan, A. Bashir, E. Akiyama, K. Takai, D. Raabe, and K. Tsuzaki. Recent progress in microstructural hydrogen mapping in steels: quantification, kinetic analysis, and multi-scale characterisation. *Materials Science and Technology*, 33(13):1481–1496, 2017.
- [74] E. Fallahmohammadi, F. Bolzoni, and L. Lazzari. Measurement of lattice and apparent diffusion coefficient of hydrogen in X65 and F22 pipeline steels. *International Journal of Hydrogen Energy*, 38(5):2531–2543, 2013.
- [75] G. T. Park, S. U. Koh, H. G. Jung, and K. Y. Kim. Effect of microstructure on the hydrogen trapping efficiency and hydrogen induced cracking of linepipe steel. *Corrosion Science*, 50(7):1865–1871, 2008.
- [76] Y.F. Cheng. Analysis of electrochemical hydrogen permeation through X-65 pipeline steel and its implications on pipeline stress corrosion cracking. *International Journal of Hydrogen Energy*, 32(9):1269–1276, 2007.
- [77] T. A. Jack, R. Pourazizi, E. Ohaeri, J. Szpunar, J. Zhang, and J. Qu. Investigation of the hydrogen induced cracking behaviour of API 5L X65 pipeline steel. *International Journal of Hydrogen Energy*, 45(35):17671–17684, 2020.

-
- [78] E. Fallahmohammadi, F. Bolzoni, G. Fumagalli, G. Re, G. Benassi, and L. Lazzari. Hydrogen diffusion into three metallurgical microstructures of a C–Mn X65 and low alloy F22 sour service steel pipelines. *International Journal of Hydrogen Energy*, 39(25):13300–13313, 2014.
- [79] F. Bolzoni and E. Fallahmohammadi. Electrochemical Investigation of Hydrogen Diffusion in Pipeline Steels. In *NACE CORROSION*, pages NACE–2013–2792, 2013.
- [80] H. Lee and S. Lap-Ip Chan. Hydrogen embrittlement of AISI 4130 steel with an alternate ferrite/pearlite banded structure. *Materials Science & Engineering A*, 142(2):193–201, 1991.
- [81] L. Tau and S.L.I. Chan. Effects of ferrite/pearlite alignment on the hydrogen permeation in a AISI 4130 steel. *Materials Letters*, 29(1-3):143–147, 1996.
- [82] A. Alvaro, A.B. Hagen, M. Lervåg, B. Nyhus, and V. Olden. Materials testing and characterization of four X60-X65 pipeline steels. Technical Report 2020:01325, SINTEF Industry, 2021.
- [83] A. Alvaro, A. O. Myhre, B. Nyhus, A. Vinogradov, and V. Olden. HyLINE status meeting-WP3, Mechanical performances of pipelines for H2 gas transport, 2022.
- [84] E. Koren, C. M. H. Hagen, J. Yamabe, A.B. Hagen, D. Wang, and R. Johnsen. HyLINE status meeting-WP1, Hydrogen uptake and diffusion, 2022.
- [85] D. Wang, A. B. Hagen, D. Wan, X. Lu, and R. Johnsen. Probing hydrogen effect on nanomechanical properties of X65 pipeline steel using in-situ electrochemical nanoindentation. *Materials Science and Engineering: A*, 824:141819, 2021.
- [86] D. Wang, A.B. Hagen, P.U. Fathi, M. Lin, R. Johnsen, and X. Lu. Investigation of hydrogen embrittlement behavior in X65 pipeline steel under different hydrogen charging conditions. *Materials Science and Engineering: A*, 860: 144262, 2022.
- [87] A. O. Myhre, A. B. Hagen, B. Nyhus, V. Olden, A. Alvaro, and A. Vinogradov. Hydrogen Embrittlement Assessment of Pipeline Materials Through Slow Strain Rate Tensile Testing. *Procedia Structural Integrity*, 42:935–942, 2022.
- [88] M. A. V. Devanathan and Z. Stachurski. The Adsorption and Diffusion of Electrolytic Hydrogen in Palladium. *Proceedings of the Royal Society of London. Series A. Mathematical and Physical Sciences*, 270(1340):90–102, 1962.
- [89] ISO 17081 Method of measurement of hydrogen permeation and determination of hydrogen uptake and transport in metals by an electrochemical technique, 2014.
- [90] Practice for Evaluation of Hydrogen Uptake, Permeation, and Transport in Metals by an Electrochemical Technique. Technical report, ASTM International, 2018.
- [91] E. Akiyama and S. Li. Electrochemical hydrogen permeation tests under
-

- galvanostatic hydrogen charging conditions conventionally used for hydrogen embrittlement study. *Corrosion Reviews*, 34(1-2), 2016.
- [92] P. Manolatos, M. Jerome, and J. Galland. Necessity of a palladium coating to ensure hydrogen oxidation during electrochemical permeation measurements on iron. *Electrochimica Acta*, 40(7):867–871, 1995.
- [93] H. Husby, M. Iannuzzi, R. Johnsen, M. Kappes, and A. Barnoush. Effect of nickel on hydrogen permeation in ferritic/pearlitic low alloy steels. *International Journal of Hydrogen Energy*, 43(7):3845–3861, 2018.
- [94] S. Frappart, X. Feaugas, J. Creus, F. Thebault, L. Delattre, and H. Marchebois. Study of the hydrogen diffusion and segregation into Fe–C–Mo martensitic HSLA steel using electrochemical permeation test. *Journal of Physics and Chemistry of Solids*, 71(10):1467–1479, 2010.
- [95] T. Zakroczymski. Adaptation of the electrochemical permeation technique for studying entry, transport and trapping of hydrogen in metals. *Electrochimica Acta*, 51(11):2261–2266, 2006.
- [96] T. Matsuo, J. Yamabe, H. Furukawa, K. Seki, K. Shimizu, S. Watanabe, and S. Matsuoka. Development of New Strain Gage for High-Pressure Hydrogen Gas Use. *Experimental Mechanics*, 54(3):431–442, 2014.
- [97] A. Demarez, A. G. Hocks, and F. A. Meuniers. Diffusion of hydrogen in mild steel. *Acta Metallurgica*, 2(2):214–223, 1954.
- [98] H. E. Kissinger. Reaction Kinetics in Differential Thermal Analysis. *Analytical chemistry.*, 29(11):1702–1706, 1957. Place: Washington, DC : Publisher: American Chemical Society,.
- [99] J. Yamabe, O. Takakuwa, H. Matsunaga, H. Itoga, and S. Matsuoka. Hydrogen diffusivity and tensile-ductility loss of solution-treated austenitic stainless steels with external and internal hydrogen. *International Journal of Hydrogen Energy*, 42(18):13289 – 13299, 2017.
- [100] R. Kirchheim. Bulk Diffusion-Controlled Thermal Desorption Spectroscopy with Examples for Hydrogen in Iron. *Metallurgical and Materials Transactions A*, 47(2):672–696, 2016.

Appended papers

Paper 1

Experimental comparison of gaseous and electrochemical hydrogen charging in X65 pipeline steel using the permeation technique

E. Koren, C. M. H. Hagen, D. Wang, X. Lu, R. Johnsen, J. Yamabe

Corrosion Science 215 (2023) 111025

DOI: 10.1016/j.corsci.2023.111025



Experimental comparison of gaseous and electrochemical hydrogen charging in X65 pipeline steel using the permeation technique

Erik Koren^{a,*}, Catalina M. H. Hagen^b, Dong Wang^a, Xu Lu^a, Roy Johnsen^a, Junichiro Yamabe^c

^a Department of Mechanical and Industrial Engineering, NTNU, 7491 Trondheim, Norway

^b SINTEF, Richard Birkelandsvei 2B, 7465 Trondheim, Norway

^c Department of Mechanical Engineering, Fukuoka University, 8-19-1 Nanakuma, Jonan-ku, Fukuoka 814-0180, Japan

ARTICLE INFO

Keywords:

- A. Low alloy steel
- B. Hydrogen permeation
- B. Galvanostatic
- C. Hydrogen embrittlement
- C. Hydrogen absorption

ABSTRACT

Herein, hydrogen uptake and diffusivity in X65 pipeline steel were investigated using the permeation technique under different hydrogen charging conditions. Hydrogen charging was performed using hydrogen gas at different pressures, and electrochemical charging was performed at different cathodic current densities. The results revealed that both the sub-surface hydrogen concentration in lattice and reversible trap sites and the effective hydrogen diffusivity were dependent on the charging conditions. Moreover, the relationship between equivalent hydrogen fugacity and overpotential was determined.

1. Introduction

The world is going through a transition from using fossil fuels towards using more renewable energy sources, aiming to reduce the emission of greenhouse gases. Hydrogen, as a clean energy carrier, is regarded as a key building block in realising a climate-neutral and zero-pollution economy [1]. For long-distance transportation of hydrogen gas, pipelines are an economically favoured choice [2,3]. A reassignment of the existing infrastructure of steel pipelines utilised for transportation of natural gas, to transport hydrogen gas, could reduce hydrogen delivery costs by 60% [4] and ease the realisation of a hydrogen economy.

However, thorough material investigations are required for safe transportation of hydrogen gas via steel pipelines. Atomic hydrogen can absorb and diffuse into steel and potentially degrade its mechanical properties; this phenomenon is referred to as hydrogen embrittlement (HE) [5–8]. Although, tensile and fatigue investigations in gaseous hydrogen environment have shown a decrease in ductility and increased fatigue crack growth rate [6,9–16], the majority of hydrogen-related studies have been performed using electrochemical charging. One reason for this is that gaseous hydrogen charging facilities are limited and mandate strict safety protocols [17]. To compare investigations of HE susceptibility utilising electrochemical and gaseous charging, the charging methods should produce a comparable hydrogen concentration, as the concentration of hydrogen in steel can affect the degree of

HE [6,12,18]. Therefore, the establishment of a relationship between the severity of hydrogen gas charging and electrochemical charging is critical.

It has been proposed that two charging conditions are equivalent if they produce the same activity of hydrogen in a steel [19]. Fugacity can be regarded as the activity of a real gas; hence, the hydrogen fugacity, f_{H_2} , relates to the ease of hydrogen uptake at the surface of a specific metal [19–21]. Studies correlating electrochemical charging and hydrogen gas charging have determined the equivalent hydrogen fugacity, $f_{H_2}^{eq}$, during electrochemical charging. $f_{H_2}^{eq}$ is typically expressed as a function of the overpotential, η . The hydrogen permeation technique [18,19] and thermal desorption spectroscopy (TDS) [21–23] are the two methods employed to determine $f_{H_2}^{eq}$. In a permeation cell, hydrogen enters the sample membrane on one side (charging side), diffuses through the sample membrane, and is oxidized on the exit side (detection side) [24]. The oxidation current density or permeation current density, i_p , is a measure of the hydrogen flux passing through the sample. Fick's laws of diffusion can be used to determine the hydrogen uptake and diffusivity. Permeation tests have been used to determine $f_{H_2}^{eq}$ by comparing the permeability coefficient obtained with gas charging with that obtained using electrochemical charging [25], or to determine $f_{H_2}^{eq}$ as a function of η using electrochemical permeation in combination with thermodynamic calculations [18,19]. TDS allows the determination of the hydrogen uptake and diffusivity by measuring the amount of desorbed hydrogen gas from a precharged sample [26,27]. The

* Corresponding author.

E-mail address: erik.a.koren@ntnu.no (E. Koren).

relationship between $f_{H_2}^{eq}$ and η is determined using TDS by comparing the hydrogen concentration in gas-charged and electrochemically charged samples [21–23].

However, several experimental difficulties must be overcome during charging to determine the correct value of $f_{H_2}^{eq}$. One such challenge is to maintain stable surface conditions during charging, which is an essential requirement for determining the uptake and diffusivity through the permeation technique. During electrochemical charging presence and modifications of an oxide layer, formation of corrosion products or excessive evolution of hydrogen bubbles can affect i_p [28–30]. Moreover, it has been reported that severe hydrogen charging can induce damage, such as blisters and cracks [30–33]. In gas-phase charging, a Pd coating may be necessary to achieve equilibrium on the charging side because air-formed oxides impede hydrogen entry [25,27,34]. The sub-surface lattice hydrogen concentration, C_0 , has been regarded as a direct reflection of the severity of the charging condition and suggested to be an appropriate measure for comparing the uptake from different hydrogen sources [7]. However, trapping sites, which are microstructural features wherein hydrogen may reside, affect the uptake and diffusivity of hydrogen [35] rendering it difficult to determine C_0 [36]. At such trap sites, the activation energy of a hydrogen atom jumping to a neighbouring lattice site is greater than that between regular lattice sites, thus causing a reduction in the diffusivity. The term “reversible trap” typically refers to trap sites wherein hydrogen has a short residence time at the temperature of interest corresponding to a low de-trapping activation energy, whereas the term “irreversible trap” refers to trap sites where the probability of releasing trapped hydrogen is negligible under the same conditions [37]. When reversible trapping affects the transport of hydrogen in steels, the diffusion coefficient determined from permeation tests is an effective value, denoted as D_{eff} , and the sub-surface concentration includes hydrogen in lattice and reversible trap sites, denoted as C_{OR} [36]. However, if the fraction of occupied traps changes to an extent such that the permeation transient does not follow Fick’s 2nd law, D_{eff} has no theoretical basis [36,38,39]. In this case, D_{eff} can vary by one order of magnitude depending on the severity of charging conditions, and C_{OR} is typically overestimated [35, 40]. The change in trap occupancy can be minimized by performing successive transients with a partial increase or decrease in the charging current [41–43]. Previous reports have stated that during partial permeation transients, surface and trapping effects can be eliminated to an extent such that the lattice diffusion coefficient, D_L , can be determined [41,44].

The aim of this study was to correlate hydrogen gas charging and electrochemical charging for a X65 pipeline steel. The hydrogen uptake and diffusivity were evaluated via the permeation technique by employing both hydrogen gas charging and electrochemical charging. The dependency of D_{eff} on the charging conditions was investigated. C_{OR} was then employed to determine a relationship between $f_{H_2}^{eq}$ and η .

2. Experimental

2.1. Material and sample preparation

The material used in this study was API 5 L X65 steel from a hot-rolled and arc-welded vintage pipeline. The wall thickness was 26 mm. Its chemical composition is listed in Table 1. The samples were machined from a position close to the inner side of the pipe wall along

Table 1
Chemical composition of X65 pipeline steel.

Element	C	Si	Mn	P	S	Cu	Cr
wt%	0.1	< 0.6	< 1.6	< 0.025	< 0.015	< 0.25	< 0.25
Element	Ni	Mo	V	Nb	Ti	N	-
wt%	< 0.25	< 0.05	< 0.1	< 0.05	< 0.02	< 0.01	-

the longitudinal direction. The samples used for the electrochemical permeation tests were disks with diameters of 30 mm and thicknesses of 1.9 mm, whereas the samples used for the gas permeation tests were 50 mm wide, 150 mm long, and 1.9 mm thick plates. Both sides of the disks and plates were ground using SiC grinding papers to a final grade of #P1000. The detection side of both types of samples were electroplated with Pd to ensure complete oxidation of hydrogen, as hydrogen oxidation is known to occur more easily on a Pd surface [45]. In addition, the plates used for gas permeation were electroplated with Pd on the charging side to overcome the surface impedance which can be caused by an oxide layer [25,27,34]. The electroplating procedure followed the method described by Husby et al. [46] based on the work of Bruzzoni et al. [47,48] and Castaño Rivera et al. [11]. After electroplating, the samples were placed in a furnace at 120 °C for 16 h to remove the hydrogen introduced during the plating process.

2.2. Gas permeation

A high-pressure H₂ gas permeation apparatus was employed for the tests, certified for pressures of up to 100 bar. The apparatus is illustrated in Fig. 1. H₂ gas of a 6.0 quality, with a purity of 99.99999%, was injected into the cell on the charging side from 50 L-gas bottles until a pre-determined pressure was achieved. Three gas pressures, p_{H_2} , were employed for testing: 10, 50, and 100 bar. The valves were then closed, and the charging of the samples commenced. The exposed surface area of the sample in each chamber was 16 cm². The cell corresponding to the exit side consisted of 0.1 M NaOH (pH = 12.6) with continuous N₂ gas purge. A Pt foil was used as the counter electrode. The exit surface of the Pd coated steel, was polarised at + 360 mV vs. Ag/AgCl in saturated KCl (+315 mV vs. saturated calomel electrode (SCE)) while measuring i_p . All tests were performed using succeeding transients. Three charging/discharging cycles were performed at each gas pressure. Discharging was performed by evacuating the gas on the entry side. All gas permeation tests were performed at 21 ± 1 °C.

2.3. Electrochemical permeation

An illustration of the cell used for electrochemical permeation tests is presented in Fig. 2. The sample was mounted into the sample holder and held between the two chambers in the permeation cell using gaskets and clamps. The exposed surface area of the sample in each chamber was 3.7 cm². The detection chamber (oxidation side) was filled with a 0.1 M NaOH electrolyte (pH = 12.6) and purged with N₂ gas. An Hg/Hg₂SO₄ electrode in saturated K₂SO₄ was used as the reference electrode, and a Pt foil was used as the counter electrode. A potential of – 80 mV vs. Hg/Hg₂SO₄ (+318 mV vs. SCE) was applied. While i_p was stabilising, the charging chamber was constantly purged with N₂ gas to avoid oxidation. When i_p attained a stable value below 0.1 μA cm⁻², the N₂ gas supply to the charging chamber was cut off, and a solution of 3.5 wt% NaCl (pH = 6.6) was introduced into the charging chamber. In the charging chamber, an Ag/AgCl electrode in saturated KCl was used as the reference electrode, and a Pt foil was used as the counter electrode. Different cathodic charging current densities, i_c , were applied: – 1, – 15 and – 50 mA cm⁻². When i_p reached a steady state, denoted as i_p^{ss} , the test was terminated, and the permeation cell was dismantled. In contrast to the gas permeation test, the sample was removed from the sample holder and kept in a desiccator overnight to allow hydrogen degassing. The charging side was further ground using a #P1000 grinding paper to remove any corrosion products within 1 h before initiation of the next transient. The change in the sample thickness was negligible. Three transients were performed for each charging condition. All electrochemical permeation tests were performed at 21 ± 1 °C.

In addition, partial permeation transients were performed to reduce trapping and potential surface effects that are known to impede hydrogen uptake [41]. First, a complete build-up permeation transient

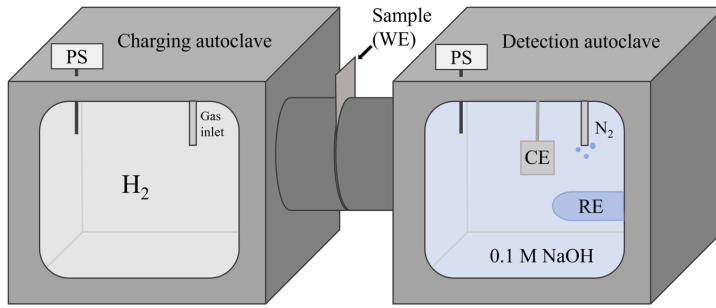


Fig. 1. Schematic of the high pressure H₂ gas permeation cell. WE – working electrode, CE – counter electrode, RE – reference electrode, PS – pressure sensor.

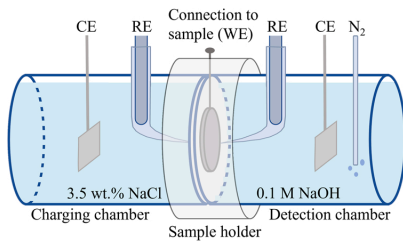


Fig. 2. Schematic of the electrochemical permeation cell. WE – working electrode, CE – counter electrode, RE – reference electrode.

was performed by applying an i_c of -1 mA cm^{-2} for 12 h, to produce a stable surface condition. i_c was then increased in steps of 1 mA cm^{-2} in the cathodic direction until i_c reached -7 mA cm^{-2} , while i_p was continuously measured on the detection side. A good fit between i_p and Fick's 2nd law was observed at -7 mA cm^{-2} . After stabilisation was achieved, i_c was decreased in steps of 1 mA cm^{-2} in the anodic direction until i_c reached -1 mA cm^{-2} .

2.4. Analysis

From the permeation transients, D_{eff} can be calculated using the breakthrough time method and time lag method, as presented in Eqs. (1) and (2), respectively [24,36,38,49]. L denotes the thickness of the sample. The breakthrough time, t_b , represents the intercept between the extrapolation of the linear portion of the build-up of i_p and the baseline of i_p . A difference in t_b between the first and subsequent transients indicates irreversible trapping [37]. Irreversible traps are not emptied between successive permeation transients; hence, they slow down the hydrogen transport during the first transient but do not affect the subsequent transients. The time lag, t_{lag} , represents the time required to attain 63% of i_p^∞ .

$$D_{\text{eff}}(t_b) = \frac{L^2}{19.8t_b} \quad (1)$$

$$D_{\text{eff}}(t_{\text{lag}}) = \frac{L^2}{6t_{\text{lag}}} \quad (2)$$

The diffusion coefficient of hydrogen, D , from partial permeation tests was estimated by fitting the experimental results to an analytical solution of Fick's 2nd law. The build-up of i_p can be fit to Eq. (3), and the decay of i_p can be fitted to Eq. (4) [41]. t denotes the time after changing i_c , and i_p^0 denotes the initial value of the permeation current density when i_c is changed.

$$\frac{i_p - i_p^0}{i_p^\infty - i_p^0} = \frac{2L}{\sqrt{\pi Dt}} \sum_{n=0}^{\infty} \exp\left(-\frac{(2n+1)^2 L^2}{4Dt}\right) \quad (3)$$

$$\frac{i_p - i_p^\infty}{i_p^0 - i_p^\infty} = 1 - \frac{2L}{\sqrt{\pi Dt}} \sum_{n=0}^{\infty} \exp\left(-\frac{(2n+1)^2 L^2}{4Dt}\right) \quad (4)$$

C_{OR} is proportional to i_p^∞ and can be calculated using Eq. (5). F denotes the Faraday constant ($96485 \text{ A s mol}^{-1}$) [36].

$$C_{\text{OR}} = \frac{i_p^\infty L}{FD_{\text{eff}}} \quad (5)$$

3. Results

3.1. Microstructure

Fig. 3(a) and (b) presents the scanning electron microscopy (SEM) micrographs of the studied steel. The microstructure primarily consists of polygonal ferrite, together with pearlite. The plate-like microstructure with a banded appearance indicates that some bainite is also present. The average grain size is $3.7 \mu\text{m}$.

3.2. Hydrogen diffusivity

3.2.1. Gas permeation

Three consecutive permeation transients performed at 100 bar of H₂ gas pressures are presented in Fig. 4(a). A significant difference in t_b between the first and subsequent transients can be observed, indicating that irreversible traps affect the first transient [37]. As the investigation of irreversible traps is not within the scope of this study, the results obtained from the first transient will not be reported herein. The second and third permeation transients obtained at different p_{H_2} are presented in Fig. 4(b). Transient 2 and 3 concur well at all p_{H_2} . An increase in p_{H_2} caused an increase in i_p^∞ and a reduction in t_b .

The normalised hydrogen flux, as a function of the normalised time for gas permeation transients, is presented in Fig. 5, along with the predictions of Fick's 2nd law calculated using the hydrogen diffusion coefficient in well-annealed bcc iron, $7.27 \times 10^{-5} \text{ cm}^2 \text{ s}^{-1}$ [50]. The normalised gas permeation transients are shifted to the right and are steeper than that predicted by Fick's 2nd law. A normalised permeation transient that is steeper than that predicted by Fick's 2nd law indicates a significant change in trap occupancy, which affects the transport of hydrogen [36,38,39]. Thus, the determinations of $D_{\text{eff}}(t_b)$ and $D_{\text{eff}}(t_{\text{lag}})$ using Eqs. (1) and (2) have no theoretical basis.

The average values for D_{eff} calculated by the t_b and t_{lag} methods from transients 2 and 3 are presented in Table 2. D_{eff} increases with increasing p_{H_2} . $D_{\text{eff}}(t_b)$ ranges from $2.21 \times 10^{-7} \text{ cm}^2 \text{ s}^{-1}$ at 10 bar to $3.23 \times 10^{-7} \text{ cm}^2 \text{ s}^{-1}$ at 100 bar, while $D_{\text{eff}}(t_{\text{lag}})$ ranges from $4.45 \times 10^{-7} \text{ cm}^2 \text{ s}^{-1}$ at 10 bar to $7.53 \times 10^{-7} \text{ cm}^2 \text{ s}^{-1}$ at 100 bar. $D_{\text{eff}}(t_{\text{lag}})$ is 1.9 – 2.3 times

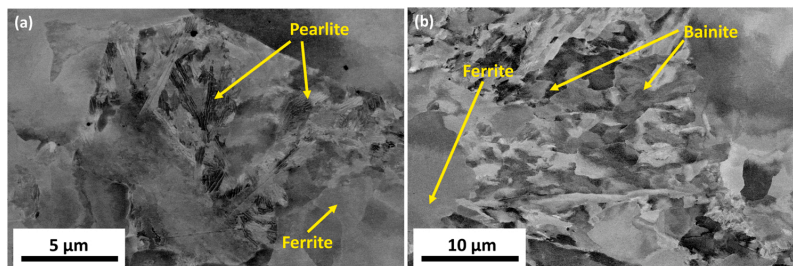


Fig. 3. SEM micrographs at (a) 5,000X and (b) 10,000X magnifications revealing the microstructure of the studied steel, which consisted of ferrite, pearlite, and bainite.

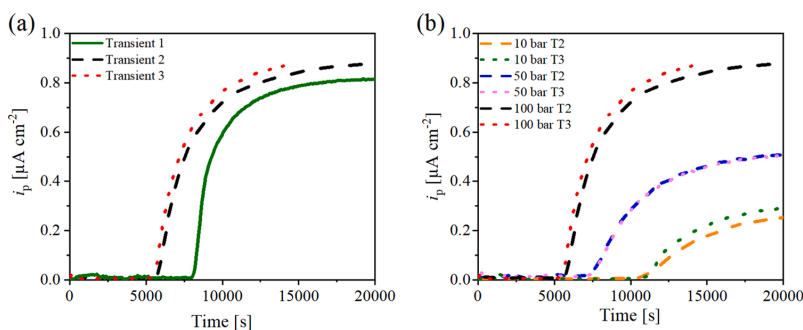


Fig. 4. (a) Three transients performed at 100 bar of hydrogen pressure. (b) Transient 2 and 3 at 10, 50, and 100 bar of hydrogen pressure. T2 – transient 2, T3 – transient 3.

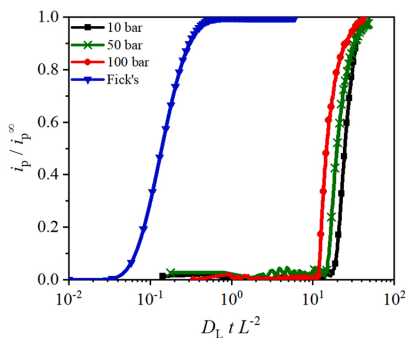


Fig. 5. Normalised gas permeation transients and prediction of Fick's 2nd law for lattice diffusion in bcc iron.

Table 2

Parameters determined by the gas permeation test. The values represent average values obtained from transients 2 and 3.

p_{H_2} [bar]	$D_{eff}(t_b)$ [$cm^2 s^{-1}$]	$D_{eff}(t_{lag})$ [$cm^2 s^{-1}$]
10	$2.21 \times 10^{-7} \pm 0.01$	$4.25 \times 10^{-7} \pm 0.01$
50	$2.47 \times 10^{-7} \pm 0.01$	$5.66 \times 10^{-7} \pm 0.01$
100	$3.23 \times 10^{-7} \pm 0.03$	$7.53 \times 10^{-7} \pm 0.03$

higher than $D_{eff}(t_b)$ for all p_{H_2} , thus confirming the inference made from the normalised transients, that the effective diffusivity changes during permeation transients [35,36,38,39].

3.2.2. Electrochemical permeation

The three electrochemical permeation transients obtained at $-15 mA cm^{-2}$ are presented in Fig. 6(a). As was observed with gas charging, t_b of the first transient was higher than that of the subsequent transients, indicating irreversible trapping. Fig. 6(b) presents the second and third transients obtained at different levels of i_c . t_b decreases and i_p^{sp} increases with increasing i_c . Deviation between transients 2 and 3 at $-1 mA cm^{-2}$ and $-50 mA cm^{-2}$ can be observed, which indicate that the surface conditions during electrochemical charging are not as stable as those during hydrogen gas charging.

The normalised hydrogen flux, as a function of the normalised time for electrochemical permeation transients, is presented in Fig. 7, including the prediction of Fick's 2nd law, which was calculated using the lattice diffusivity of bcc iron. The trends are similar to those observed during gas charging. The normalised permeation transients are shifted toward the right and are steeper than that predicted by Fick's 2nd law.

The average values for D_{eff} determined by the t_b and t_{lag} methods for different i_c are provided in Table 3. D_{eff} increases with an increase in i_c . $D_{eff}(t_b)$ ranges from 1.95×10^{-7} to $3.61 \times 10^{-7} cm^2 s^{-1}$, while $D_{eff}(t_{lag})$ ranges from $5.24 \times 10^{-7} cm^2 s^{-1}$ to $6.73 \times 10^{-7} cm^2 s^{-1}$. $D_{eff}(t_{lag})$ is 1.8 – 2.7 times higher than $D_{eff}(t_b)$ for all i_c .

3.2.3. Partial permeation transients

As the values of D_{eff} presented above appear to be significantly affected by reversible trapping, D_{eff} was determined via electrochemical partial permeation transients. The normalised partial permeation transient build-up and decay between i_c values of $-6 mA cm^{-2}$ and $-7 mA cm^{-2}$ are presented in Fig. 8(a) and (b), respectively. The best fits of the analytical solutions to Fick's 2nd law (Eqs. (3) and (4)) are included. MATLAB was used for the fitting. A good fit indicates that, in contrast to the complete permeation transient, the hydrogen diffusivity

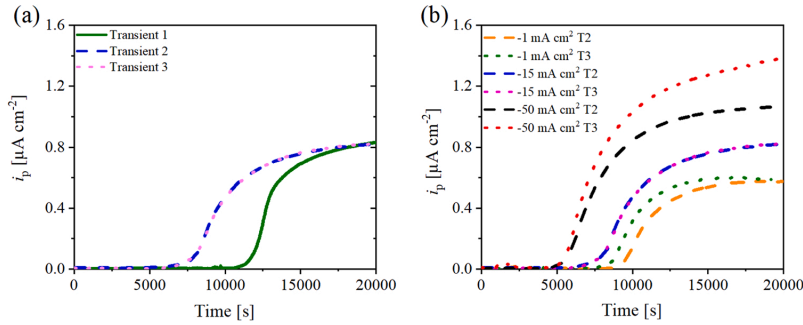


Fig. 6. (a) Three transients performed at a charging current density of -15 mA cm^{-2} charging current density during the electrochemical permeation test. (b) Transients 2 and 3 performed at -1 , -15 and -50 mA cm^{-2} . T2 – transient 2, T3 – transient 3.

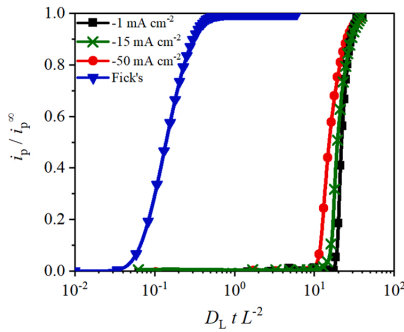


Fig. 7. Normalised electrochemical permeation transients and prediction of Fick's 2nd law for lattice diffusion in bcc iron.

Table 3
Average values for D_{eff} , as determined by the electrochemical permeation test.

$i_c [\text{mA cm}^{-2}]$	$D_{\text{eff}} (t_b) [\text{cm}^2 \text{ s}^{-1}]$	$D_{\text{eff}} (t_{\text{tag}}) [\text{cm}^2 \text{ s}^{-1}]$
-1	$1.95 \times 10^{-7} \pm 0.08$	$5.24 \times 10^{-7} \pm 0.23$
-15	$2.22 \times 10^{-7} \pm 0.01$	$5.43 \times 10^{-7} \pm 0.01$
-50	$3.61 \times 10^{-7} \pm 0.45$	$6.73 \times 10^{-7} \pm 0.09$

between the aforementioned two charging conditions can be represented by Fick's 2nd law [41,43]. The best fit of D_{eff} to the build-up curve is $1.68 \times 10^{-6} \text{ cm}^2 \text{ s}^{-1}$, while the best fit to the decay curve is $1.55 \times 10^{-6} \text{ cm}^2 \text{ s}^{-1}$. An average value of $1.6 \times 10^{-6} \text{ cm}^2 \text{ s}^{-1}$ is denoted as $D_{\text{eff}}(\text{PT})$.

3.3. Hydrogen uptake

3.3.1. Uptake from gas permeation

C_{OR} values at different p_{H_2} obtained from different calculation methods are presented in Table 4. These values depend on the calculation method. D_{eff} changes during complete permeation transients; hence, the $C_{\text{OR}}(t_b)$ and $C_{\text{OR}}(t_{\text{tag}})$ values appear different. The $C_{\text{OR}}(t_b)$ values are 1.9 – 2.3 times higher than the $C_{\text{OR}}(t_{\text{tag}})$ values for all p_{H_2} . During stepwise charging, the partial transients could be fitted to Fick's 2nd law. Thus, it can be argued that the value of C_{OR} calculated from Eq. (5) using i_p^{∞} from the complete permeation transient and $D_{\text{eff}}(\text{PT})$ represents the best measure of C_{OR} and is denoted as $C_{\text{OR}}(\text{PT})$. At p_{H_2} of 10, 50, and 100 bar, $C_{\text{OR}}(\text{PT})$ was 0.047, 0.082 and 0.137 wppm,

Table 4
 C_{OR} determined by different methods from gas permeation. The values represent average values of transients 2 and 3.

$p_{\text{H}_2} [\text{bar}]$	$f_{\text{H}_2} [\text{bar}]$	$C_{\text{OR}} (t_b) [\text{wppm}]$	$C_{\text{OR}} (t_{\text{tag}}) [\text{wppm}]$	$C_{\text{OR}} (\text{PT}) [\text{wppm}]$
10	10.1	0.341 ± 0.011	0.183 ± 0.001	0.047 ± 0.002
50	51.6	0.529 ± 0.002	0.231 ± 0.001	0.082 ± 0.000
100	106.7	0.681 ± 0.011	0.295 ± 0.001	0.137 ± 0.002

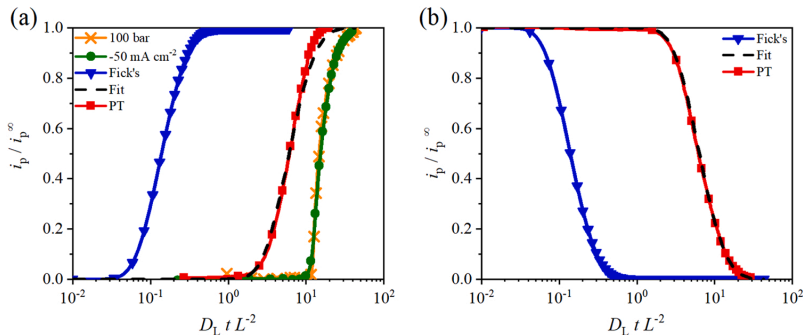


Fig. 8. (a) Normalised build-up partial permeation transients from -6 mA cm^{-2} to -7 mA cm^{-2} with best fit to Eq. (3). Normalised transients at one hundred bar, -50 mA cm^{-2} and a prediction of Fick's 2nd law for lattice diffusion in bcc iron are included for comparison. (b) Normalised decay permeation transients from -7 mA cm^{-2} to -6 mA cm^{-2} with the best fit to Eq. (4). PT – partial transient.

respectively. Sieverts' law, Eq. (6), states that the concentration of dissolved hydrogen in a metal is proportional to the square root of f_{H_2} in a charging atmosphere [51]. At a steady-state, C_0 is proportional to C_{OR} [52]; thus, Sieverts' law is also valid for C_{OR} . The hydrogen fugacity can be calculated from the hydrogen partial pressure using the Able-Noble equation of state, Eq. (7), where b denotes a constant ($1.584 \times 10^{-5} \text{ m}^3 \text{ mol}^{-1}$), T denotes the temperature in K, and R denotes the gas constant ($8.314 \text{ J K}^{-1} \text{ mol}^{-1}$) [20]. The linearity between C_{OR} and $f_{H_2}^{1/2}$, observed in Fig. 9, is in agreement with Sieverts' law. Sieverts' constant, S , determined from the linear regression line, has a value of $0.0125 \text{ wppm bar}^{-1/2}$.

$$C_0 = S \times \sqrt{f_{H_2}} \quad (6)$$

$$f_{H_2} = p_{H_2} \exp\left(\frac{p_{H_2} b}{RT}\right) \quad (7)$$

3.3.2. Uptake from electrochemical permeation

C_{OR} values at different i_c obtained from different calculation methods are listed in Table 5. As was observed with gas charging, C_{OR} values appear to be dependent on the calculation method. $C_{OR}(t_b)$ values are 1.9–2.7 times higher than $C_{OR}(t_{ag})$ values for all i_c . Additionally, the $C_{OR}(t_b)$ values are 4.6–8.2 times higher than $C_{OR}(PT)$, and the $C_{OR}(t_{ag})$ values are 2.3–3.1 times higher than $C_{OR}(PT)$. At -1 , -15 , and -50 mA cm^{-2} , $C_{OR}(PT)$ is 0.090 , 0.129 , and 0.189 wppm , respectively. $C_{OR}(PT)$ is proportional to $i_c^{1/2}$, as presented in Fig. 10.

3.3.3. Equivalent fugacity

$f_{H_2}^{eq}$ was determined using the method described by Venezuela et al. [21,22] and Liu et al. [23]. The values of $C_{OR}(PT)$ determined from electrochemical charging were inserted into Eq. (6), and the equation was solved for f_{H_2} to determine $f_{H_2}^{eq}$. S determined from gas charging, $0.0125 \text{ ppm bar}^{-1/2}$, was used in the calculations. Fig. 11 presents the $C_{OR}(PT)$ values determined from electrochemical charging superimposed onto the linear regression line corresponding to Sieverts' law. The equivalent hydrogen charging pressure, $p_{H_2}^{eq}$, was determined by solving Eq. (7) iteratively using the Newton-Raphson method. The values of $f_{H_2}^{eq}$ and $p_{H_2}^{eq}$ are listed in Table 6. i_c values of -1 , -15 , and -50 mA cm^{-2} correspond to $f_{H_2}^{eq}$ values of 49.1 , 101.9 , and 222.7 bar , respectively.

The value of η is determined using Eq. (8). E_c denotes the average measured potential on the charging side, and E_H^0 denotes the equilibrium potential for a hydrogen evolution reaction in solution under standard state conditions, as described by Eq. (9) [19,53]. The average measure η at -1 , -15 and -50 mA cm^{-2} was -593 ± 3 , -1133 ± 23 , and $-2023 \pm 74 \text{ mV}$, respectively.

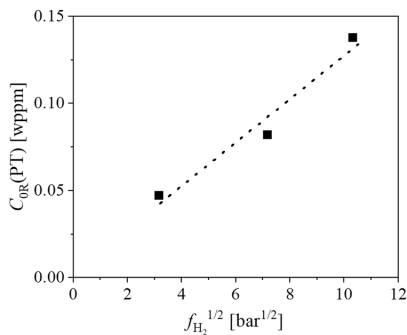


Fig. 9. Sub-surface hydrogen concentration $C_{OR}(PT)$ versus the square root of hydrogen charging fugacity.

Table 5

C_{OR} values determined by different methods from electrochemical permeation. The values represent averages values of transients 2 and 3.

i_c [mA cm^{-2}]	$C_{OR}(t_b)$ [wppm]	$C_{OR}(t_{ag})$ [wppm]	$C_{OR}(PT)$ [wppm]
-1	0.740 ± 0.016	0.276 ± 0.007	0.090 ± 0.002
-15	0.929 ± 0.011	0.370 ± 0.007	0.129 ± 0.001
-50	0.864 ± 0.219	0.450 ± 0.065	0.189 ± 0.025

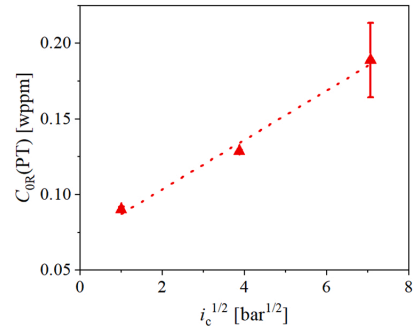


Fig. 10. Sub-surface hydrogen concentration $C_{OR}(PT)$ versus the square root of charging current density.

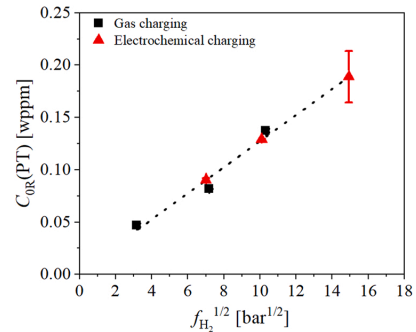


Fig. 11. Sub-surface hydrogen concentration $C_{OR}(PT)$ versus the square root of the hydrogen fugacity along with values obtained from electrochemical charging superimposed onto the best linear fit of gaseous charging.

Table 6

Equivalent hydrogen pressure and equivalent hydrogen fugacity.

i_c [mA cm^{-2}]	$C_{OR}(PT)$ [wppm]	$p_{H_2}^{eq}$ [bar]	$f_{H_2}^{eq}$ [bar]
-1	0.090 ± 0.002	47.6	49.1
-15	0.129 ± 0.001	95.9	101.9
-50	0.189 ± 0.025	196.4	222.7

$$\eta = E_c - E_H^0 \quad (8)$$

$$E_H^0 = -0.0591 \times \text{pH} - 0.0295 \log f_{H_2} \quad (9)$$

The mathematical relationship between $f_{H_2}^{eq}$ and η was determined using the approach described by Atrens et al. [18] and Liu et al. [19]. Thorough analyses of the development of a mathematical expression for the relationship between $f_{H_2}^{eq}$ and η during electrochemical permeation tests can be found elsewhere [18,19,54,55]. In short, the Nernst equation can be used to relate $f_{H_2}^{eq}$ to η , as indicated in Eq. (10). A and ξ denote

parameters that can be determined experimentally using the relations provided in Eqs. (11) and (12), respectively.

$$f_{\text{H}_2}^{\text{cqi}} = A \exp\left(\frac{-\eta F}{\xi RT}\right) \quad (10)$$

$$\xi = -\frac{1}{2} \frac{F}{R T} \frac{\delta \eta}{\delta \ln i_p^\infty} \quad (11)$$

$$i_p^\infty = \frac{FDS}{L} \left(A \exp\left(\frac{-\eta F}{\xi RT}\right) \right)^{1/2} \quad (12)$$

The constants ξ and A , as well as $D_{\text{eff}}(\text{PT})$ and S determined in this study, were substituted into Eq. (10). The mathematical relation between the $f_{\text{H}_2}^{\text{cqi}}$ and η is described by Eq. (13). It should be emphasized that galvanostatic charging was used in this study, and η was determined from the average potential measured during the transients.

$$f_{\text{H}_2}^{\text{cqi}} = 32.19 \exp\left(\frac{-\eta F}{38.81 RT}\right) \quad (13)$$

4. Discussion

The aim of this study was to determine the relationship between hydrogen gas charging and electrochemical charging. $f_{\text{H}_2}^{\text{cqi}}$ was determined as a function of η under the assumption that different charging conditions producing equal concentrations of hydrogen in steel are equivalent. To compare the severity of electrochemical and gaseous hydrogen charging conditions based on the hydrogen permeation technique, it is necessary to have an accurate measure of the sub-surface hydrogen concentration. Because the calculation of C_{OR} depends on D_{eff} , it is important to carefully evaluate D_{eff} . Detailed discussions on hydrogen diffusion and uptake are presented in the following sections.

4.1. Hydrogen diffusivity

The normalised permeation transients (Figs. 5 and 7) were shifted to the right and steeper than predicted by Fick's 2nd law. A normalised transient that is shifted to the right along the x-axis indicates slower diffusion than lattice diffusion, while a slope that deviates from Fick's 2nd law indicates that the diffusion coefficient appears to increase during the transient due to significant reversible trapping (steeper slope) or that the surface conditions are unsteady (less steep slope) [36,38,39]. Hence, the observed effects on the normalised transients reveal that a significant change in reversible trap occupancy affected both the electrochemical and gaseous permeation transients. It was also evident from the difference between $D_{\text{eff}}(t_b)$ and $D_{\text{eff}}(t_{\text{lag}})$ that significant trap occupancy caused D_{eff} to change during the permeation transients. For all tests, the value of $D_{\text{eff}}(t_b)$ was smaller than $D_{\text{eff}}(t_{\text{lag}})$. Hence, the probability of diffusing hydrogen being trapped is lowest at t_{lag} , and the effective diffusivity appears faster [7]. Because D_{eff} appears to change during a transient, it does not have a theoretical basis in Fick's 2nd law [36,38,39].

Essentially, t_b should be independent of the magnitude of the hydrogen flux through a sample [56]. However, it is evident from Figs. 4 (b) and 6(b) that t_b decreases with increasing p_{H_2} and i_c . A decrease in t_b with an increase in i_c has been previously reported [30,49]. The reduced value of t_b is attributed to a higher flux of hydrogen diffusing through the material, which causes traps to be occupied at a faster rate. Thus, the impediment to hydrogen transport caused by traps is more pronounced when the hydrogen flux is low. It is evident from Tables 2 and 3 that the D_{eff} values are dependent on the charging conditions. Fig. 12 presents D_{eff} values as a function of i_p^∞ . A similar relationship between C_0 and D_{eff} was predicted by Griffiths and Turnbull [35] using theoretical calculations based on electrochemical permeation results obtained from three low alloy steels. C_0 is proportional to i_p^∞ ; thus, it is expected that the

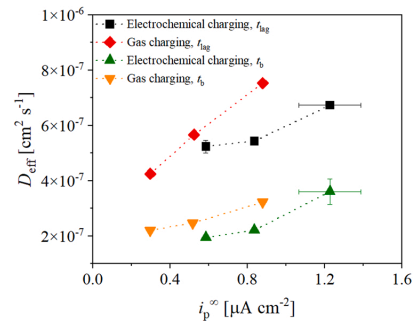


Fig. 12. Effective diffusion coefficients, $D_{\text{eff}}(t_b)$ and $D_{\text{eff}}(t_{\text{lag}})$, as a function of the steady-state permeation current density, i_p^∞ .

dependency of D_{eff} on the concentration follows the same trend. D_{eff} obtained from gaseous charging is slightly larger than those obtained from electrochemical permeation, compared to that during gaseous permeation (10:1). A smaller radius to thickness ratio can cause deviation from the assumption of one-dimensional diffusion due to increasing influence of lateral diffusion. According to the study by Hutchings et al. [57], a radius to thickness ratio of 10:1 and 5:1 can cause a deviation of less than 5% and about 10%, respectively, when one-dimensional diffusion is assumed. Owing to the concentration dependency of D_{eff} , the effective diffusivity should not be treated as an intrinsic material property unless the trap occupancy is very low [7]. The concentration dependence of the effective diffusivity underlines the importance of performing tests in charging conditions comparable to the operating conditions.

Because $D_{\text{eff}}(t_b)$ and $D_{\text{eff}}(t_{\text{lag}})$ were significantly affected by the change in trap occupancy, partial permeation transients were performed. This approach caused a smaller disturbance to the equilibrium between the lattice and trapped hydrogen, that is, the change in the trap occupancy was small [41]. This method could, as reported in the literature, be used to determine D_L of hydrogen in bcc iron [41]. Partial permeation transients have also been applied to X65 low alloy steels, where the reported value of D_L is in the order of $1-3 \times 10^{-6} \text{ cm}^2 \text{ s}^{-1}$ [44]. The diffusion coefficient determined by the partial transient in this study was approximately $1.6 \times 10^{-6} \text{ cm}^2 \text{ s}^{-1}$, with the same order of magnitude as that reported for X65 low alloy steel. However, even with a minimal change in trap occupancy, the effect of reversible traps was not completely eliminated in this study. Thus, the diffusion coefficient obtained from the partial transients was regarded as an effective value. However, $D_{\text{eff}}(\text{PT})$ is in this case regarded as the best measure of hydrogen diffusivity in steady-state conditions.

4.2. Hydrogen uptake

Two charging conditions resulting in the same hydrogen activity below the steel surface are considered to be equivalent [19]. As explained above, the complete permeation transients could not be fit to Fick's 2nd law; thus, the determination of $C_{\text{OR}}(t_b)$ and $C_{\text{OR}}(t_{\text{lag}})$ does not have a theoretical basis. In such a case, C_{OR} obtained from the t_b and t_{lag} methods can be overestimated by a factor of 2.5–5 [40]. As observed in Fig. 8(a) and (b), the effects produced by changes in trap occupancy are reduced when performing partial permeation transients to an extent such that the transients agree well with Fick's 2nd law. $D_{\text{eff}}(\text{PT})$ obtained from partial transients and i_p^∞ obtained from the complete permeation transient were used to calculate $C_{\text{OR}}(\text{PT})$ using Eq. (5). As $D_{\text{eff}}(\text{PT})$ was considered the best measure of hydrogen diffusivity in a steady-state, $C_{\text{OR}}(\text{PT})$ was used to determine $f_{\text{H}_2}^{\text{cqi}}$. It has been argued that C_0 is the best measure of the severity of charging conditions [7]. To determine C_0 ,

it is often considered that the hydrogen flux in a steady-state is equal to the lattice hydrogen flux and D_L in bcc iron is substituted into Eq. (5). In this study, reversible trapping was so significant that this assumption was not made. However, because a single value of D_{eff} is used to determine $C_{OR}(PT)$, whether C_0 or $C_{OR}(PT)$ forms the basis for comparison does not affect the relationship between $f_{H_2}^{eq}$ and η .

The determination of $f_{H_2}^{eq}$ as a function of η by hydrogen permeation requires the following conditions to be satisfied: (i) Sieverts' law must apply to both gas charging and electrochemical charging, (ii) equilibrium conditions must exist on the charging side, and (iii) the permeation transients must be described by Fick's 2nd law [19]. The linearity of C_{OR} with both $p_{H_2}^{1/2}$ and $i_c^{1/2}$ indicates that Sieverts' law applies to both electrochemical and gas charging. The linear dependence between C_{OR} and $i_c^{1/2}$, as presented in Fig. 10, is attributed to the balance between charging and chemical recombination [52]. Equilibrium conditions on the charging side were obtained by eliminating surface effects that impeded hydrogen uptake. During gas charging, a Pd coating was applied to the charging side, as air-formed surface oxides can cause surface impedance to hydrogen uptake from hydrogen gas [27,34]. Pd coatings have been reported to eliminate the impeding effect of surface oxides and ensure equilibrium between the gas and metal phases, according to Sieverts' law [11,25,27,34]. However, a few studies on hydrogen gas permeation have not mentioned the use of Pd coatings on the charging side [9,10,58]. The linear dependence between $C_{OR}(PT)$ and $p_{H_2}^{1/2}$ with an intercept close to the origin indicates that the Pd coating ensure equilibrium conditions on the charging side and that the Pd coated surface represents the hydrogen uptake of a bare steel surface (for instance in a growing crack tip).

During electrochemical hydrogen permeation, the second and third permeation transients were less coincident (Fig. 6(b)) than those of gas charging (Fig. 4(b)), especially when charging at -50 mA cm^{-2} . This indicated that the surface conditions were less stable during electrochemical charging. One possible explanation for this is that the surface conditions were slightly different between the transients, as the sample was removed from the cell and ground, which was not the case for gas charging. The largest deviation between transients 2 and 3 was observed during charging at -50 mA cm^{-2} . Corrosion has been reported to take place under high cathodic current densities, possibly due to extensive evolution of hydrogen bubbles disturbing local electrochemical conditions [29,30]. Air-formed oxides could impede hydrogen uptake also during electrochemical charging; however, it has been reported that the oxides can be reduced during the early stage of hydrogen permeation on the order of minutes to one hour in NaOH solution [28,29]. If this were the case here, the air-formed oxide would be reduced faster than t_p such that the removal of surface oxides could affect the shape of the transient without affecting i_p^{eq} . If the shape of the electrochemical transient was affected by an air-formed oxide, it can be an additional explanation to why D_{eff} is slightly smaller for electrochemical permeation than for gas permeation at equal i_p^{eq} , as observed in Fig. 12. In addition, blisters and surface cracks can be formed under severe charging conditions but are more likely to form in acidic solutions with added hydrogen recombination poisons [31,32]. The linear dependence of $C_{OR}(PT)$ on $i_c^{1/2}$ indicated equilibrium conditions on the charging side. Combined with the partial transients following Fick's 2nd law, conditions (i), (ii), and (iii) were considered as satisfied.

An advantage of determining $f_{H_2}^{eq}$ using both gas charging and electrochemical permeation is that through gas charging, one can determine S for the specific material investigated. S is necessary to determine $f_{H_2}^{eq}$ as a function of η using Eq. (10), and a difference in S can significantly affect the relationship between $f_{H_2}^{eq}$ and η determined by electrochemical hydrogen permeation. S of pure bcc iron is approximately $5.3 \times 10^{-4} \text{ wppm bar}^{-1/2}$ [19,50], which is approximately two orders of magnitude lower than the value obtained in this study. For a 3.5NiCrMoV steel

specimen, S was reported to be $0.0272 \text{ wppm bar}^{-1/2}$ [22], which is approximately twice the value determined in this study. In materials with low solubility and high diffusivity, such as low carbon steels, it can be challenging to conduct accurate measurements with TDS. A substantial amount of hydrogen can egress between hydrogen charging and analysis, and it may be necessary to estimate the amount of effused hydrogen during this dwell time [22,59]. Using the permeation technique, small fluxes of hydrogen can be detected simultaneously with hydrogen exposure on the charging side, rendering this an advantageous method for samples with low solubility and high diffusivity.

A summary of previous studies including the current study, which determined $f_{H_2}^{eq}$ as a function of η , is presented in Fig. 13 [19,21,23,54,60]. The plot illustrates different charging methods that can represent equal hydrogen activities. However, the relationship between $f_{H_2}^{eq}$ and η is, to a large extent, specific to the electrolyte and the investigated alloy owing to the variation in the microstructure and surface conditions that affect hydrogen evolution [21]. This is further demonstrated by comparing the results of this study with the values obtained by Venezuela et al. [21] for a martensitic advanced high-strength steel, which was also charged in a 3.5 wt% NaCl solution and obtained a similar magnitude of $f_{H_2}^{eq}$ but at a lower η . The results obtained Liu et al. [23] for a dual phase steel in 3 wt% NaCl are comparable to that obtained by Venezuela et al. [21], both studies using a TDS based approach. Crolet and Maisonneuve [60] obtained a lower $f_{H_2}^{eq}$ when charging a low carbon steel walled hollow sensor in a 5 wt% NaCl solution, compared to the other studies that performed charging in NaCl solutions. A change in the slope was observed in results of certain studies presented in Fig. 13, which was attributed to a change in the hydrogen evolution reaction mechanism [19,54]. This change in the slope was not observed in this study; however, it may occur outside the tested range of η . A change in the slope at lower η could bring the $f_{H_2}^{eq}$ closer to the value obtained by Crolet and Maisonneuve. As a change in the slope may occur outside the tested range of η , the relationship between $f_{H_2}^{eq}$ and η may not be valid outside the investigated range.

The determined relationship between $f_{H_2}^{eq}$ and η for the investigated steel specimen (Eqs. (6) and (13)) is related to the hydrogen uptake of bare metal surface, as the influence of an oxide layer is eliminated by using a Pd-coated surface during gas charging. The nature of failure can make it difficult to make direct comparisons between investigations of HE susceptibility performed with different charging methods [6]; thus,

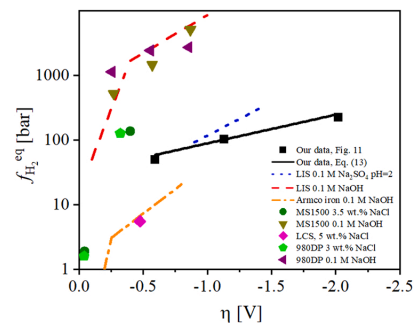


Fig. 13. Equivalent fugacity, $f_{H_2}^{eq}$, versus overpotential, η . Included data: Study conducted by Liu et al. [19] on low interstitial steel (LIS) charged in both 0.1 M NaOH and acidified 0.1 M Na_2SO_4 ($\text{pH} = 2$) in permeation tests; Study conducted by Venezuela et al. [21] on MS1500 martensitic advanced high-strength steels charged in 0.1 M NaOH and 3.5 wt% NaCl; Study conducted by Liu et al. [23] on 98DP dual phase steels charged in 0.1 M NaOH and 3 wt% NaCl; Study conducted by Crolet and Maisonneuve [60] on low carbon steel (LCS) in 5 wt% NaCl; Data collected by Bockris et al. [54] on ArmoCo iron in 0.1 M NaOH with the relationship deduced by Liu et al. [19].

the determined equivalency between charging methods and hydrogen uptake may not translate to mechanical testing. Validation of equivalence between charging methods and hydrogen uptake using mechanical testing requires thorough design. For instance, during HE investigation by mechanical testing, hydrogen uptake between gaseous and electrochemical charging at equivalent fugacity may differ initially due to the surface impedance of the oxide layer. However, strain will cause breakage of the oxide film [6], which will expose the bare steel surface to the hydrogen gas and uptake will proceed according to Sieverts' law. Surface oxides prepared on a steel surface can inhibit hydrogen uptake, however, the efficiency is dependent on the nature of the oxide film as hydrogen uptake take place through pores and cracks [10]. Similarly, naturally formed oxide layers present during in-service conditions may act as a barrier to hydrogen uptake. Thus, further work is necessary to investigate the equivalency between investigations of HE susceptibility using different charging methods, and hydrogen uptake under in-service conditions.

5. Conclusion

In this study, the hydrogen permeation technique was used to investigate the hydrogen uptake and diffusivity under different charging conditions. Electrochemical and gaseous hydrogen charging were conducted. The sub-surface hydrogen concentration in lattice and reversible trap sites were used to compare the severity of the charging conditions, and to determine the relationship between the equivalent hydrogen fugacity and overpotential. Additionally, the dependence of the effective diffusivity of hydrogen on the charging conditions was investigated. Partial permeation transients were performed to reduce the effect of trapping on permeation transients. The primary findings are summarised as follows:

- The sub-surface hydrogen concentration in lattice and reversible trap sites, C_{OR} , increased linearly with the square root of both the hydrogen gas charging fugacity and charging current density.
- The effective diffusion coefficient, D_{eff} , determined via the breakthrough time method and the time lag method was dependent on the charging conditions owing to significant reversible trapping. Its values were found to lie in the range of $2\text{--}8 \times 10^{-7} \text{ cm}^2 \text{ s}^{-1}$ at room temperature. Performing partial permeation transients reduced the effects produced by changes in trap occupancy to the extent that the permeation transients followed Fick's 2nd law. The value of D_{eff} determined by partial permeation transients was in the order of $1.6 \times 10^{-6} \text{ cm}^2 \text{ s}^{-1}$ at room temperature.
- A relationship between the equivalent hydrogen fugacity and overpotential was deduced. During gaseous hydrogen charging, a Pd coating was utilised to overcome the surface impedance which can be caused by an oxide layer. Further work is necessary to investigate the equivalence of charging methods during mechanical testing, and hydrogen uptake from hydrogen gas where naturally formed surface oxides are present.

CRedit authorship contribution statement

Erik Koren: Conceptualization, Methodology, Formal analysis, Investigation, Data curation, Writing – original draft. **Catalina Hoem Musinoi Hagen:** Conceptualization, Methodology, Investigation, Writing – review & editing. **Dong Wang:** Supervision, Investigation, Writing – review & editing. **Xu Lu:** Conceptualization, Writing – review & editing. **Roy Johnsen:** Supervision, Conceptualization, Writing – review & editing. **Junichiro Yamabe:** Conceptualization, Writing – review & editing.

Declaration of Competing Interest

The authors declare that they have no known competing financial

interests or personal relationships that could have appeared to influence the work reported in this paper.

Data availability

The data that has been used is confidential.

Acknowledgements

This work has been supported by the Research Council of Norway and the industry company partners through the HyLINE project (294739).

References

- [1] European Commission, A hydrogen strategy for a climate-neutral Europe, 2020.
- [2] C. Yang, J. Ogden, Determining the lowest-cost hydrogen delivery mode, *Int. J. of Hydrog. Energy* 32 (2) (2007) 268–286.
- [3] J.R. Fekete, J.W. Sowards, R.L. Amaro, Economic impact of applying high strength steels in hydrogen gas pipelines, *Int. J. of Hydrog. Energy* 40 (33) (2015) 10547–10558.
- [4] S. Cerniauskas, A.J.C. Junco, T. Grube, M. Robinius, D. Stolten, Options of natural gas pipeline reassignment for hydrogen: cost assessment for a Germany case study, *Int. J. of Hydrog. Energy* 45 (21) (2020) 12095–12107.
- [5] W.H. Johnson, On Some, Remarkable changes produced in iron and steel by the action of hydrogen and acids, *Proc. R. Soc. Lond.* 23 (156–163) (1874) 168–179.
- [6] N.E. Nanninga, Y.S. Levy, E.S. Drexler, R.T. Condon, A.E. Stevenson, A.J. Slička, Comparison of hydrogen embrittlement in three pipeline steels in high pressure gaseous hydrogen environments, *Corros. Sci.* 59 (2012).
- [7] A. Turnbull, 4 - Hydrogen diffusion and trapping in metals, in: R.P. Gangloff, B. P. Somerday (Eds.), *Gaseous Hydrogen Embrittlement of Materials in Energy Technologies 1*, Woodhead publishing series in metals and surface engineering, 2012, pp. 89–128.
- [8] S. Lynch, Hydrogen embrittlement phenomena and mechanisms, *Corros. Rev.* 30 (3) (2012) 105–123.
- [9] S. Zhang, J. Li, T. An, S. Zheng, K. Yang, L. Lv, C. Xie, L. Chen, L. Zhang, Investigating the influence mechanism of hydrogen partial pressure on fracture toughness and fatigue life by in-situ hydrogen permeation, *Int. J. Hydrog. Energy* 46 (39) (2021) 20621–20629.
- [10] T. Zhang, W. Zhao, Y. Zhao, K. Ouyang, Q. Deng, Y. Wang, W. Jiang, Effects of surface oxide films on hydrogen permeation and susceptibility to embrittlement of X80 steel under hydrogen atmosphere, *Int. J. of Hydrog. Energy* 43 (6) (2018) 3353–3365.
- [11] P. Castaño Rivera, V.P. Ramunni, P. Bruzzoni, Hydrogen trapping in an API 5L X60 steel, *Corros. Sci.* 54 (2012) 106–118.
- [12] I. Moro, L. Briottet, P. Lemoine, E. Andrieu, C. Blanc, G. Odemer, J. Chêne, F. Jambon, Damage under high pressure hydrogen environment of a high strength pipeline steel X80. *Effects of Hydrogen on Materials*, ASM International, 2008, pp. 357–364.
- [13] K. Xu, M. Rana, Tensile and fracture properties of carbon and low alloy steels in high pressure hydrogen. *Effects of Hydrogen on Materials*, ASM International, 2008.
- [14] D. Stalheim, T. Boggess, C. San Marchi, S. Jansto, B. Somerday, G. Muralidharan, & P. Sofronis, Microstructure and Mechanical Property Performance of Commercial Grade API Pipeline Steels in High Pressure Gaseous Hydrogen. *Proceedings of the 2010 8th International Pipeline Conference*, ASME, Volume 2, pp. 529–537, 2010.
- [15] T. An, H. Peng, P. Bai, S. Zheng, X. Wen, L. Zhang, Influence of hydrogen pressure on fatigue properties of X80 pipeline steel, *Int. J. Hydrog. Energy* 42 (23) (2017).
- [16] E.S. Drexler, A.J. Slička, R.L. Amaro, N. Barbosa, D.S. Lauria, L.E. Hayden, D. G. Stalheim, Fatigue crack growth rates of API X70 pipeline steel in a pressurized hydrogen gas environment, *Fatigue Fract. Eng. Mater. Struct.* 37 (2014).
- [17] G.B. Rawls, T. Adams, N.L. Newhouse, 1 - Hydrogen production and containment, in: P.R. Gangloff, B.P. Somerday (Eds.), *Gaseous hydrogen embrittlement of materials in energy technologies 2*, Woodhead publishing series in metals and surface engineering, 2012.
- [18] A. Atrens, D. Mezzanotte, N.F. Fiore, M.A. Genshaw, Electrochemical studies of hydrogen diffusion and permeability in Ni, *Corros. Sci.* 20 (5) (1980) 673–684.
- [19] Q. Liu, A.D. Atrens, Z. Shi, K. Verbeke, A. Atrens, Determination of the hydrogen fugacity during electrolytic charging of steel, *Corros. Sci.* 87 (2014) 239–258.
- [20] C. San Marchi, B. Somerday, S. Robinson, Permeability, solubility and diffusivity of hydrogen isotopes in stainless steels at high gas pressures, *Int. J. of Hydrog. Energy* 32 (1) (2007) 100–116.
- [21] J. Venezuela, E. Gray, Q. Liu, Q. Zhou, C. Tapia-Bastidas, M. Zhang, A. Atrens, Equivalent hydrogen fugacity during electrochemical charging of some martensitic advanced high-strength steels, *Corros. Sci.* 127 (2017) 45–58.
- [22] J. Venezuela, C. Tapia-Bastidas, Q. Zhou, T. Depover, K. Verbeke, E. Gray, Q. Liu, Q. Liu, M. Zhang, A. Atrens, Determination of the equivalent hydrogen fugacity during electrochemical charging of 3.5NiCrMoV steel, *Corros. Sci.* 132 (2018) 90–106.
- [23] Q. Liu, A. Atrens, Z. Shi, K. Verbeke, A. Atrens, Equivalent hydrogen fugacity during electrochemical charging of 980DP steel determined by thermal desorption spectroscopy, *Adv. Eng. Mater.* 20 (1) (2018).

- [24] M.A.V. Devanathan, Z. Stachurski, The adsorption and diffusion of electrolytic hydrogen in palladium, *Proc. R. Soc. Lond. Ser. A. Math. Phys. Sci.* 270 (1340) (1962) 90–102.
- [25] A.J. Kummick, H.H. Johnson, Steady state hydrogen transport through zone refined irons, *Metall. Trans. A* 6A (1975) 1087–1091.
- [26] D. Pérez Escobar, K. Verbeken, L. Duprez, M. Verhaege, Evaluation of hydrogen trapping in high strength steels by thermal desorption spectroscopy, *Materials Science & Engineering, A, Struct. Mater.: Prop., Microstruct. Process.* 551 (2012) 50–58.
- [27] J. Yamabe, T. Awane, S. Matsuoka, Investigation of hydrogen transport behavior of various low-alloy steels with high-pressure hydrogen gas, *Int. J. of Hydrog. Energy* 40 (34) (2015) 11075–11086.
- [28] T. Casanova, J. Crousier, The influence of an oxide layer on hydrogen permeation through steel, *Corros. Sci.* 38 (9) (1996) 1535–1544.
- [29] J. Flis, Changes in hydrogen entry rate and in surface of iron during cathodic polarisation in alkaline solutions, *Electrochim. Acta* 44 (23) (1999) 3989–3997.
- [30] S.M. Charca, O.N.C. Uwakweh, V.S. Agarwala, Hydrogen transport conditions and effects in cathodically polarized AF1410 steel, *Metall. Mater. Trans. A* 38 (10) (2007) 2389–2399.
- [31] D. Pérez Escobar, C. Miñambres, L. Duprez, K. Verbeken, M. Verhaege, Internal and surface damage of multiphase steels and pure iron after electrochemical hydrogen charging, *Corros. Sci.* 53 (10) (2011) 3166–3176.
- [32] M. Cauwels, R. Depraetere, W.D. Waele, S. Hertelé, T. Depover, K. Verbeken, Influence of electrochemical hydrogenation parameters on microstructures prone to hydrogen-induced cracking, *J. Nat. Gas. Sci. Eng.* 101 (2022), 104533.
- [33] A. Laureys, E. Van den Eeckhout, R. Petrov, K. Verbeken, Effect of deformation and charging conditions on crack and blister formation during electrochemical hydrogen charging, *Acta Mater.* 127 (2017) 192–202.
- [34] A. Nagao, N. Ishikawa, S. Takagi, M. Kimura, Hydrogen uptake in steels exposed to high pressure H₂ gas, in: B.P. Somerday, Sofronis (Eds.), *International hydrogen conference (IHC2016): Materials performance in hydrogen environments*, P. ASME Press, 2017.
- [35] A.J. Griffiths, A. Turnbull, On the effective diffusivity of hydrogen in low alloy steels, *Corros. Sci.* 37 (11) (1995) 1879–1881.
- [36] ISO 17081:2014 Method of measurement of hydrogen permeation and determination of hydrogen uptake and transport in metals by an electrochemical technique, *International Organization for Standardization*, 2014.
- [37] G.M. Pressouyre, I.M. Bernstein, A quantitative analysis of hydrogen trapping, *Metall. Trans. A* 9 (11) (1978) 1571–1580.
- [38] *Practice for Evaluation of Hydrogen Uptake, Permeation, and Transport in Metals by an Electrochemical Technique*, ASTM International, 2018.
- [39] E. Wu, *A Mathematical Treatment of the Electrochemical Method of Hydrogen Permeation and Its Application in Hydrogen Traps and Embrittlement*, *J. Electrochem. Soc.* 134 (1987) 2126.
- [40] L. Simoni, T. Falcade, D.C.F. Ferreira, C.E.F. Kwitniewski, An integrated experimental and modeling approach to determine hydrogen diffusion and trapping in a high-strength steel, *Int. J. of Hydrog. Energy* 46 (50) (2021) 25738–25751.
- [41] T. Zakroczyński, Adaptation of the electrochemical permeation technique for studying entry, transport and trapping of hydrogen in metals, *Electrochim. Acta* 51 (11) (2006) 2261–2266.
- [42] T. Zakroczyński, Permeability of iron to hydrogen cathodically generated in 0.1 M NaOH, *Scr. Metall.* 19 (4) (1985) 521–524.
- [43] Q. Liu, A. Atrens, Reversible hydrogen trapping in a 3.5NiCrMoV medium strength steel, *Corros. Sci.* 96 (2015) 112–120.
- [44] E. Fallahmohammadi, F. Bolzoni, L. Lazzari, Measurement of lattice and apparent diffusion coefficient of hydrogen in X65 and F22 pipeline steels, *Int. J. Hydrog. Energy* 38 (5) (2013) 2531–2543.
- [45] P. Manolatos, M. Jerome, J. Galland, Necessity of a palladium coating to ensure hydrogen oxidation during electrochemical permeation measurements on iron, *Electrochim. Acta* 40 (7) (1995) 867–871.
- [46] H. Husby, M. Iannuzzi, R. Johnsen, M. Kappes, A. Barnoush, Effect of nickel on hydrogen permeation in ferritic/pearlitic low alloy steels, *Int. J. Hydrog. Energy* 43 (7) (2018) 3845–3861.
- [47] P. Bruzzoni, *Efectos de superficie en la difusión de hidrógeno en hierro y aleaciones ferrosas*, Universidad de Buenos Aires, 2003.
- [48] P. Bruzzoni, R.M. Carranza, J.R.C. Lacoste, Influence of palladium films on hydrogen gas entry into iron: a study by electrochemical impedance spectroscopy, *Int. J. of Hydrog. Energy* (2000) 5.
- [49] S. Frappart, X. Feaugas, J. Creus, F. Thebault, L. Delattre, H. Marchebois, Study of the hydrogen diffusion and segregation into Fe–C–Mo martensitic HSLA steel using electrochemical permeation test, *J. Phys. Chem. Solids* 71 (10) (2010) 1467–1479.
- [50] K. Kiuchi, R.B. McLellan, The solubility and diffusivity of hydrogen in well-annealed and deformed iron, *Acta Metall.* 31 (7) (1983) 961–984.
- [51] C.K. Gupta, *Chemical Metallurgy: Principles and Practice*, Wiley-VCH, Weinheim, 2003, p. 273.
- [52] A. Turnbull, I. Wright, Hydrogen permeation modelling with generalised boundary conditions at the charging surface, *NPL Rep. Mat.* 69 (2014).
- [53] P. Delahay, M. Pourbaix, P.V. Rysseberghe, Potential-pH diagrams, *J. Chem. Educ.* (1950).
- [54] J.O. Bockris, J. McBreen, L. Nanis, The Hydrogen evolution kinetics and hydrogen entry into α -iron, *J. Electrochem. Soc.* 112 (10) (1965) 1025.
- [55] J.O. Bockris, P.K. Subramanyan, The equivalent pressure of molecular hydrogen in cavities within metals in terms of the overpotential developed during the evolution of hydrogen, *Electrochim. Acta* 16 (12) (1971) 2169–2179.
- [56] N. Boes, H. Züchner, Electrochemical methods for studying diffusion, permeation and solubility of hydrogen in metals, *J. Less Common Met.* 49 (1976) 223–240.
- [57] R.B. Hutchings, D.H. Ferriss, A. Turnbull, Ratio of specimen thickness to detection area for reliable hydrogen permeation measurement, *NPL Rep. DMM 1* (1993) 103.
- [58] T. Zhang, W. Xiao, E. Li, Y. Zhao, Q. Deng, Y. Wang, W. Jiang, Comparison of hydrogen embrittlement susceptibility of three cathodic protected subsea pipeline steels from a point of view of hydrogen permeation, *Corros. Sci.* 131 (2018) 104–115.
- [59] K. Verbeken, 2 - Analysing hydrogen in metals: bulk thermal desorption spectroscopy (TDS) methods, in: R.P. Gangloff, B.P. Somerday (Eds.), (eds), *Gaseous Hydrogen Embrittlement of Materials in Energy Technologies*, vol. 1, Woodhead Publishing, 2012, pp. 27–55.
- [60] J.-L. Crolet, G. Maisonneuve, Construction of a universal scale of severity for hydrogen cracking, *CORROSION 2000*, OnePetro, 2000.

Paper 2



**Investigation electrochemical charging conditions equivalent
to hydrogen gas exposure of X65 pipeline steel**

E. Koren, C. M. H. Hagen, D. Wang, X. Lu, R. Johnsen

Materials and Corrosion (2023) 1-7

DOI: <https://doi.org/10.1002/maco.202313931>

Investigating electrochemical charging conditions equivalent to hydrogen gas exposure of X65 pipeline steel

Erik Koren¹  | Catalina M. H. Hagen² | Dong Wang¹ | Xu Lu¹ | Roy Johnsen¹ 

¹Department of Mechanical and Industrial Engineering, NTNU, Trondheim, Norway

²SINTEF, Trondheim, Norway

Correspondence

Erik Koren and Xu Lu, Department of Mechanical and Industrial Engineering, NTNU, 7491 Trondheim, Norway.
Email: erik.a.koren@ntnu.no and xu.lu@ntnu.no

Funding information

Research Council of Norway,
Grant/Award Number: 294739

Abstract

In this study, we systematically investigate electrochemical hydrogen charging conditions equivalent to hydrogen gas pressures relevant for hydrogen transportation in X65 pipeline steel. By performing hydrogen gas permeation, a relationship for Sieverts' law was established, which was used in combination with electrochemical hydrogen permeation to determine the equivalent hydrogen pressure. The results revealed that cathodic protection simulated condition at $-1050 \text{ mV}_{\text{Ag}/\text{AgCl}}$ was equivalent to a hydrogen pressure of 12.3 bar. The addition of thiourea, a hydrogen recombination poison, and changing the applied potential in the cathodic direction increased the equivalent hydrogen pressure. In this way, an electrochemical charging condition equivalent to a potential hydrogen gas pressure for hydrogen transportation (200 bar) was determined.

KEYWORDS

electrochemical charging, equivalent fugacity, H_2 gas charging, hydrogen embrittlement, hydrogen permeation, pipeline steel

1 | INTRODUCTION

With hydrogen emerging as a clean energy carrier,^[1] the transportation and storage of pressurized hydrogen gas have gained recent interest,^[2–6] for example, repurposing existing natural gas pipelines for hydrogen gas transportation.^[7] Pipelines should withstand pressures in the range 150–200 bar, due to the low energy density of hydrogen gas.^[8] Hydrogen can degrade a material's mechanical properties, a phenomenon known as hydrogen embrittlement (HE).^[9] Because of safety concerns using pressurized hydrogen gas, electrochemical charging is sometimes used as a substitute for hydrogen gas exposure during investigations of HE susceptibility of a material.^[10,11]

The severity of HE effects is highly dependent on the hydrogen charging condition.^[2,12] Relating electrochemical and gaseous charging, would enhance the comparability of HE investigations performed under different charging conditions. The equivalence between electrochemical and gaseous charging has previously been investigated by hydrogen permeation,^[13–16] thermal desorption analysis,^[17–19] and by measuring the hydrogen pressure developed in a hollow sensor during charging.^[20] While these studies investigated the pressure equivalency from common electrochemical charging conditions, a systematic approach to determine electrochemical charging conditions equivalent to pressures relevant for hydrogen gas transportation is lacking.

This is an open access article under the terms of the Creative Commons Attribution License, which permits use, distribution and reproduction in any medium, provided the original work is properly cited.

© 2023 The Authors. *Materials and Corrosion* published by Wiley-VCH GmbH.

Chemical additives can enhance hydrogen absorption during electrochemical charging.^[21,22] Several mechanisms explaining the increased hydrogen absorption have been proposed, which have been discussed in detail in Protopopoff and Marcus.^[23] One prominent hypothesis is that the enhanced hydrogen absorption is caused by a chemisorbed element or species obstructing the recombination of adsorbed atomic hydrogen, hence, these additives are commonly referred to as hydrogen recombination poisons.^[24] Increasing the cathodic current density or cathodic potential are other measures to enhance hydrogen uptake,^[17,25] however, high cathodic current densities can cause unsteady surface conditions due to extensive bubble formation, changes in the local pH, or detachment of second phase particles.^[26,27] Akiyama and Li investigated the application of hydrogen recombination poison and different cathodic current densities to optimize electrochemical charging,^[22] however, its equivalence to gaseous hydrogen charging was not determined.

Herein, the objective is to optimize the electrochemical charging conditions to obtain a desired and predetermined equivalent hydrogen pressure, which simulates a potential hydrogen pressure level (200 bar) in a pipeline system aimed for hydrogen transportation.

2 | MATERIAL AND METHODS

2.1 | Material and sample preparation

The steel used in this study was API 5L X65 grade, from a quenched and tempered, seamless pipe. The wall thickness was 15.4 mm. It consisted of homogeneously distributed grains of ferrite and bainite. The phase volumes of ferrite and bainite were 89% and 11%, respectively. The average grain size was 7 μm . The chemical composition is given in Table 1. The samples were machined from a position close to the inner side of the pipe wall, parallel to the longitudinal direction. Plates with dimensions of 50 \times 150 \times 1.9 mm (width \times length \times thickness) were used for hydrogen gas charging. Disks with dimensions of 30 mm diameter and 1.1 mm thickness were used for electrochemical charging. The exposed areas during gaseous and electrochemical

charging were 16 and 3.7 cm², respectively. Both sides of all samples were prepared with SiC grinding papers to a final grade of #P1000. A Pd coating was electrodeposited on the detection side of all samples, following the method described by Husby et al.^[28] based on the work of Bruzzoni et al.^[29] and Castaño Rivera et al.^[30] Samples used for gas charging were also coated with Pd on the charging side. Pd facilitates hydrogen oxidation on the detection side,^[31] while on the charging side, Pd is applied to overcome the surface impedance which can be caused by an oxide layer during gaseous hydrogen charging.^[3,13,16]

2.2 | Hydrogen permeation tests

The hydrogen permeation experiments follow the principles first described by Devanathan and Stachurski.^[32] A detailed description of the gas permeation set-up and electrochemical permeation set-up was described in a previous paper.^[16] In the detection chamber, for both gas and electrochemical permeation, a 0.1 M NaOH solution (pH = 12.6) and an applied potential of +315 mV_{SCE} was used to ensure hydrogen oxidation. For gaseous hydrogen charging, the applied hydrogen gas pressures were 10, 50, and 100 bar. In the charging chamber, a 3.5 wt% NaCl solution (pH = 6.6) with an applied potential of -1050 mV_{Ag/AgCl} was used to simulate cathodic protection (CP) conditions. To enhance the uptake of hydrogen, thiourea (CH₄N₂S) with various concentrations (0.5–3 g L⁻¹) was added and the cathodic potential was changed in steps of 75 mV in the cathodic direction. Two charging and discharging cycles were performed for all charging conditions. All tests were performed at room temperature (21 \pm 1°C).

To determine the effective hydrogen diffusion coefficient, D_{eff} , partial permeation transients were conducted in a 3.5 wt% NaCl solution with a 2 g L⁻¹ thiourea addition. Performing partial permeation transients can reduce surface and trapping effects, such that the permeation transients can be fitted to solutions of Fick's second law.^[33] Initially, a charging potential of -1050 mV_{Ag/AgCl} was applied until a steady permeation current density was achieved. Subsequently, the applied charging potential was changed every 5500 s in the following order: -1200, -1350, -1200, and -1050 mV_{Ag/AgCl}, such that two build-up transients and two decay transients were obtained.

2.3 | Analysis

The subsurface hydrogen concentration in lattice and reversible trap sites, C_{OR} , is proportional to the steady-state permeation current density, i_p^∞ .^[34] C_{OR} was calculated

TABLE 1 The chemical composition of the API 5L X65 studied steel.

Element	C	Si	Mn	P	S	Cu	Cr
wt%	0.07	0.22	1.19	0.011	0.003	0.14	0.15
Element	Ni	Mo	V	Nb	Ti	N	Fe
wt%	0.15	0.12	0.02	0.019	0.001	0.01	Bal.

using Equation (1), where L denotes the thickness of the sample and F denotes the Faraday constant ($96,485 \text{ A s mol}^{-1}$).

$$C_{\text{OR}} = \frac{i_p^\infty L}{FD_{\text{eff}}}, \quad (1)$$

D_{eff} was determined by fitting the partial permeation transients to analytical solutions of Fick's second law to the build-up transient, Equation (2), and the decay transient, Equation (3).^[33] i_p denotes the permeation current density, i_p^0 denotes the permeation current density at the time of changing the applied potential, t denotes the time after changing the applied potential, and D denotes the hydrogen diffusion coefficient.

$$\frac{i_p - i_p^0}{i_p^\infty - i_p^0} = \frac{2L}{\sqrt{\pi Dt}} \sum_{n=0}^{\infty} \exp\left(-\frac{(2n+1)^2 L^2}{4Dt}\right), \quad (2)$$

$$\frac{i_p - i_p^\infty}{i_p^0 - i_p^\infty} = 1 - \frac{2L}{\sqrt{\pi Dt}} \sum_{n=0}^{\infty} \exp\left(-\frac{(2n+1)^2 L^2}{4Dt}\right). \quad (3)$$

According to Sieverts' law, the amount of hydrogen dissolved in steel is proportional to the square root of the hydrogen fugacity, f_{H_2} , where S denotes Sieverts' constant.^[35] At steady state, the lattice hydrogen concentration will scale as the reversibly trapped hydrogen concentration,^[36] hence, Sieverts' law can be expressed as shown in Equation (4). f_{H_2} is related to the hydrogen pressure, p_{H_2} , through the Abel–Noble equation of state, Equation (5), where b denotes a constant ($1.584 \times 10^{-5} \text{ m}^3 \text{ mol}^{-1}$), T denotes the temperature in K, and R denotes the gas constant ($8.314 \text{ J K}^{-1} \text{ mol}^{-1}$).^[37] The method to

determine the equivalent hydrogen fugacity, $f_{\text{H}_2}^{\text{eq}}$, is described in detail in a previous paper^[16] and is based on work reported by Atrons and colleagues.^[14,15,17] It is considered that charging conditions that produce the same C_{OR} in a steel are equivalent. In such matter, $f_{\text{H}_2}^{\text{eq}}$ was calculated by inserting C_{OR} determined from electrochemical charging into Equation (4) and solved for f_{H_2} . Then Equation (5) was solved iteratively using the Newton–Raphson method to determine the equivalent hydrogen pressure, $p_{\text{H}_2}^{\text{eq}}$, from $f_{\text{H}_2}^{\text{eq}}$.

$$C_{\text{OR}} = S \times \sqrt{f_{\text{H}_2}}, \quad (4)$$

$$f_{\text{H}_2} = p_{\text{H}_2} \exp\left(\frac{p_{\text{H}_2} b}{RT}\right). \quad (5)$$

3 | RESULTS AND DISCUSSION

The normalized partial permeation transients of the build-up and decay are presented in Figure 1a and 1b, respectively. The predicted solution of Fick's second law for lattice hydrogen diffusivity ($D_L = 7.27 \times 10^{-5} \text{ cm}^2 \text{ s}^{-1}$)^[38] is included in the figures, as well as the average of the best fits to Equations (2) and (3). In alloys such as X65 pipeline steels, a significant trap occupancy can cause the normalized permeation transient to be steeper than predicted by Fick's second law.^[39] The consequence can be a false interpretation of D_{eff} , which would appear to be changing with time.^[39] By using the method of partial permeation transients, the effect of changing trap occupancy on the transient is reduced,^[33] and the partial permeation transients can be fitted to the analytical solutions of

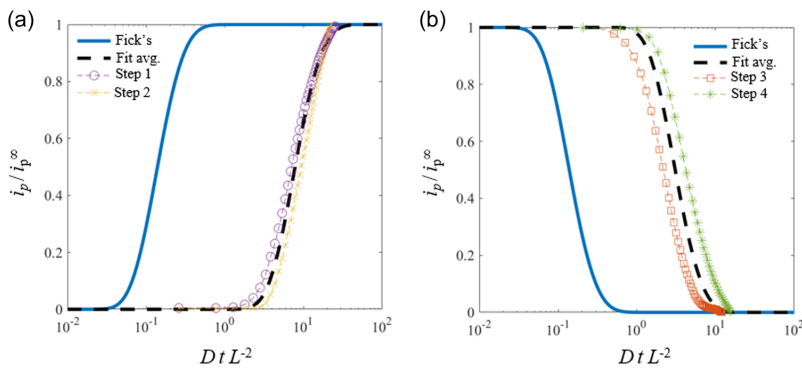


FIGURE 1 Normalized partial permeation transients obtained in a 3.5 wt% NaCl solution with a 2 g L^{-1} thiourea addition, including the prediction by Fick's second law for lattice diffusion and the average of the best fits. (a) Step 1: -1050 to $-1200 \text{ mV}_{\text{Ag}/\text{AgCl}}$, Step 2: -1200 to $-1350 \text{ mV}_{\text{Ag}/\text{AgCl}}$. (b) Step 3: -1350 to $-1200 \text{ mV}_{\text{Ag}/\text{AgCl}}$, Step 4: -1200 to $-1050 \text{ mV}_{\text{Ag}/\text{AgCl}}$. [Color figure can be viewed at wileyonlinelibrary.com]

Fick's second law. The average determined D_{eff} from the partial permeation transients is $2.3 \times 10^{-6} \text{ cm}^2 \text{ s}^{-1}$, which was used for the determination of C_{OR} .

Figure 2a shows two hydrogen permeation transients performed at 10, 50, and 100 bar. i_p^∞ increases with increasing applied p_{H_2} , manifesting that the hydrogen flux through the samples increases with increasing p_{H_2} . C_{OR} determined from gas charging at 10, 50, and 100 bar is 0.031, 0.066, and 0.095 wppm, respectively. Figure 2b shows the hydrogen permeation transients obtained in CP-simulated conditions. The corresponding C_{OR} obtained is 0.032 wppm. As shown in Figure 2c, C_{OR} obtained from gas charging is proportional to $f_{\text{H}_2}^{1/2}$, which is consistent with Sieverts' law (Equation 4). The calculated S is $0.0095 \text{ wppm bar}^{-1/2}$, which is slightly lower than determined in a previous study for a hot rolled and welded X65 pipeline steel.^[16] S is almost three times less than reported for a 3.5 NiCrMoV martensitic steel,^[18] however, it is two to three times higher than for a martensitic advanced high strength-steel^[17] and a dual phase steel.^[19] It is emphasized that the surface condition during gas permeation differs significantly from the inside of a pipeline in operation, for example, presence

of an oxide layer. However, pipelines are subjected to cyclic stresses caused by pressure fluctuations which can rupture an oxide layer and expose the bare steel surface. It is reported in the literature, that exposure to pressurized hydrogen gas reduces the fracture toughness and increases the fatigue crack growth rate of pipeline steels,^[4–6] indicating that hydrogen uptake occurs locally. The linearity between C_{OR} and $f_{\text{H}_2}^{1/2}$ and S being comparable to reported values suggests that the Pd-coated surface can resemble the hydrogen uptake of a bare steel surface after breakage of an oxide layer, however, this should be investigated further. In Figure 2c, the C_{OR} obtained at CP simulated conditions is superimposed onto the linear regression line determined for Sieverts' law, which corresponds to a $f_{\text{H}_2}^{\text{eq}}$ of 12.4 bar. Based on Equation (5), $p_{\text{H}_2}^{\text{eq}}$ is 12.3 bar, which is significantly lower than the desired hydrogen pressure of 200 bar.

Two methods to increase the hydrogen uptake are the addition of a hydrogen recombination poison,^[22,26] or to modify the cathodic charging parameters (i.e., apply a more negative potential or higher cathodic current density).^[15,25] Based on the previous study,^[16] a $p_{\text{H}_2}^{\text{eq}}$ of 196.4 bar was obtained at a current density of -50 mA cm^{-2}

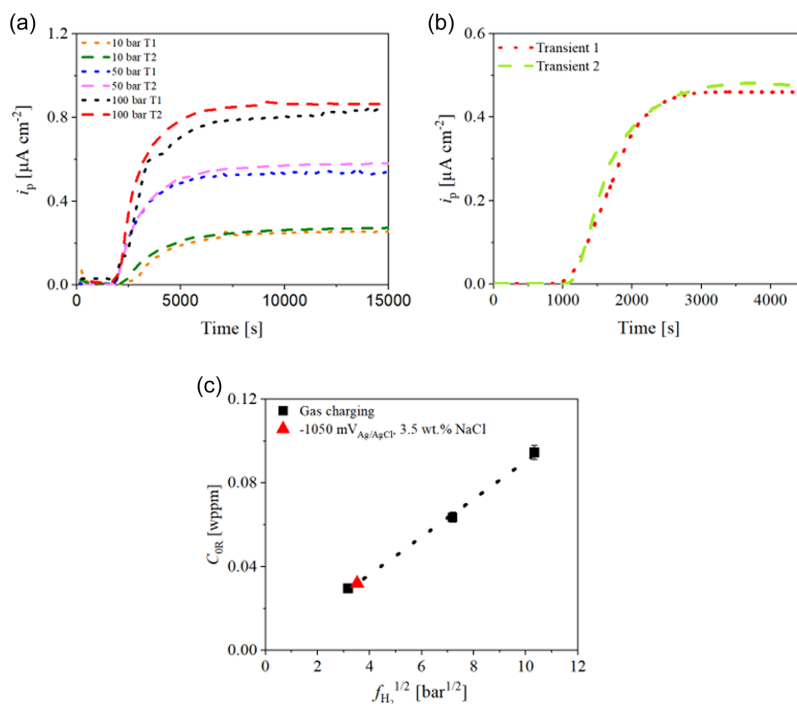


FIGURE 2 (a) Hydrogen permeation transients obtained at 10, 50, and 100 bar hydrogen gas charging pressures. (b) Hydrogen permeation transients were obtained at $-1050 \text{ mV}_{\text{Ag}/\text{AgCl}}$ in a 3.5 wt% NaCl solution. (c) Subsurface hydrogen concentration, C_{OR} , versus the square root of hydrogen gas fugacity, $f_{\text{H}_2}^{1/2}$, with C_{OR} obtained at $-1050 \text{ mV}_{\text{Ag}/\text{AgCl}}$ in a 3.5 wt% NaCl solution superimposed onto Sieverts' law regression line. [Color figure can be viewed at wileyonlinelibrary.com]

(corresponding to a potential of about $-2600 \text{ mV}_{\text{Ag}/\text{AgCl}}$). However, it can be difficult to maintain stable surface conditions at such high cathodic current density. Unsteady surface conditions can be a result of excessive hydrogen bubble formation or changes in local pH, leading to fluctuations in hydrogen flux or detachment of inclusions.^[26,27,40] In addition, the increasing influence of electrochemical recombination at higher cathodic current densities^[41] can reduce the effect of applied current density or potential on the $p_{\text{H}_2}^{\text{eq}}$. Consequently, it was decided to use a hydrogen recombination poison as the first measure to increase the hydrogen absorption, before changing the applied cathodic potential.

Thiourea is a hydrogen recombination poison often used to enhance the hydrogen uptake.^[21] Hydrogen permeation transients obtained at a cathodic potential of $-1050 \text{ mV}_{\text{Ag}/\text{AgCl}}$ in a 3.5 wt% NaCl solution with 0–3 g L^{-1} thiourea, are shown in Figure 3a. An addition of 0.5 g L^{-1} thiourea increases i_p^{∞} by approximately 2.5 times compared to the pure 3.5 wt% NaCl solution. Further, the additions of 1.0 and 2.0 g L^{-1} thiourea about triples i_p^{∞} . The $p_{\text{H}_2}^{\text{eq}}$ values as a function of thiourea concentration are presented in Figure 3b. It can be observed that $p_{\text{H}_2}^{\text{eq}}$ increases initially with an increasing thiourea concentration until 2 g L^{-1} , where a decrease in $p_{\text{H}_2}^{\text{eq}}$ started. The reduced hydrogen uptake at high hydrogen recombination poison concentration could be attributed to the formation of deposits acting as an inhibiting layer to hydrogen uptake.^[42] Because the addition of thiourea reached its limit contribution in $p_{\text{H}_2}^{\text{eq}}$ at 111.5 bar, it was necessary to apply more negative cathodic potential to obtain the desired $p_{\text{H}_2}^{\text{eq}}$ of 200 bar.

Hydrogen permeation transients obtained with different applied cathodic potentials in a 3.5 wt% NaCl solution

with 2 g L^{-1} thiourea concentration are presented in Figure 4a. The i_p^{∞} increases when more negative cathodic potentials are applied. Compared with that obtained at $-1050 \text{ mV}_{\text{Ag}/\text{AgCl}}$, i_p^{∞} increases by 1.17 times at $-1125 \text{ mV}_{\text{Ag}/\text{AgCl}}$, 1.35 times at $-1200 \text{ mV}_{\text{Ag}/\text{AgCl}}$, and 1.68 times at $-1275 \text{ mV}_{\text{Ag}/\text{AgCl}}$. Table 2 lists the determined C_{OR} , $f_{\text{H}_2}^{\text{eq}}$, and $p_{\text{H}_2}^{\text{eq}}$. At -1200 and $-1275 \text{ mV}_{\text{Ag}/\text{AgCl}}$ the $p_{\text{H}_2}^{\text{eq}}$ obtained are 191.4 and 237.4 bar, respectively. Hence, the desired $p_{\text{H}_2}^{\text{eq}}$ of 200 bar should be obtained between these two potentials. To determine the potential at which a 200 bar $p_{\text{H}_2}^{\text{eq}}$ would be obtained, $f_{\text{H}_2}^{\text{eq}}$ is plotted on a logarithmic scale as a function of applied potential, as illustrated in Figure 4b. By using Equation (5), it is calculated that a 200 bar p_{H_2} corresponds to a f_{H_2} of 227.2 bar. The relationship between $f_{\text{H}_2}^{\text{eq}}$ and applied potential from Figure 4b was solved for 227.2 bar, and the determined corresponding potential was approximately $-1225 \text{ mV}_{\text{Ag}/\text{AgCl}}$. Following the above deduction, a permeation transient was performed at a potential of $-1225 \text{ mV}_{\text{Ag}/\text{AgCl}}$ in 3.5 wt% NaCl solution with 2 g L^{-1} thiourea concentration, and the results are included in Table 2. The corresponding C_{OR} is 0.137 wppm and the $p_{\text{H}_2}^{\text{eq}}$ is 201.9 bar. Thus, electrochemical charging at a potential $-1225 \text{ mV}_{\text{Ag}/\text{AgCl}}$ in 3.5 wt% NaCl solution with 2 g L^{-1} thiourea concentration can represent approximately the same C_{OR} as a $p_{\text{H}_2}^{\text{eq}}$ of 200 bar. The determined equivalence in terms of hydrogen uptake was obtained with a Pd coating during gas permeation. However, in real service conditions, the equivalence can be affected by relevant environmental parameters (e.g., the presence of surface oxides, temperature, and local stress conditions), which should be carefully considered in the design of HE susceptibility investigations. In addition, the transferability of the determined equivalent hydrogen pressure to mechanical testing needs to be validated.

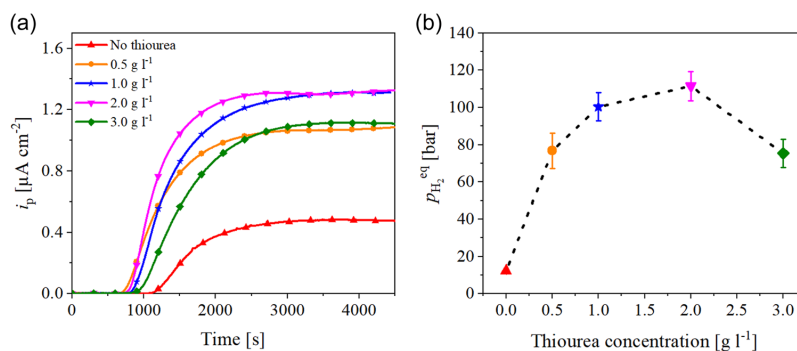


FIGURE 3 (a) Hydrogen permeation transients obtained at $-1050 \text{ mV}_{\text{Ag}/\text{AgCl}}$ in a 3.5 wt% NaCl solution with different thiourea concentrations. (b) Equivalent hydrogen pressure, $p_{\text{H}_2}^{\text{eq}}$, versus the thiourea concentration. [Color figure can be viewed at wileyonlinelibrary.com]

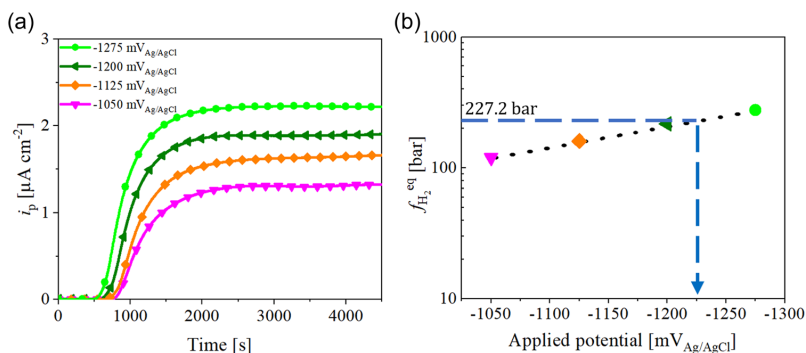


FIGURE 4 (a) Hydrogen permeation transients performed at different cathodic potentials in a 3.5 wt% NaCl solution with 2 g L^{-1} thiourea. (b) Equivalent hydrogen fugacity, $f_{\text{H}_2}^{\text{eq}}$, versus the applied potential. [Color figure can be viewed at wileyonlinelibrary.com]

TABLE 2 C_{OR} , $f_{\text{H}_2}^{\text{eq}}$, and $p_{\text{H}_2}^{\text{eq}}$ obtained by charging at different cathodic potentials in a 3.5 wt% NaCl solution with 2 g L^{-1} thiourea.

Potential (mV _{Ag/AgCl})	C_{OR} (wppm)	$f_{\text{H}_2}^{\text{eq}}$ (bar)	$p_{\text{H}_2}^{\text{eq}}$ (bar)
-1050	0.099 ± 0.004	119.8 ± 9.0	111.5 ± 7.8
-1125	0.115 ± 0.002	160.0 ± 4.3	145.7 ± 3.6
-1200	0.133 ± 0.001	216.3 ± 2.7	191.4 ± 2.2
-1225	0.137 ± 0.001	229.7 ± 1.5	201.9 ± 1.2
-1275	0.151 ± 0.002	276.3 ± 7.2	237.4 ± 5.4

4 | CONCLUSIONS

This study established an equivalence between electrochemical and gaseous hydrogen charging by the addition of a hydrogen recombination poison in combination with different charging potentials. The results show that the subsurface hydrogen concentration was proportional to the square root of the hydrogen fugacity, in agreement with Sieverts' law, which formed the basis for determining the equivalent hydrogen pressure. Electrochemical charging at the condition simulating cathodic protection at $-1050 \text{ mV}_{\text{Ag/AgCl}}$ was equivalent to a hydrogen pressure of 12.3 bar at room temperature. Higher equivalent pressures were achieved by adding thiourea to the 3.5 wt% NaCl solution, and by applying more negative cathodic potentials. The equivalent pressure as a function of thiourea concentration went through a maximum at 2 g L^{-1} . The desired equivalent pressure of about 200 bar, which is a potential hydrogen pressure during hydrogen gas transportation using pipeline steel, was obtained in a 3.5 wt% NaCl solution with 2 g L^{-1} thiourea and an applied potential of $-1225 \text{ mV}_{\text{Ag/AgCl}}$ at room temperature. The equivalent hydrogen pressure

was deduced using a Pd coating during gas permeation, and further evaluation must be conducted to elucidate the effect of surface conditions and transferability to mechanical testing.

ACKNOWLEDGMENTS

The authors acknowledge the financial support by the Research Council of Norway and the industry company partners through the HyLINE project (294739).

CONFLICT OF INTEREST STATEMENT

The authors declare no conflict of interest.

DATA AVAILABILITY STATEMENT

The data that support the findings of this study are available from the corresponding author upon reasonable request.

ORCID

Erik Koren  <http://orcid.org/0009-0009-3790-9756>

Roy Johnsen  <http://orcid.org/0000-0002-5449-7396>

REFERENCES

- [1] Z. Abidin, A. Zafaranloo, A. Rafiee, W. Mérida, W. Lipiński, K. R. Khalilpour, *Renew. Sustain. Energy Rev.* **2020**, *120*, 109620.
- [2] N. E. Nanninga, Y. S. Levy, E. S. Drexler, R. T. Condon, A. E. Stevenson, A. J. Slifka, *Corros. Sci.* **2012**, *59*, 1.
- [3] J. Yamabe, T. Awane, S. Matsuoka, *Int. J. Hydrogen Energy* **2015**, *40*, 11075.
- [4] L. Briottet, I. Moro, P. Lemoine, *Int. J. Hydrogen Energy* **2012**, *37*, 17616.
- [5] T. An, H. Peng, P. Bai, S. Zheng, X. Wen, L. Zhang, *Int. J. Hydrogen Energy* **2017**, *42*, 15669.
- [6] E. S. Drexler, A. J. Slifka, R. L. Amaro, N. Barbosa, D. S. Lauria, L. E. Hayden, D. G. Stalheim, *Fatigue Fracture Eng. Mater. Struct.* **2014**, *37*, 517.

- [7] S. Cerniauskas, A. J. Chavez Junco, T. Grube, M. Robinius, D. Stolten, *Int. J. Hydrogen Energy* **2020**, *45*, 12095C12107.
- [8] L. Briottet, R. Batisse, G. de Dinechin, P. Langlois, L. Thiers, *Int. J. Hydrogen Energy* **2012**, *37*, 9423.
- [9] S. Lynch, *Corros. Rev.* **2012**, *30*, 105.
- [10] G. B. Rawls, T. Adams, N. L. Newhouse in *Gaseous hydrogen embrittlement of materials in energy technologies*, Vol. 1 (Eds: R. P. Gangloff, B. P. Somerday), Woodhead Publishing Series in Metals and Surface Engineering, London **2012**, p. 3.
- [11] A. Turnbull, in *Gaseous hydrogen embrittlement of materials in energy technologies*, Vol. 1 (Eds: R. P. Gangloff, B. P. Somerday), Woodhead Publishing Series in Metals and Surface Engineering, London **2012**, p. 89.
- [12] P. Zhang, M. Laleh, A. E. Hughes, R. K. W. Marceau, T. Hilditch, M. Y. Tan, *Int. J. Hydrogen Energy* **2023**, *48*, 16501.
- [13] A. J. Kumnick, H. H. Johnson, *Metall. Trans. A* **1975**, *6*, 1087.
- [14] A. Atrens, D. Mezzanotte, N. F. Fiore, M. A. Genshaw, *Corros. Sci.* **1980**, *20*, 673.
- [15] Q. Liu, A. D. Atrens, Z. Shi, K. Verbeken, A. Atrens, *Corros. Sci.* **2014**, *87*, 239.
- [16] E. Koren, C. M. H. Hagen, D. Wang, X. Lu, R. Johnsen, J. Yamabe, *Corros. Sci.* **2023**, *215*, 111025.
- [17] J. Venezuela, E. Gray, Q. Liu, Q. Zhou, C. Tapia-Bastidas, M. Zhang, A. Atrens, *Corros. Sci.* **2017**, *127*, 45.
- [18] J. Venezuela, C. Tapia-Bastidas, Q. Zhou, T. Depover, K. Verbeken, E. Gray, Q. Liu, Q. Liu, M. Zhang, A. Atrens, *Corros. Sci.* **2018**, *132*, 90.
- [19] Q. Liu, E. Gray, J. Venezuela, Q. Zhou, C. Tapia-Bastidas, M. Zhang, A. Atrens, *Adv. Eng. Mater.* **2018**, *20*, 1700469.
- [20] J. L. Crolet, G. Maisonnette, Corrosion, NACE International, Houston **2000**.
- [21] T. Depover, D. Pérez Escobar, E. Wallaert, Z. Zermout, K. Verbeken, *Int. J. Hydrogen Energy* **2014**, *39*, 4647.
- [22] E. Akiyama, S. Li, *Corros. Rev.* **2016**, *34*, 103.
- [23] E. Protopopoff, P. Marcus, in *Corrosion mechanisms in theory and practice* (Ed: P. Marcus), CRC Press Taylor and Francis Group, Boca Raton **2011**, p. 105.
- [24] B. J. Berkowitz, J. J. Burton, C. R. Helms, R. S. Polizzotti, *Scripta Metall.* **1976**, *10*, 871.
- [25] L. Zhang, W. Cao, K. Lu, Z. Wang, Y. Xing, Y. Du, M. Lu, *Int. J. Hydrogen Energy* **2017**, *42*, 3389.
- [26] Y. J. Jeong, S. J. Kim, *Int. J. Hydrogen Energy* **2021**, *46*, 7615.
- [27] J. Flis, *Electrochim. Acta* **1999**, *44*, 3989.
- [28] H. Husby, M. Iannuzzi, R. Johnsen, M. Kappes, A. Barnoush, *Int. J. Hydrogen Energy* **2018**, *43*, 3845.
- [29] P. Bruzzoni, *Int. J. Hydrogen Energy* **2000**, *25*, 61.
- [30] P. Castaño Rivera, V. P. Ramunni, P. Bruzzoni, *Corros. Sci.* **2012**, *54*, 106.
- [31] P. Manolatos, M. Jerome, J. Galland, *Electrochim. Acta* **1995**, *40*, 867.
- [32] M. A. V. Devanathan, Z. Stachurski, *Proc. R. Soc. Lond. Ser. A. Math. Phys. Sci.* **1962**, *270*, 90.
- [33] T. Zakroczymski, *Electrochim. Acta* **2006**, *51*, 2261.
- [34] ISO 17081:2014, *Method of measurement of hydrogen permeation and determination of hydrogen uptake and transport in metals by an electrochemical technique*, International Organization for Standardization **2014**.
- [35] K. K. Gupta, *Chemical Metallurgy: Principles and Practice*, Wiley-VCH, Weinheim **2003**.
- [36] A. Turnbull, *Int. J. Hydrogen Energy* **2015**, *40*, 16961.
- [37] C. San Marchi, B. Somerday, S. Robinson, *Int. J. Hydrogen Energy* **2007**, *32*, 100.
- [38] K. Kiuchi, R. B. McLellan, *Acta Metall.* **1983**, *31*, 961.
- [39] A. Turnbull, *Mater. Sci. Forum* **1995**, *192-194*, 63.
- [40] S. M. Charca, O. N. C. Uwakweh, V. S. Agarwala, *Metall. Mater. Trans. A* **2007**, *38*, 2389.
- [41] J. O. Bockris, J. McBreen, L. Nanis, *J. Electrochem. Soc.* **1965**, *112*, 1025.
- [42] E. Lunarska, Z. Szklarska-Smialowska, M. Smialowski, *Mater. Corros.* **1975**, *26*, 324.

How to cite this article: E. Koren, C. M. H. Hagen, D. Wang, X. Lu, R. Johnsen, *Mater. Corros.* **2023**, *1*.
<https://doi.org/10.1002/maco.202313931>

Paper 3

Hydrogen diffusivity in X65 pipeline steel: Desorption and permeation studies

E. Koren, J. Yamabe, X. Lu, C. M. H. Hagen, D. Wang, R. Johnsen

Under review in the International Journal of Hydrogen Energy

Hydrogen diffusivity in X65 pipeline steel: Desorption and permeation studies

Erik Koren^a, Junichiro Yamabe^b, Xu Lu^a, Catalina M. H. Hagen^c, Dong Wang^a, Roy Johnsen^a

^aDepartment of Mechanical and Industrial Engineering, NTNU, 7491 Trondheim, Norway

^bDepartment of Mechanical Engineering, Fukuoka University, 8-19-1 Nanakuma, Jonan-ku, Fukuoka, 814-0180, Japan

^cSINTEF, Richard Birkelandsvei 2B, 7465 Trondheim, Norway

Abstract

Hydrogen diffusivity can play a crucial role in hydrogen-assisted degradation of steels. Herein, we investigate the hydrogen diffusion behavior in two X65 pipeline steels using desorption and permeation techniques. Gas charged samples were used for desorption experiments, while permeation tests were conducted using electrochemical charging. The Vintage steel, having a banded ferrite-pearlite microstructure, exhibits a significant influence of strong traps. A modified solution of Fick's 2nd law is proposed to account for the strong traps. At room temperature, the effective diffusivity in the Modern steel, which has homogenous ferrite-bainite microstructure, has a scatter factor of three, whereas for the Vintage steel, the factor is 17. The difference is explained by considering a concentration-dependent effective diffusivity and a tortuous diffusion path. Comparable values of the highest measured effective diffusivity at room temperature were obtained for the Modern and Vintage steels: 2.70×10^{-6} and 3.34×10^{-6} cm²/s, respectively.

Keywords: Hydrogen diffusion, Hydrogen permeation, Hydrogen desorption, Hydrogen trapping, Pipeline steels

1. Introduction

Hydrogen diffusion and trapping in metals have been a topic of interest ever since hydrogen

was first reported to reduce the toughness and ductility of iron and steel, termed as hydrogen embrittlement [1,2]. In 1874, Johnson [1] reported a lower diffusivity in steel compared with pure iron and described a faster recovery from hydrogen embrittlement in iron than steel. Diffusion of hydrogen from the bulk to local areas ahead of crack tips is today regarded as an important process in hydrogen-assisted cracking [2,3]. Lattice diffusion proceeds by hydrogen atoms jumping between interstitial sites, which for bcc iron are tetrahedral sites at ambient temperatures [4]. In other sites, such as grain boundaries, vacancies, dislocations, and carbides, the hydrogen atoms can have a longer residence time than those in the interstitial lattice sites [3]. Such sites slow down the transport of hydrogen and are typically termed as traps. The binding energy of a trap will vary for different microstructural sites and affect the hydrogen's residence time in the trap. The higher the trap binding energy, the lower the probability of hydrogen escaping the trap and the longer the residence time [5]. Pressouyre and Bernstein [6] defined traps where hydrogen has a short residence time at the temperature of interest, as reversible, and traps where the probability of releasing hydrogen is negligible, as irreversible. At room temperature, a binding energy above 50-60 kJ/mol has been regarded as irreversible [7]; However, the probability of hydrogen escaping a trap increases with increasing temperature [5]. Hydrogen is commonly divided into diffusible and non-diffusible, where the former represents the hydrogen in lattice and reversible trap sites [8]. The role of traps in hydrogen-assisted cracking has been debated, questioning whether they can serve as protective barriers or potentially act as hydrogen sources when subjected to stress [9,10]. Understanding the diffusivity and trapping behavior of hydrogen in steels can be important for understanding the embrittlement phenomena, developing predictive models for hydrogen embrittlement, and designing materials for hydrogen applications.

The most common method to determine the hydrogen diffusion coefficient in metals has been the double electrochemical cell for hydrogen permeation, which was first described by Devanathan and Stachurski [11]. The set-up includes two compartments: a charging compartment and a detection compartment, which are separated by the sample. The hydrogen flux through the sample can be used to calculate the hydrogen diffusivity using Fick's laws of diffusion. The hydrogen permeation technique has later been developed to compare different hydrogen sources and to evaluate hydrogen trapping properties, e.g., using gaseous hydrogen charging [12–14], and performing stepwise partial permeation transients [15]. Due to the existence of various influencing parameters, the permeation technique is frequently discussed [16–20], e.g., the effect of hydrogen trapping on the permeation transients. When traps are

present, the hydrogen transport is retarded, and the determined hydrogen diffusivity is an effective value [5]. If the fraction of occupied traps becomes significant during the transient, the rate of hydrogen transport will change during the transient, and determining an effective diffusivity does not have a theoretical basis in Fick's laws [5,20]. Performing partial permeation transients, where the charging condition is changed in steps, can improve the adherence to Fick's 2nd law of diffusion [15]. This method offers advantages like minimal disturbance of trap occupancy and limiting surface effects [15,21,22].

Hydrogen desorption-based methods are common alternatives to determining the hydrogen diffusivity in metals [18,23–28]. Typically, the hydrogen desorbing from a charged sample is detected, e.g., using a gas chromatography-mass spectrometer (GC-MS) or a thermal conductivity detector. Hydrogen diffusivity can be measured by placing a charged sample in a furnace, holding a constant temperature, and continuously measuring the desorbing hydrogen [18,23,24]. Another possibility is to measure the hydrogen concentration of several samples as a function of dwell time after charging [23] or the hydrogen charging time [26,28]. In all cases, the hydrogen concentration evolution versus time is fitted to a solution of Fick's 2nd law of diffusion. Permeation and desorption techniques to determine the hydrogen diffusivity have been used in combination in a few studies [18,23,26,29]. Zafra et al. [18,23] reported good agreement between the effective diffusivity determined by a desorption method and partial permeation, with the former having a better reproducibility. Lu et al. [26] reported a three-times difference in the determined effective diffusivity between desorption and permeation methods, and speculated that the difference was caused by trapping or surface effects. Simoni et al. [29] combined numerical analysis with desorption and permeation experiments. They recommended to use several experimental techniques and charging conditions for determining quantitative parameters in steels with complex microstructures because changing fraction of occupied traps makes it challenging to determine the effective diffusivity and trapping parameters.

Pipeline steels have been recognized as an essential part of the hydrogen transport infrastructure necessary to develop a hydrogen economy [30]. Recently, there have been interest in whether existing natural gas pipelines can be used to transport H₂ gas or if new steel pipelines should be developed [30–33]. The microstructure of the pipeline steel will influence the diffusivity and trapping of hydrogen, which can affect the susceptibility to hydrogen embrittlement [34–36]. In a microstructure with no texture, hydrogen diffusion can occur in all directions and is not orientation-dependent [37]; However, banded ferrite-pearlite

microstructures are common in hot rolled and welded lower-grade pipeline steels [38]. Because of lower hydrogen diffusivity in pearlite, the pearlite bands can lead to a tortuous diffusion path [37,39]. In such case, the orientation of the diffusion path relative to the banded direction can affect the determined effective hydrogen diffusivity [37,39]. Hydrogen-assisted fatigue crack growth rate has been reported to be orientation-dependent in a ferritic-pearlitic X65 pipeline steel with a banded structure, partially attributed to limited diffusion through pearlite bands [36]. A pipeline steel can potentially have many trapping sites, e.g., dislocations, grain boundaries, and particle-matrix interfaces [7,40–42]. Dunne et al. [43] investigated the capacity of X70 steels for strong hydrogen trapping with varying microstructures. The results revealed that a banded ferritic-pearlitic microstructure had a higher concentration of strongly trapped hydrogen compared with equiaxed ferritic-pearlitic and ferritic-bainitic microstructures [43]. The hydrogen diffusivity in pipeline steels has been reported in several studies in the literature. The reported hydrogen diffusion coefficient for X65 pipeline steels at room temperature varies over two orders of magnitude, from 1.5×10^{-7} to 2×10^{-5} cm²/s [17,22,35,44–46]. A similar scatter is observed for other grades, such as X70 [47–51]. Such scatter can be caused by difference in microstructure, technique, and charging method, which can affect the determined effective diffusivity. Following the recommendation by Simoni et al. [29], different techniques and charging methods will be conducted to evaluate the hydrogen diffusivity in X65 pipeline steel.

The objective of this study is to investigate the hydrogen diffusivity in two X65 pipeline steels utilizing permeation- and desorption-based techniques. Both complete and partial permeation transients were performed by electrochemical charging. In comparison, hydrogen charging for the desorption-based methods was conducted by exposure to pressurized H₂ gas. The effects of microstructure and concentration-dependent effective diffusivity were discussed.

2. Materials and methods

2.1 Materials and sample preparation

In this study, two types of X65 pipeline steels were investigated. One modern steel was selected to represent steel for potential new infrastructure for H₂ gas transport. In addition, steel from an existing natural gas pipeline was selected to investigate the feasibility of repurposing the infrastructure. The chemical compositions are listed in Table 1. The steel, denoted as Modern, is a seamless quenched and tempered pipeline steel with a wall thickness of 15.4 mm. The steel, denoted as Vintage, is a hot-rolled and longitudinal welded pipeline

steel with a wall thickness of 26 mm. Microstructural characterizations of the two studied steels were reported in [13,52,53]. The microstructure of the Modern steel consists of ferrite and bainite, which are homogeneously distributed. The phase volume fraction of ferrite is 84%, and the average grain size is approximately 7 μm . The Vintage steel has a banded microstructure consisting of alternating layers of ferrite and pearlite. Some granular bainite is present within the pearlite bands. The phase volume fraction of ferrite is approximately 85% and the average grain size is approximately 4 μm . Only slight microstructural differences were observed through the pipe thickness; Hence, average values through the thickness are given. In this study, only the base material was investigated.

Samples employed for hydrogen permeation tests were disks of 30 mm diameter and 1.9 mm thickness. The samples were machined from a position close to the inner side of the pipe wall, parallel to the longitudinal direction. The samples were ground with SiC paper to a finish of #P1000 grade. The disks used for permeation tests were coated with Pd by electroplating on the detection side to facilitate the oxidation of hydrogen [54]. The electroplating procedure followed the method described by Husby et al. [55] based on Bruzzoni et al. [56] and Castaño Rivera et al. [57]. A cross-section of the permeation samples was studied using optical microscopy. The cross-sectional area was ground and polished until 1 μm diamond paste and etched in a 3% nital (3% HNO_3 and 97% ethanol) solution.

Cylindrical samples were employed for hydrogen desorption tests. The radius, r , of the Vintage steel was 9.5 mm. Due to the lower wall thickness of the Modern steel, these samples had an r of 7.5 mm. The thickness, L , of the samples used for desorption measurements was 19 mm. The relatively large samples for hydrogen desorption tests were used to ensure volume-controlled diffusion [24]. The samples were ground with SiC paper to a finish of #P600 grade and were coated with a Pd layer by ion sputtering.

Modern	Element	C	Si	Mn	P	S	Cu	Cr
	wt%	0.07	0.22	1.19	0.011	0.003	0.14	0.15
	Element	Ni	Mo	V	Nb	Ti	N	Fe
	wt%	0.15	0.12	0.02	0.019	0.001	0.01	Bal.
Vintage	Element	C	Si	Mn	P	S	Cu	Cr
	wt. %	0.1	<0.6	<1.6	<0.025	<0.015	<0.25	<0.25
	Element	Ni	Mo	V	Nb	Ti	N	Fe
	wt. %	<0.25	<0.05	<0.1	<0.05	<0.02	<0.01	Bal.

Table 1 Chemical composition of the two X65 steels.

2.2 Hydrogen desorption methods

The samples used for hydrogen desorption tests were charged in a high-pressure hydrogen autoclave at a pressure of 1000 bar at a temperature of 85 °C. The samples were charged for 200 hours to reach the saturation level of hydrogen. After charging, the samples were stored in liquid nitrogen to avoid unwanted hydrogen desorption. To measure hydrogen concentration using GC-MS, the samples were removed from the liquid nitrogen, rinsed in distilled water and ethanol, and dried with an air blower. The total dwell time, including the transfer from the charging autoclave to liquid nitrogen and from liquid nitrogen to the GC-MS, was less than 15 minutes.

Two desorption methods were used to determine the hydrogen diffusivity. The method denoted as in-situ desorption, involved inserting the charged sample into a furnace connected to the GC-MS. The temperature in the furnace was kept constant while continuously measuring the hydrogen desorbing from the sample. The temperature in the GC-MS furnace was kept at 25, 50, and 85 °C. The temperatures were selected based on a previous study on hydrogen diffusivity in low-alloy steels [24]. When the desorption rate was negligible, the furnace temperature was ramped up at a heating rate of 100 °C/h to desorb the residual hydrogen concentration in the sample. The method, denoted as ex-situ desorption, involves keeping charged samples at a constant temperature for different holding times. The samples were kept either at the laboratory room temperature of 24 °C or in a refrigerator at -2 °C. The samples

were subsequently inserted into the GC-MS furnace and the residual hydrogen concentration was measured by heating at a rate of 100 °C/h. For both methods, Eq. (1), which is a modified solution to Fick's 2nd law of diffusion, was used to fit the residual diffusible hydrogen concentration, C_{HD} , versus the holding time, t_R , to determine the effective diffusion coefficient, D_{eff} [24,27,58]. A is a fitted constant to account for hydrogen diffused out during the dwell time between charging and desorption analysis. β_m is the root of the zero-order Bessel function.

$$C_{HD} = \frac{32}{\pi^2} \cdot A \cdot \left\{ \sum_{n=0}^{\infty} \frac{\exp \left[-\frac{(2n+1)^2 \pi^2 D_{eff} t_R}{L^2} \right]}{(2n+1)^2} \right\} \cdot \left\{ \sum_{m=1}^{\infty} \frac{\exp \left[-\frac{D_{eff} \beta_m^2 t_R}{r^2} \right]}{\beta_m^2} \right\} \quad (1)$$

2.3 Hydrogen permeation methods

Hydrogen permeation tests were performed in a double electrochemical cell consisting of a charging chamber (cathodic side) and a detection chamber (anodic side), after the principles described by Devanathan and Stachurski [11] and standardized in [59,60]. A description of the permeation cell was presented in a previous paper [13]. The electrolyte was a 0.1 M NaOH solution in the detection chamber, and a Hg/Hg₂SO₄ (sat. K₂SO₄) electrode was used as a reference. Platinum foil was used as the counter electrode in both chambers. A 3.5 wt.% NaCl solution and an Ag/AgCl (sat. KCl) reference electrode was used in the charging chamber. Initially, a potential of -83 mV vs. Hg/Hg₂SO₄ (+315 mV vs. SCE) was applied in the detection chamber, and the electrolyte was continuously purged with N₂ gas. At the same time, the empty charging chamber was purged with N₂ gas to avoid oxidation of the sample surface. When the permeation current density, i_p , obtained a stable value below 0.1 μA/cm², the electrolyte was added to the charging chamber, a -1 mA/cm² current density was applied, and the N₂ gas purging stopped. Both chambers were double-walled such that water from a water bath could be circulated through the outside of the cell to control the temperature. Four temperatures were used: 7, 21, 50, and 75 °C. The temperatures were chosen to facilitate comparison with the desorption measurements; However, the lower temperature was limited by issues with condensation on the sample's charging side during stabilization of the permeation current density, while the upper temperature was limited by unstable surface conditions.

D_{eff} was determined by two methods based on Fick's law of diffusion: The time-lag method and the breakthrough time method [59–61]. The time-lag, t_{lag} , is the time it takes to reach 63%

of the steady-state permeation current density, i_p^∞ . D_{eff} determined by the time lag method is denoted as, $D_{\text{eff}}(t_{\text{lag}})$, and is calculated using Eq. (2). The breakthrough time, t_b , is defined as the intercept of an extrapolated line from the linear part of the permeation curve and the x-axis. The D_{eff} determined by the breakthrough time method is denoted as, $D_{\text{eff}}(t_b)$, and is calculated using Eq. (3).

$$D_{\text{eff}}(t_{\text{lag}}) = \frac{L^2}{6 t_{\text{lag}}} \quad (2)$$

$$D_{\text{eff}}(t_b) = \frac{L^2}{19.8 t_b} \quad (3)$$

Subsequent to the complete permeation transients, stepwise partial permeation transients were performed. The charging current density, i_c , was changed in steps while continuously measuring the permeation current density. One experiment was performed by stepping i_c between 0.5 and 1 mA/cm² to a minimum of two build-up and two decay transients were obtained. The temperatures were 7, 21, and 50 °C. In addition, one experiment was performed at 21 °C where i_c was changed in three steps: -0.5 to -1 mA/cm², -1 to -1.5 mA/cm², and -1.5 to -2 mA/cm². D_{eff} was determined by fitting the build-up and decay transients to Eqs. (4) and (5), respectively. t denotes the time after changing i_c and i_p^0 denotes i_p when i_c is changed.

$$\frac{i_p - i_p^0}{i_p^\infty - i_p^0} = \frac{2L}{\sqrt{\pi D_{\text{eff}} t}} \sum_{n=0}^{\infty} \exp\left(-\frac{(2n+1)^2 L^2}{4D_{\text{eff}} t}\right) \quad (4)$$

$$\frac{i_p - i_p^\infty}{i_p^0 - i_p^\infty} = 1 - \frac{2L}{\sqrt{\pi D_{\text{eff}} t}} \sum_{n=0}^{\infty} \exp\left(-\frac{(2n+1)^2 L^2}{4D_{\text{eff}} t}\right) \quad (5)$$

3. Results

3.1 Microstructure

Fig. 1 (a) and (b) show optical micrographs of the Modern and Vintage steels, respectively. The cross-section shows the through-thickness area of the pipelines, close to the inner side of the pipe wall. The Modern steel consists of a homogenous distribution of ferrite- and bainite grains, as reported in [52,53]. It was reported in [13,52] that Vintage steel consists of ferrite,

pearlite, and a small fraction of granular bainite. Fig. 1(b) shows that the pearlite grains are elongated parallel to the rolling direction.

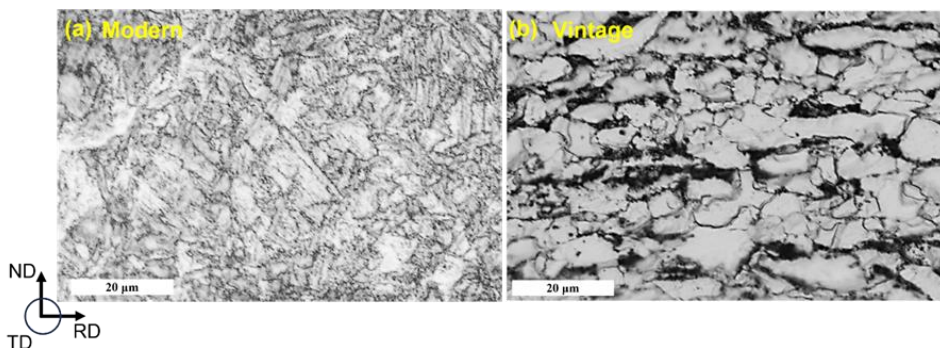


Fig. 1. Optical micrographs of (a) the Modern steel and (b) the Vintage steel. The bright regions are ferrite, while the dark areas are pearlite and bainite. ND - Normal direction, RD – Rolling direction, and TD – Transverse direction.

3.2 Desorption methods

3.2.1 Ex-situ hydrogen desorption

Fig. 2(a) and (b) show hydrogen desorption curves for the Modern steel after ex-situ desorption at holding temperatures of 24 °C and –2 °C, respectively. The desorption curves generally exhibit a normalized shape, and the area under the curves reduces with increasing t_R . To determine D_{eff} , only diffusible hydrogen is of interest. In desorption spectra, the diffusible hydrogen is regarded as the hydrogen desorbing up to the temperature where the desorption curve is independent of t_R ; in this case, 275 °C was sufficient to achieve this. Hydrogen desorbing at higher temperatures is considered as strongly trapped. At 24 °C holding temperature, the hydrogen desorption flux is approximately zero after t_R above 40 hours. For desorption curves after holding at –2 °C, a t_R of 72 h was insufficient to reach a hydrogen desorption flux of zero. At around 225-250 °C, there appears to be a minor shoulder peak, which is independent of t_R . The shoulder peak was most prominent at –2 °C, which could be because of the longer residence time in traps at lower temperatures.

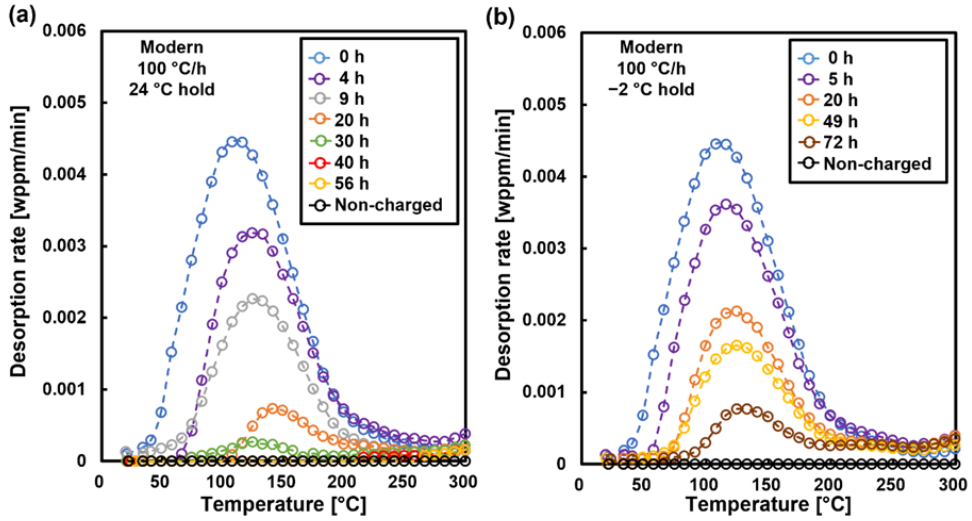


Fig. 2. Hydrogen desorption curve for the Modern steel charged at 85 °C in H₂ gas at 1000 bar pressure for 200 h and kept in a thermostatic chamber at (a) 24 °C holding temperature (b) -2 °C holding temperature.

C_{HD} in the Modern steel as a function of t_R at 24 °C and -2 °C, is shown in Fig. 3. C_{HD} was defined as the hydrogen content desorbed below 275 °C, which was the temperature where the desorption curves were independent of t_R . It is observed that the decrease in C_{HD} is faster at 24 °C than at -2 °C, indicating higher diffusivity at the higher holding temperature. The solution to Fick's 2nd law of diffusion (Eq. (1)) was fitted to the data using the least square method, giving a good fit to the data at both holding temperatures. At 24 °C, D_{eff} is 1.24×10^{-6} cm²/s with a coefficient of determination, R^2 , of 0.995. At -2 °C, D_{eff} is 3.37×10^{-7} cm²/s with a R^2 value of 0.993.

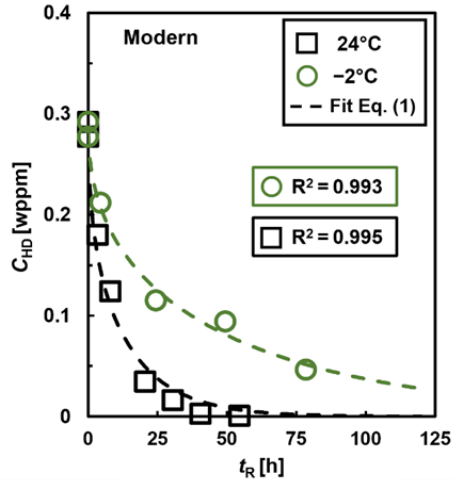


Fig. 3. Residual diffusible hydrogen concentration, C_{HD} , in the Modern steel as a function of holding time, t_R , in a thermostatic chamber fitted to a solution of Fick's 2nd law of diffusion.

In comparison, Fig. 4(a) and (b) show hydrogen desorption curves for the Vintage steel after ex-situ desorption at holding temperatures of 24 °C and -2 °C, respectively. The shape of the desorption curves appears to be asymmetric, stretching towards higher temperature. The area under the curve reduces with increasing t_R . In contrast to the Modern steel, the hydrogen desorption rate never reaches zero within the t_R utilized. A small peak is observed in the non-charged sample, starting at about 200 °C, indicating some strongly trapped hydrogen. The desorption rate is independent of the t_R from approximately 275 °C.

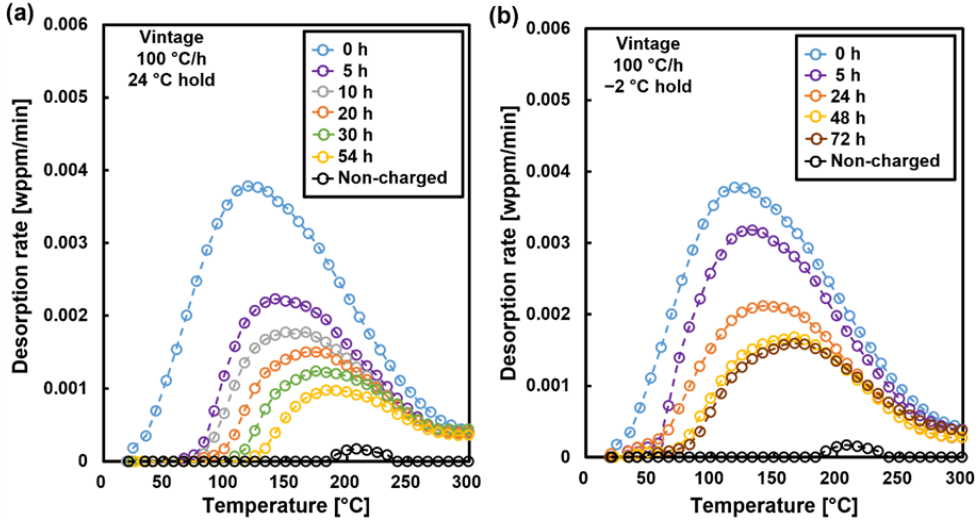


Fig. 4. Hydrogen desorption curve for Vintage steel samples charged at 85 °C in H₂ gas at 1000 bar pressure for 200 h and kept in a thermostatic chamber at (a) 24 °C holding temperature (b) -2 °C holding temperature.

Fig. 5 shows C_{HD} in the Vintage steel as a function of t_R at 24 °C and -2 °C. From Fig. 4, it is challenging to separate diffusible from non-diffusible hydrogen because the peak of the non-charged sample overlaps with a region where the area under the curve is reducing with t_R . C_{HD} was considered as the hydrogen desorbing up to the temperature where the desorption curves were independent of t_R , which was 275 °C. The hydrogen concentration of the non-charged hydrogen was subtracted from C_{HD} . As was observed in the Modern steel, C_{HD} in Vintage steel samples decreases with t_R , and the reduction is faster at 24 °C than at -2 °C, manifesting that the hydrogen diffusivity increases with increasing temperature. After extended t_R , the residual hydrogen concentration is close to being independent of the t_R and forms a lower limiting level. C_{HD} as a function of t_R was fitted to the solution of Fick's 2nd law (Eq. (1)). At 24 °C, D_{eff} is 7.87×10^{-7} cm²/s and the R² value is 0.920. At -2 °C, D_{eff} is 2.18×10^{-7} cm²/s and the R² value is 0.965. Hence, the lower limiting level where the change in C_{HD} versus t_R was negligible caused poorer fits to Fick's 2nd law compared with the fits obtained to the results of the Modern steel.

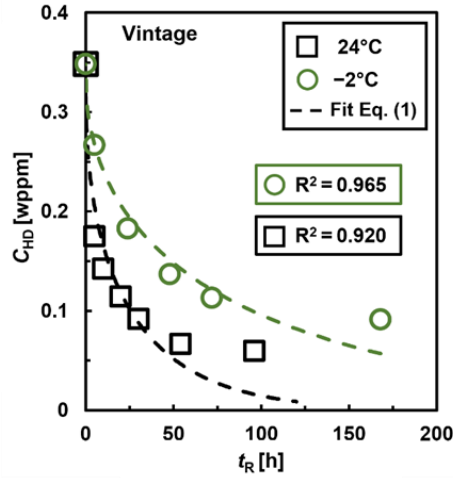


Fig. 5. Residual diffusible hydrogen concentration, C_{HD} , in the Vintage steel as a function of holding time, t_R , in a thermostatic chamber fitted to a solution of Fick's 2nd law of diffusion.

3.2.2 In-situ hydrogen desorption

Fig. 6(a) and (b) show C_{HD} as a function of t_R measured using in-situ desorption at 25, 50, and 85 °C for the Modern and Vintage steel, respectively. It is observed that the C_{HD} decreases faster with increasing temperature, indicating that the hydrogen diffusivity increases with increasing holding temperature. The D_{eff} and R^2 values determined by fitting to the solution of Fick's 2nd law (Eq. (1)) are listed in Table 2. The R^2 values for the Modern steel are all above 0.976, demonstrating a good fit between the data and the solution to Fick's 2nd law. The D_{eff} determined at 25 °C is 1.50×10^{-6} cm²/s, which is in excellent agreement with that determined by ex-situ desorption at 24 °C, 1.24×10^{-6} cm²/s. For the Vintage steel, the curves reach a lower limiting level where C_{HD} is almost independent of the t_R , similar to what was observed in Fig. 5 by ex-situ desorption. The value of the C_{HD} lower limiting level reduces with increasing temperature. As observed for ex-situ desorption, the R^2 values are relatively not as high as for the Modern steel, which was attributed to the limiting level of C_{HD} versus t_R . D_{eff} determined at 25 °C is 8.78×10^{-7} cm²/s, which is comparable to the value determined by the ex-situ desorption at 24 °C, 7.87×10^{-7} cm²/s.

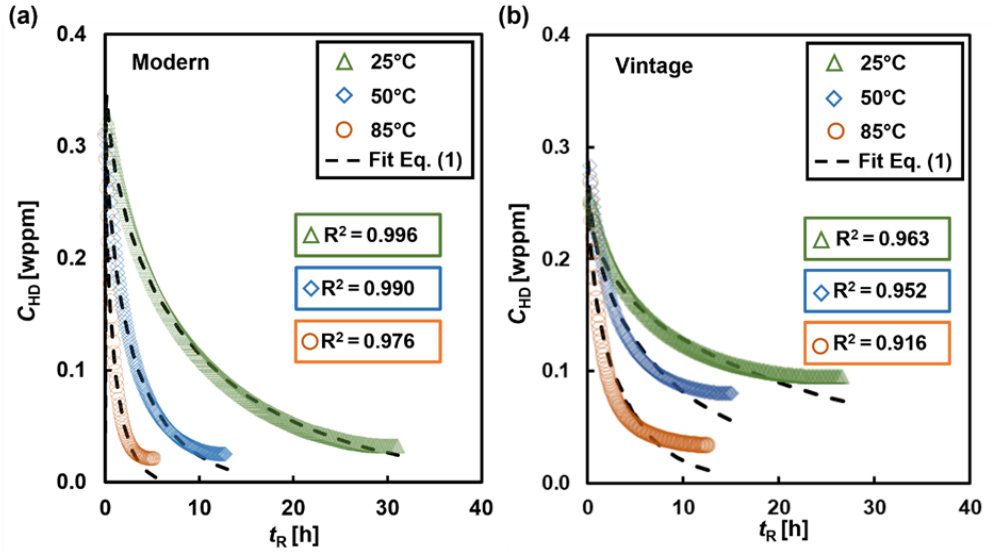


Fig. 6. Residual diffusible hydrogen concentration, C_{HD} , in (a) the Modern steel (b) the Vintage steel as a function of holding time, t_R , determined by in-situ desorption at 25, 50, and 85 °C fitted to a solution of Fick's 2nd law.

Steel	Temperature [°C]	D_{eff} [cm ² /s]	R^2
Modern	25	1.50×10^{-6}	0.996
	50	4.87×10^{-6}	0.990
	85	1.56×10^{-5}	0.976
Vintage	25	8.78×10^{-7}	0.963
	50	2.22×10^{-6}	0.952
	85	6.43×10^{-6}	0.916

Table 2 D_{eff} and R^2 values determined by in-situ desorption for the Modern and Vintage steel.

3.3 Electrochemical hydrogen permeation

3.3.1 Complete permeation transients

Fig. 7 shows three subsequent complete hydrogen permeation transients for (a) the Modern steel and (b) the Vintage steel, obtained at an applied current density of -1 mA/cm^2 and temperatures of 7, 21, 50, and 75 °C. For both steels, i_p^∞ increases with increasing temperature, manifesting that the hydrogen flux through the samples increases with increasing temperature. It can be observed that t_b decreases with increasing temperature, indicating that the hydrogen diffusivity increases with increasing temperature. At 75 °C, i_p fluctuated or did not stabilize, which is likely related to unsteady surface conditions at higher temperatures. Only two successful transients were obtained at 75 °C.

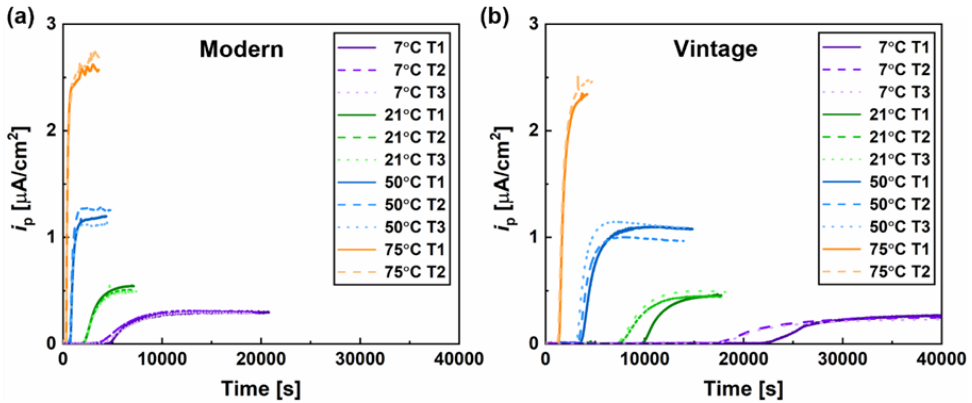


Fig. 7. Hydrogen permeation transients of (a) the Modern steel and (b) the Vintage steel obtained at 21, 50, and 75 °C during after charging in 3.5 wt% NaCl solution at an applied current density of -1 mA/cm^2 . T1-Transient 1, T2-Transient 2, T3-Transient 3.

In Fig. 7, it can be observed that t_b of the transients differs in some conditions, which is most prominent for the Vintage steel and at lower temperatures. Such difference has been attributed to strong traps that are filled during the first transient and remain filled until the start of the subsequent transients, hence only affecting the hydrogen transport during the first transient [6]. In this case, hydrogen having a residence time longer than approximately 24 hours, which is the approximate time between the transients, is considered as strongly trapped. Fig. 8 shows a close-up of Fig. 7 focusing on the time when the first hydrogen is detected for (a)-(d) the Modern steel and (e)-(h) the Vintage steel. For the Modern steel, a difference in t_b between the transients can be observed at 7 °C, while no significant difference in t_b is observed at

higher temperatures, 21, 50, and 75 °C. For the Vintage steel, a distinct difference in t_b is observed between the first transient and the two subsequent transients at 7 and 21 °C. A difference can also be observed at higher temperatures, but the difference in t_b decreases with increasing temperature.

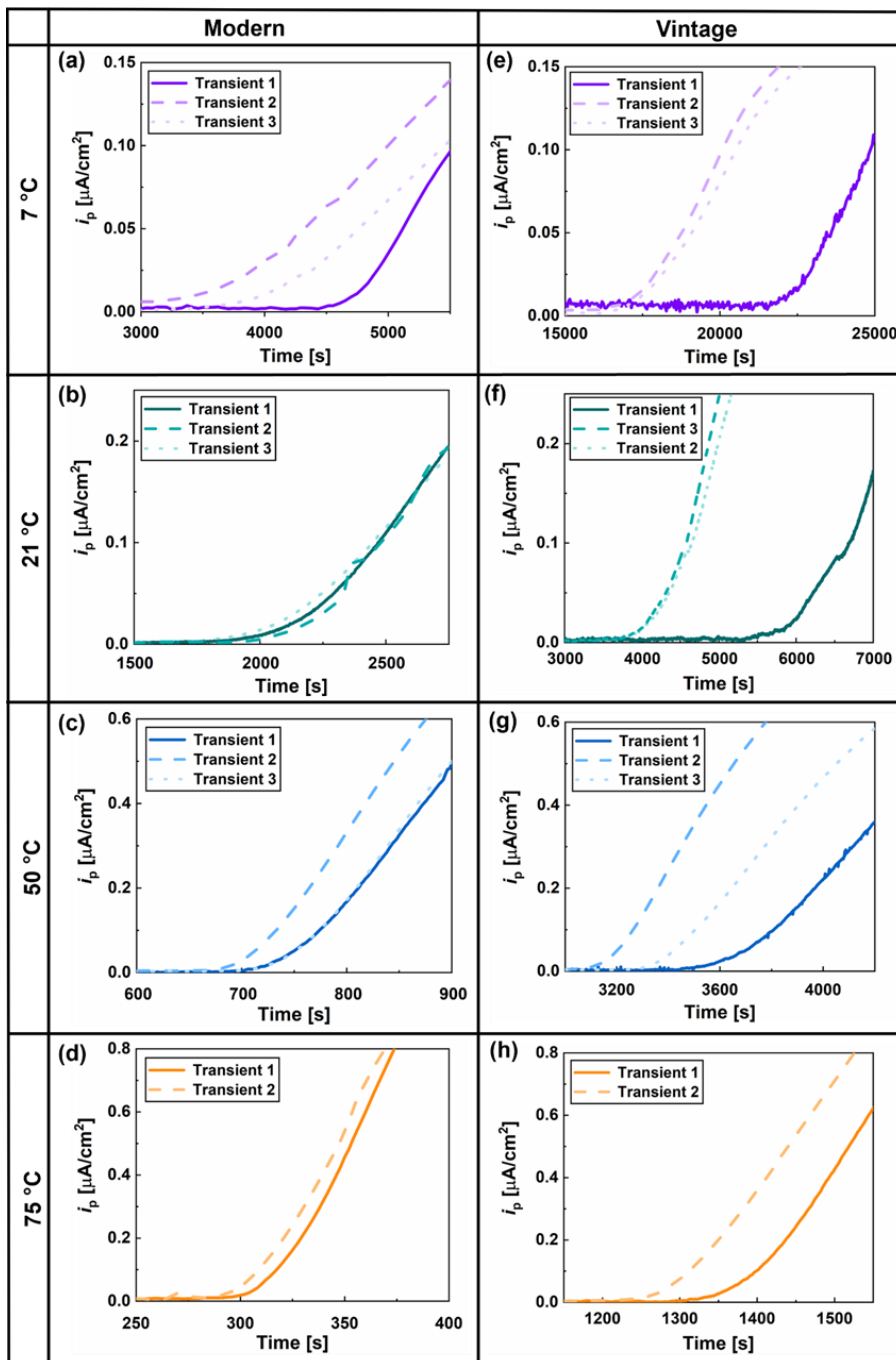


Fig. 8. Close-up of the breakthrough time during complete electrochemical permeation transients at 7, 21, 50, and 75 °C of (a)-(d) the Modern steel and (e)-(h) the Vintage steel.

Fig. 9 shows the ratio of t_b of the first transient to the t_b of the subsequent transients, denoted as the t_b -ratio. A t_b -ratio of one would imply that strong trapping does not occur. Because there was some deviation in t_b also between the 2nd and 3rd transient at some temperatures, the t_b -ratio is calculated using the average t_b of Transient 2 and 3. At 7 °C, the t_b -ratio of the Modern steel of 1.22 indicates some strong hydrogen trapping. The t_b -ratio of the Modern steel is approximately one at the higher temperatures: 21, 50, and 75 °C. For the Vintage steel, the t_b -ratios were approximately 1.30 at 7 °C and 21 °C. When the temperature increased above 21 °C, the t_b -ratio decreased to 1.14 at 50 °C and 1.07 at 75 °C. The reduction in t_b -ratio with increasing temperature manifests that the residence time in traps decreases with increasing temperature.

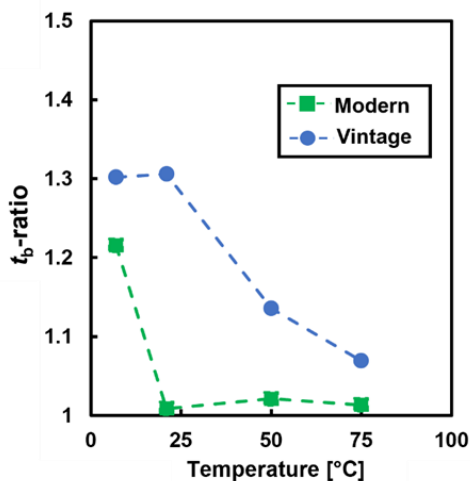


Fig. 9. Ratio of the breakthrough time, t_b , of Transient 1 to the average of t_b of Transient 2 and 3, denoted as t_b -ratio, as a function of temperature.

Because of the effect of strong traps on the first transient, only the results obtained from the subsequent transients were used to calculate D_{eff} . The obtained values for D_{eff} of the two steels determined by the t_b method ($D_{\text{eff}}(t_b)$) and the t_{lag} method ($D_{\text{eff}}(t_{\text{lag}})$) at 7, 25, 50, and 75 °C are listed in Table 3. For both steels, the diffusivity determined by the t_{lag} method is higher than that determined by the t_b method for all the conditions. In the literature, such difference has been attributed to the filling of traps causing a higher D_{eff} in a later stage of the transients when the occupancy of traps is higher [29,62]. For the Modern steel at 21 °C, $D_{\text{eff}}(t_b)$ is 8.56×10^{-7} cm²/s and $D_{\text{eff}}(t_{\text{lag}})$ is 1.83×10^{-6} cm²/s, which are comparable to the diffusivity determined by the desorption methods (1.50×10^{-6} cm²/s at 24 °C and 1.24×10^{-6} cm²/s at 25

°C). For the Vintage steel at 21 °C, $D_{\text{eff}}(t_b)$ and $D_{\text{eff}}(t_{\text{lag}})$ are 1.95×10^{-7} and 5.24×10^{-7} cm²/s, respectively. Both diffusivities are lower than that determined by the desorption methods, 7.87×10^{-7} cm²/s at 24 °C and 8.78×10^{-7} cm²/s at 25 °C.

Steel	Temperature [°C]	$D_{\text{eff}}(t_b)$ [cm ² /s]	$D_{\text{eff}}(t_{\text{lag}})$ [cm ² /s]
Modern	7	4.62×10^{-7}	8.96×10^{-7}
	21	8.56×10^{-7}	1.83×10^{-6}
	50	2.57×10^{-6}	6.21×10^{-6}
	75	6.04×10^{-6}	1.32×10^{-5}
Vintage	7	1.05×10^{-7}	2.78×10^{-7}
	21	1.95×10^{-7}	5.24×10^{-7}
	50	5.05×10^{-7}	1.30×10^{-6}
	75	1.25×10^{-6}	3.34×10^{-6}

Table 3 D_{eff} determined by electrochemical hydrogen permeation. The results are average values determined from Transients 2 and 3.

3.3.2 Partial permeation transients

The stepwise partial permeation build-up and decay transients fitted to the analytical solutions of Fick's 2nd law (Eqs. (4) and (5)) obtained by stepwise changing the applied current density between 0.5 and 1 mA/cm² are presented in Fig. 10(a) and (b) for the Modern and Vintage steel, respectively. The fits are good for both steels at all temperatures. The effective diffusivity determined by partial permeation transients, $D_{\text{eff}}(\text{PT})$, are listed in Table 4. For the Modern steel the, $D_{\text{eff}}(\text{PT})$ are comparable with those determined by the desorption methods and the complete permeation transients, although slightly higher values were obtained. For the Vintage steel, $D_{\text{eff}}(\text{PT})$ were higher than the diffusivities determined by the complete

permeation transients; however, they were lower than those determined by the desorption methods. Compared to the Modern steel, the Vintage steel presents lower D_{eff} using permeation methods.

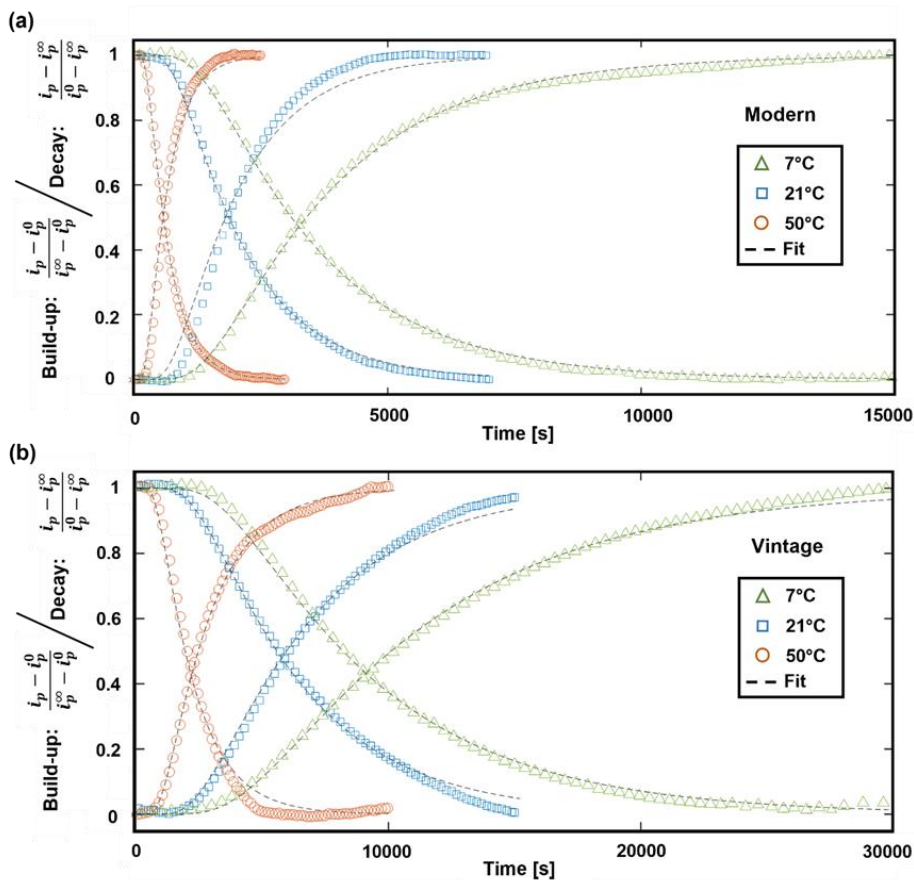


Fig. 10 Partial permeation build-up and decay transients fitted to the solutions of Fick’s 2nd law (Eqs. (4) and (5)) for (a) the Modern steel and (b) the Vintage steel. The charging current density was stepped between -0.5 and -1 mA/cm^2 in 3.5 wt% NaCl at 7, 21, and 50 °C.

Steel	Temperature [°C]	$D_{\text{eff}}(\text{PT})$ [cm^2/s]	R^2
Modern	7	1.37×10^{-6}	0.994
	21	2.70×10^{-6}	0.993
	50	9.07×10^{-6}	0.984
Vintage	7	5.61×10^{-7}	0.990
	21	7.85×10^{-7}	0.983
	50	2.35×10^{-6}	0.980

Table 4 D_{eff} determined by partial permeation transients at 7, 21, and 50 °C. The results are average values of a minimum of two build-up and two decay transients.

Fig. 11(a) and (b) show the stepwise partial permeation build-up transients of the Modern and Vintage steel, respectively, which were performed in three steps of i_c from $-0.5 \text{ mA}/\text{cm}^2$ to $-2 \text{ mA}/\text{cm}^2$, and the fits to the analytical solution of Fick's 2nd law (Eq. (4)). D_{eff} and R^2 values are listed in Table 5. For the Modern steel, there is no significant change in the $D_{\text{eff}}(\text{PT})$ with increasing i_c . D_{eff} of the Vintage steel increases with each step of the charging current density. From the step between -0.5 and $-1.0 \text{ mA}/\text{cm}^2$ the $D_{\text{eff}}(\text{PT})$ is $7.85 \times 10^{-7} \text{ cm}^2/\text{s}$, while the step between -1.5 and $-2.0 \text{ mA}/\text{cm}^2$ yields a $D_{\text{eff}}(\text{PT})$ of $1.28 \times 10^{-6} \text{ cm}^2/\text{s}$.

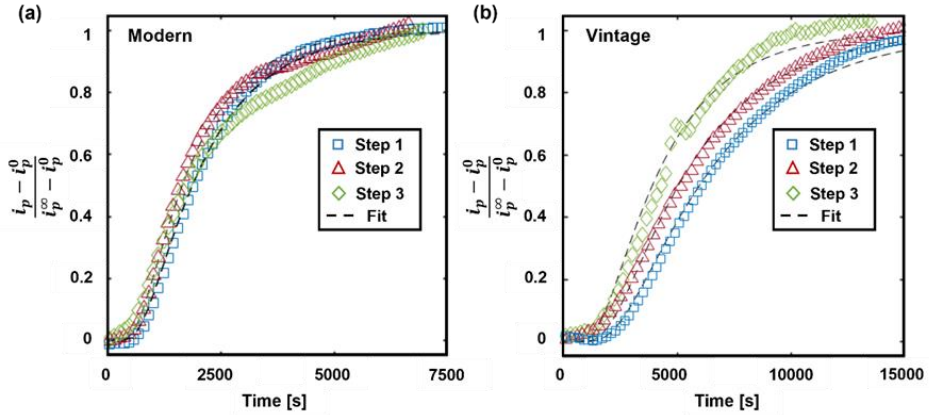


Fig. 11. Partial permeation build-up transient for (a) the Modern steel and (b) the Vintage steel performed in 3.5 wt% NaCl at 21 °C fitted to the solution of Fick's 2nd law (Eq.(4)).

Step 1: -0.5 to -1 mA/cm², Step 2: -1 to -1.5 mA/cm², Step 3: -1.5 to -2 mA/cm².

Steel	i_c -step [mA/cm ²]	$D_{\text{eff}}(\text{PT})$ [cm ² /s]	R ²
Modern	0.5-1	2.70×10^{-6}	0.993
	1-1.5	3.02×10^{-6}	0.995
	1.5-2	2.66×10^{-6}	0.977
Vintage	0.5-1	7.85×10^{-7}	0.983
	1-1.5	9.94×10^{-7}	0.994
	1.5-2	1.28×10^{-6}	0.988

Table 5 D_{eff} determined by partial permeation transients at 21 °C.

4. Discussion

The hydrogen diffusivity in two X65 pipeline steels was investigated by hydrogen desorption and permeation methods. The Modern steel has a microstructure consisting of homogeneously distributed grains of ferrite and bainite, while the Vintage steel has a microstructure mainly

consisting of banded ferrite-pearlite layers. Hydrogen desorption from samples charged in high-pressure H₂ gas was measured by GC-MS. Both in-situ and ex-situ hydrogen desorption measurements were conducted. Electrochemical hydrogen permeation was performed with both complete and partial transients. The results will be discussed in detail in the following sections.

4.1 Strong hydrogen trapping

Hydrogen trapping affects the transport of hydrogen in steels, which can complicate the determination of hydrogen diffusivities. In particular, traps where hydrogen atoms have long residence time will cause deviation from Fickian diffusion [6,62,63]. In complete permeation transients, a difference in t_b between the first and subsequent transients indicates strong trapping. This is attributed to the filling of traps that remain filled until subsequent transients; hence, the trap will only affect the hydrogen transport during the first transient [6]. Such traps have been reported to have a binding energy above 50-60 kJ/mol [7]. Figs. 7-9 showed that such an effect was less prominent in the Modern steel than in the Vintage steel; However, a significant t_b -ratio was observed at the lowest temperature, 7 °C. Because the probability of hydrogen escaping a trap increases with increasing temperature [5], the residence time in traps and the t_b -ratio reduced with increased temperature. For the Modern steel, it was not observed any hydrogen desorption from the non-charged sample in Fig. 2. For the Vintage steel, on the other hand, a desorption peak for the non-charged Vintage sample was observed in Fig. 4, confirming the presence of strong traps. Thus, both permeation and desorption methods indicate less strong trapping in the Modern steel than in the Vintage steel. This is in agreement with Dunne et al. [43], who reported that ferritic-pearlitic microstructures have a higher capability of strong trapping than ferritic-bainitic microstructures. According to Karimi et al. [64], strong trapping occurs at ferrite-pearlite and/or pearlite-pearlite interfaces, corresponding to binding energies of 64-69 kJ/mol. In a study by Myhre et al. [52], who investigated hydrogen embrittlement susceptibility by slow strain rate tensile testing of four steels, including the Modern and the Vintage steels, it was reported that the Modern steel was less susceptible to hydrogen embrittlement than the Vintage steel. The result was partially attributed to a higher cleanliness and lower number of inclusions in the Modern steel than in the Vintage steel. Inclusions are reported to be strong traps [65,66], e.g. MnS inclusions 73.8 kJ/mol trap binding energy [65], which could contribute the strong trapping effect observed in the Vintage steel. Inclusions can increase hydrogen embrittlement susceptibility by acting as crack initiation sites and stress concentrators due to high local hydrogen concentrations

[52,66].

In the permeation method, hydrogen in strong traps can be accounted for by performing subsequent complete transients or partial transients [6,15]. In the desorption tests for the Vintage steel (Fig. 4), the broad asymmetric desorption peaks overlapped with the peak of the non-charged sample, indicating that the peaks consist of hydrogen from several traps, rendering it challenging to separate diffusible and non-diffusible hydrogen. As a result, lower limiting levels were observed in Fig. 5 and Fig. 6(b), where C_{HD} was independent of t_R . These lower limiting levels lead to a poorer fit to the solution of Fick's 2nd law for the Vintage steel, as compared to the fits for the Modern steel (Fig. 3 and 6(a)). To account for the strongly trapped hydrogen during the determination of D_{eff} by the desorption methods, a constant term denoted as C_{strong} was added to Eq. (1), as shown in Eq. (6):

$$C_{HD} = \frac{32}{\pi^2} \cdot A \cdot \left\{ \sum_{n=0}^{\infty} \frac{\exp\left[-\frac{(2n+1)^2 \pi^2 D t_R}{L^2}\right]}{(2n+1)^2} \right\} \cdot \left\{ \sum_{m=1}^{\infty} \frac{\exp\left[-\frac{D \beta_m t_R}{r^2}\right]}{\beta_m^2} \right\} + C_{strong} \quad (6)$$

Fig. 12 show C_{HD} versus t_R of the Vintage steel fitted by Eqs. (1) and (6) for (a) ex-situ desorption and (b) in-situ desorption. For both methods, the modified equation gives an improved fit at all temperatures. Table 6 lists the comparison of D_{eff} and R^2 values for the Vintage steel, determined by fitting C_{HD} versus t_R to Eq. (1) and Eq. (6). D_{eff} at 24 °C determined by Eq. (1) and Eq. (6) is 7.76×10^{-7} and 2.21×10^{-6} cm²/s, respectively. At -2 °C, D_{eff} determined by Eq. (1) and Eq. (6) is 2.18×10^{-7} and 6.98×10^{-7} cm²/s, respectively. For both methods, the R^2 values increased using Eq. (6). Hence, modifying the solution of Fick's 2nd law of diffusion to account for the stronger trapping was essential to estimate the hydrogen diffusivity. After modification, D_{eff} for the Vintage steels determined by the desorption methods are slightly higher but comparable to those of the Modern steel.

Temperature [°C] / Method	Eq. (1): D_{eff} [cm ² /s]	Eq. (1): R^2	Eq. (6): D_{eff} [cm ² /s]	Eq. (6): R^2
-2 / Ex-situ	2.18×10^{-7}	0.965	6.98×10^{-7}	0.998
24 / Ex-situ	7.76×10^{-7}	0.920	2.21×10^{-6}	0.992
25 / In-situ	8.78×10^{-7}	0.963	3.34×10^{-6}	0.985
50 / In-situ	2.22×10^{-6}	0.952	8.04×10^{-6}	0.989
85 / In-situ	6.43×10^{-6}	0.916	1.74×10^{-5}	0.991

Table 6 D_{eff} and R^2 values obtained for the Vintage steel by fitting to Eq. (1) and Eq. (6).

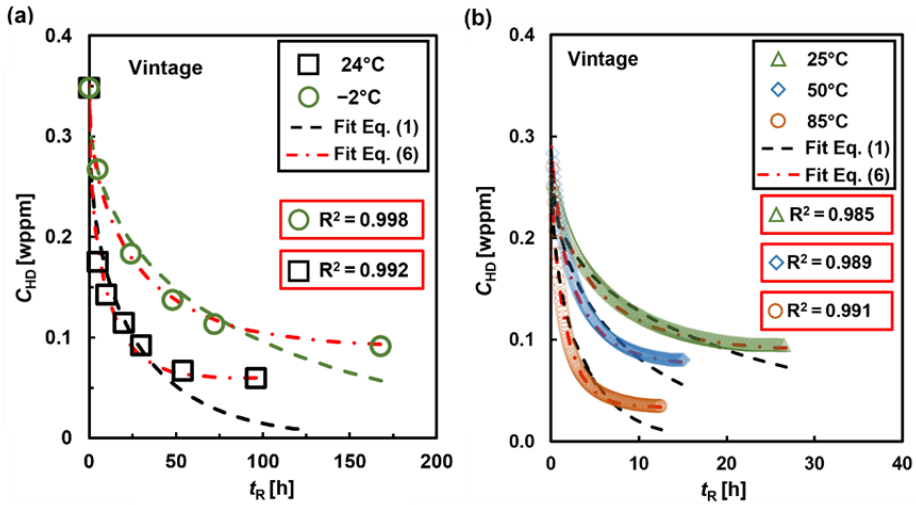


Fig. 12. Residual diffusible hydrogen concentration, C_{HD} , versus holding time, t_{R} , for the Vintage steel, for (a) ex-situ desorption and (b) in-situ desorption. Fitted solution to the analytical solution of Fick's 2nd law with and without modification to account for strong trapping.

4.2 Arrhenius relationship

Fig. 13(a) and (b) show the Arrhenius plots of all the methods used for the Modern and Vintage steels, respectively. The Arrhenius relationship is given in Eq. (7), where D_0 denotes the pre-

exponential factor, E_d denotes the activation energy of diffusion, and R_g denotes the gas constant (8.314 J/K mol). The Arrhenius relationship deduced by Kiuchi and McLellan [4] for well-annealed iron, $7.23 \times 10^{-4} \exp\left(\frac{-5690}{RT}\right)$ cm²/s, is regularly quoted as the lattice diffusion, D_L , and is included in the figure. Because there was good agreement between the two desorption methods, the results were combined to obtain one Arrhenius relationship.

$$D = D_0 \exp\left(-\frac{E_d}{R_g T}\right) \quad (7)$$

Table 7 lists the Arrhenius parameters of the Modern steel and Vintage steel, respectively. E_d determined from the different methods were in good agreement for both steels. As expected, trapping effects cause a higher E_d for the investigated X65 steels. For the Modern steel, the E_d values are between 30.5 to 36.0 kJ/mol, with the average value between all the methods being 32.9 kJ/mol. For the Vintage steel, the E_d values are between 25.1 and 29.0 kJ/mol, with an average value of 27.5 kJ/mol. For the Modern and Vintage steel there is about a 13 and 18 times difference in D_0 values, respectively. Hence, the more consistent D_0 values produced the lower scatter between methods observed in Fig. 13 for the Modern steel compared with the Vintage steel. The determined Arrhenius relationships are comparable to reported values, $6.5 \times 10^{-3} \exp\left(\frac{-25500}{RT}\right)$ cm²/s for X65 pipeline steel [67] and $0.39 \exp\left(\frac{-32200}{RT}\right)$ cm²/s, which is calculated from data given in [57]. At room temperature, there is a large scatter in reported diffusivity values for X65 pipeline steels, 1.5×10^{-7} to 2×10^{-5} cm²/s [17,22,35,44–46]. Reasons for the large scatter in diffusivities could be different investigation methods utilized, different charging conditions, and different microstructures. In this work, the lowest and highest measured D_{eff} of the Modern steel at room temperature are 8.56×10^{-7} and 2.70×10^{-6} cm²/s, about a three-time difference. For the Vintage steel, the difference between the lowest (1.95×10^{-7} cm²/s) and highest (3.34×10^{-6} cm²/s) measured D_{eff} at room temperature is 17 times. Hence, the highest measured D_{eff} at room temperature in the two steels are comparable, while the scatter factor is highest in the Vintage steel. The results indicate that the significance of the method utilized can vary from steel to steel, and possible reasons will be discussed in the following paragraphs.

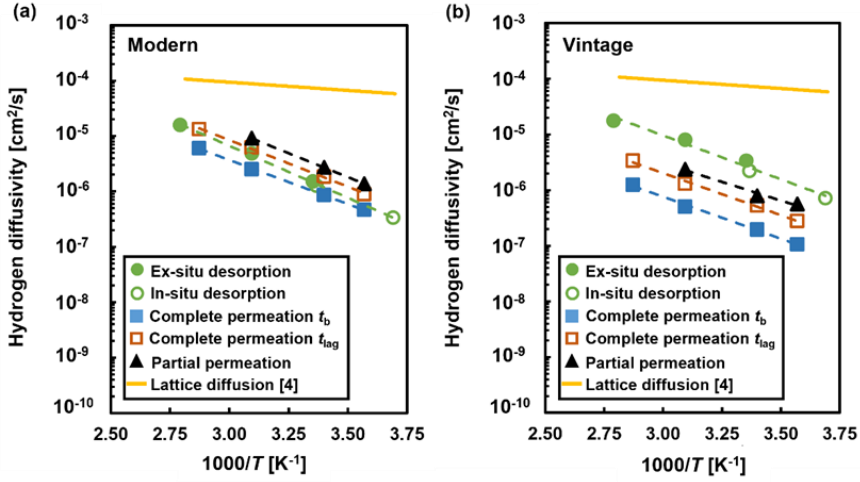


Fig. 13. Arrhenius plot including all the methods used to determine the hydrogen diffusivity for (a) the Modern steel and (b) the Vintage steel.

Steel	Parameter	Desorption	Partial permeation	Breakthrough time	Time lag
Modern	D_0 [cm ² /s]	2.92	1.99	0.220	0.936
	E_d [kJ/mol]	36.0	33.0	30.5	32.2
Vintage	D_0 [cm ² /s]	0.506	0.031	0.027	0.068
	E_d [kJ/mol]	27.1	25.1	29.0	28.9

Table 7 Arrhenius parameters of the Modern and Vintage steels.

4.3 Tortuosity

The tortuosity of the diffusion path may account for the lower scatter in D_{eff} for the Modern steel compared with the Vintage steel. The Modern steel has a microstructure consisting of equiaxed ferrite- and bainite grains, while the Vintage steel mainly consists of a banded structure of ferrite- and pearlite grains. In equiaxed microstructures, the hydrogen diffusivity can occur in all directions and is not orientation dependent [37]; Hence, a significant tortuosity effect would not be expected in the Modern steel. In banded ferrite-pearlite microstructures, the lower diffusivity in pearlite grains can cause preferential hydrogen diffusion through ferrite

grains [37,39], which could occur in the Vintage steel. A tortuous diffusion path can lead to an orientation dependency of the effective diffusivity [37,39]. For the Vintage steel, an effect of tortuosity should be most significant in the permeation tests because of the thin disk samples where one-dimensional diffusion was assumed. Fig. 14 illustrates a possible diffusion path in the Vintage steel in the through-thickness direction (normal direction), which is perpendicular to the elongated pearlite grains. In desorption tests, on the other hand, large samples and a three-dimensional solution to Fick's 2nd law were used. Thus, a tortuosity effect could explain why D_{eff} in the Modern steel was higher than in the Vintage steel in permeation tests, in contrast to desorption tests, where D_{eff} in the Modern steel was lower than in the Vintage steel. The hydrogen assisted fatigue crack growth rate have been reported to be affected by ferrite-pearlite banding, partially attributed to differences in diffusivity between the bands [36]. In the study by Myhre et al. [52], parallel ridges were observed at the fracture surface of the Vintage steel with both ductile and brittle features. The difference in diffusivity in the ferrite and pearlite bands, in addition to an accumulation of hydrogen at the interfaces, were recognized as contributing factors to the observed ridges and the higher hydrogen embrittlement susceptibility of the Vintage steel. Due to the limited wall thickness of the pipelines, the orientational dependency of the diffusivity was not tested; Hence, a conclusion on the degree of tortuosity effect cannot be made.

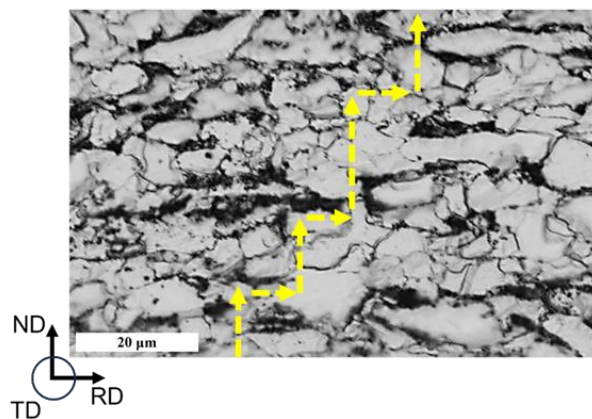


Fig. 14. Illustration of a possible hydrogen diffusion path in the Vintage steel in a permeation experiment. Hydrogen diffusion in permeation tests proceeds in the normal direction. ND - Normal direction, RD – Rolling direction, and TD – Transverse direction.

4.4 Concentration-dependent diffusivity

In this work, gaseous charging was utilized for desorption tests while electrochemical charging was conducted during permeation tests. Care should be taken when comparing the diffusivities obtained under different charging conditions because trap occupancy can affect D_{eff} [68,69]. According to Johnson et al. [70] and Oriani [71], D_{eff} is concentration-independent if the fraction of occupied traps is close to zero. D_{eff} is affected by the binding energy, E_b , and the density of traps, N_T [72]. From the work of Oriani [71], E_b and N_T can be estimated by Eq. (8), which relates D_L and D_{eff} under the assumption of local equilibrium between hydrogen in lattice and traps and low trap occupancy [55,63,71]. T and R_g denotes the temperature and gas constant, respectively. The density of lattice sites, N_L , was set to 5.1×10^{23} sites/cm³ [72], and the D_L values reported by Kiuchi and McLellan [4] were used in the calculations. By plotting $\ln(D_L/D_{\text{eff}}-1)$ versus $1/T$, E_b and N_T can be calculated from the slope and y-axis intercept, respectively [55].

$$D_{\text{eff}} = D_L \left(1 + \frac{N_T}{N_L} \exp\left(\frac{E_b}{R_g T}\right) \right)^{-1} \quad (8)$$

The E_b determined by the desorption methods and partial permeation transients were 28.2 and 28.9 kJ/mol for the Modern steel and 26.0 and 20.4 kJ/mol for the Vintage steel. Possible trap sites are dislocations (25.6 kJ/mol–26.8 kJ/mol [40,41]), grain boundaries (17.2–30.1 kJ/mol [40,73]), and ferrite-cementite interfaces (18.4–19 kJ/mol [74,75]). Assigning E_b to a specific microstructural feature for complex microstructures consisting of several possible trap sites is challenging, and several trap sites could contribute to the determined value. For the Modern steel, N_T was 1.1×10^{20} and 9.3×10^{19} sites/cm³ determined by desorption and partial permeation transients, respectively. For the Vintage steel, N_T was 3.6×10^{20} and 1.7×10^{22} sites/cm³ determined by the same methods, respectively. Lower N_T in the Modern steel compared with the Vintage steel could be attributed to tempering reducing the dislocation density and the slightly larger grain size in the Modern steel (7 μm) than in the Vintage steel (4 μm).

The partial permeation results in Fig. 11 and Table 5 showed that D_{eff} of the Modern steel was independent of the charging current density, while it increased with increasing current density for the Vintage steel. These experimental results imply that only the Modern steel satisfied the assumption of low trap occupancy. However, according to the works by Chen et al. [63]

and Zheng et al. [76], the E_b determined for the Vintage steel is not sufficient to cause a significant trap occupancy for the obtained C_H . If the assumption of low trap occupancy is not fulfilled, the determination of E_b and N_T by Eq. (8) might not be correct. Failing to fulfill the assumptions could give rise to the difference in E_b and N_T values for the Vintage steel determined by desorption and partial transients. In addition, Eq. (8) only yields a single value for E_b and N_T , which reflects the properties of a dominating trap site and cannot yield specific values for different trap sites. The difference in the E_b values of the Vintage steel between the desorption and partial-permeation tests could also suggest that the dominating trap sites differed between these two methods. One of the possible causes of the concentration-dependent diffusivity and the large scatter in determined diffusivity for the Vintage steel is a contribution of multiple traps to the determined D_{eff} . In contrast to the normalized curves observed for the Modern steel in Fig. 2, broad, asymmetric curves were observed for the Vintage steel in Fig. 4, which suggest the existence of multiple major trap sites in the Vintage steel. It is speculated that the contribution degrees of these major trap sites to the determined D_{eff} varied depending on charging conditions, leading to the concentration-dependent diffusivity of the Vintage steel. A thermal desorption analysis using the Kissinger equation could yield further information regarding E_b for different trap sites [40,77] and will be conducted in a subsequent study.

5. Conclusion

This study investigated the hydrogen diffusivity in two X65 pipeline steels by hydrogen desorption and permeation methods. The Modern steel, from a seamless quenched and tempered pipe, had a microstructure of equiaxed ferrite and bainite grains. The Vintage steel, from a hot-rolled and welded pipe, consisted of a banded ferritic-pearlitic microstructure. In-situ and ex-situ hydrogen desorption measurements were employed to determine the diffusivity of samples charged in pressurized H_2 gas. Electrochemical hydrogen permeation was performed with both complete subsequent transients and partial permeation transients. The main conclusions drawn from the study are summarized as follows:

- To account for strongly trapped hydrogen, we proposed a modified solution of Fick's 2nd law. The modified solution obtained a good fit with the obtained data, and there was a good agreement between the diffusivities determined by the two desorption methods for both steels.

- The highest measured effective diffusion coefficient, D_{eff} , for the Modern and Vintage steels at room temperature were comparable: 2.70×10^{-6} and 3.34×10^{-6} cm²/s for the Modern and Vintage steel, respectively.
- The scatter factor between the lowest and highest measured D_{eff} at room temperature was about three for the Modern steel and 17 for the Vintage steel. The scatter difference indicated that the significance of the method and charging condition utilized can vary between steels.
- Two possible causes for the larger scatter factor of D_{eff} for the Vintage steel were recognized: Presence of multiple major trap sites causing a concentration-dependent D_{eff} , and a tortuous diffusion path caused by ferrite-pearlite bands due to slow diffusion in pearlite.

Acknowledgements

This work has been supported by the Research Council of Norway through the H2Ninja project (309378) and the HyLINE project (294739). In addition, by industry company partners in the HyLINE project.

References

- [1] Johnson WH. On Some Remarkable Changes Produced in Iron and Steel by the Action of Hydrogen and Acids. *Proc R Soc Lond* 1874;23:168–79.
- [2] Lynch S. Hydrogen embrittlement phenomena and mechanisms. *Corros Rev* 2012;30:105–23.
- [3] Drexler A, He S, Pippan R, Romaner L, Razumovskiy VI, Ecker W. Hydrogen segregation near a crack tip in nickel. *Scripta Mater* 2021;194:113697.
- [4] Kiuchi K, McLellan RB. The solubility and diffusivity of hydrogen in well-annealed and deformed iron. *Acta Metall* 1983;31:961–84.
- [5] Turnbull A. 4 - Hydrogen diffusion and trapping in metals. In: Gangloff RP, Somerday BP, editors. *Gaseous Hydrogen Embrittlement of Materials in Energy Technologies*, vol. 1, 2012, p. 89–128.
- [6] Pressouyre GM, Bernstein IM. A quantitative analysis of hydrogen trapping. *Metall Trans A* 1978;9:1571–80.
- [7] Pressouyre GM. A classification of hydrogen traps in steel. *Metall Trans A* 1979;10:1571–3.
- [8] Legrand E, Feaugas X, Bouhattate J. Generalized model of desorption kinetics: Characterization of hydrogen trapping in a homogeneous membrane. *Int J Hydrog Energy* 2000;39:8374–84.
- [9] Bhadeshia HKDH. Prevention of Hydrogen Embrittlement in Steels. *ISIJ International* 2016;56:24–36.
- [10] Pressouyre GM, Bernstein IM. An example of the effect of hydrogen trapping on hydrogen embrittlement. *Metall Trans A* 1981;12:835–44.
- [11] Devanathan MAV, Stachurski Z. The Adsorption and Diffusion of Electrolytic Hydrogen in Palladium. *Proc R Soc Lond Ser A Math Phys Sci* 1962;270:90–102.

- [12] Kumnick AJ, Johnson HH. Steady state hydrogen transport through zone refined irons. *Metal Trans A* 1975;6:1087–91.
- [13] Koren E, M. H. Hagen C, Wang D, Lu X, Johnsen R, Yamabe J. Experimental comparison of gaseous and electrochemical hydrogen charging in X65 pipeline steel using the permeation technique. *Corros Sci* 2023;215:111025.
- [14] Koren E, Hagen CMH, Wang D, Lu X, Johnsen R. Investigating electrochemical charging conditions equivalent to hydrogen gas exposure of X65 pipeline steel. *Mater Corros* 2023.
- [15] Zakroczyński T. Adaptation of the electrochemical permeation technique for studying entry, transport and trapping of hydrogen in metals. *Electrochim Acta* 2006;51:2261–6.
- [16] Latypova R, Nyo TT, Seppälä O, Hahtonen K, Hänninen H, Kömi J, et al. The effect of Pd and Ni coatings on hydrogen permeation experiments of as-quenched martensitic steel. *Corros Rev* 2023.
- [17] Ma HC, Zagidulin D, Goldman M, Shoesmith DW. Influence of iron oxides and calcareous deposits on the hydrogen permeation rate in X65 steel in a simulated groundwater. *Int J Hydrog Energy* 2021;46:6669–79.
- [18] Zafra A, Harris Z, Korec E, Martínez-Pañeda E. On the relative efficacy of electropermeation and isothermal desorption approaches for measuring hydrogen diffusivity. *Int J Hydrog Energy* 2023;48:1218–33.
- [19] Van Den Eeckhout E, Verbeken K, Depover T. Methodology of the electrochemical hydrogen permeation test: A parametric evaluation. *Int J Hydrog Energy* 2023;48.
- [20] Turnbull A. Factors Affecting the Reliability of Hydrogen Permeation Measurement. *Mater Sci Forum* 1995;192–194:63–78.
- [21] Liu Q, Atrens A. Reversible hydrogen trapping in a 3.5NiCrMoV medium strength steel. *Corros Sci* 2015;96:112–20.
- [22] Fallahmohammadi E, Bolzoni F, Lazzari L. Measurement of lattice and apparent diffusion coefficient of hydrogen in X65 and F22 pipeline steels. *Int J Hydrog Energy* 2013;38:2531–43.
- [23] Zafra A, Harris Z, Sun C, Martínez-Pañeda E. Comparison of hydrogen diffusivities measured by electrochemical permeation and temperature-programmed desorption in cold-rolled pure iron. arXiv:211200589 [Cond-Mat, Physics:Physics] 2021.
- [24] Yamabe J, Awane T, Matsuoka S. Investigation of hydrogen transport behavior of various low-alloy steels with high-pressure hydrogen gas. *Int J Hydrog Energy* 2015;40:11075–86.
- [25] Yamabe J, Takakuwa O, Matsunaga H, Itoga H, Matsuoka S. Hydrogen diffusivity and tensile-ductility loss of solution-treated austenitic stainless steels with external and internal hydrogen. *Int J Hydrog Energy* 2017;42:13289–99.
- [26] Lu X, Depover T, Johnsen R. Evaluation of hydrogen diffusion and trapping in nickel Alloy 625 by thermal desorption spectroscopy. *Int J Hydrog Energy* 2022;47:31673–83.
- [27] Matsuo T, Yamabe J, Furukawa H, Seki K, Shimizu K, Watanabe S, et al. Development of New Strain Gage for High-Pressure Hydrogen Gas Use. *Exp Mech* 2014;54:431–42.
- [28] Claeys L, Cnockaert V, Depover T, Graeve ID, Verbeken K. Critical assessment of the evaluation of thermal desorption spectroscopy data for duplex stainless steels: A combined experimental and numerical approach. *Acta Mater* 2020;186:190–8.
- [29] Simoni L, Falcade T, Ferreira DCF, Kwietniewski CEF. An integrated experimental and modeling approach to determine hydrogen diffusion and trapping in a high-strength steel. *Int J Hydrog Energy* 2021;46:25738–51.
- [30] Cerniauskas S, Jose Chavez Junco A, Grube T, Robinius M, Stolten D. Options of natural gas pipeline reassignment for hydrogen: Cost assessment for a Germany case study. *Int J Hydrog Energy* 2020;45:12095–107.
- [31] Tsiklíos C, Hermesmann M, Müller TE. Hydrogen transport in large-scale transmission pipeline networks: Thermodynamic and environmental assessment of repurposed and new pipeline configurations. *Applied Energy* 2022;327:120097.
- [32] Laureys A, Depraetere R, Cauwels M, Depover T, Hertelé S, Verbeken K. Use of existing steel pipeline infrastructure for gaseous hydrogen storage and transport: A review of factors affecting hydrogen induced degradation. *J Nat Gas Sci Eng* 2022;101.
- [33] Briottet L, Batisse R, de Dinechin G, Langlois P, Thiers L. Recommendations on X80 steel for the design of hydrogen gas transmission pipelines. *Int J Hydrog Energy* 2012;37:9423–30.

- [34] Ranjbar M, Miresmaeili R, Naimi-Jamal MR, Mirzaei M. Effect of Microstructure on the Mechanical Properties and Fracture Toughness of API X65 Pipeline Steel in the Presence of Hydrogen. *Met Mater Int* 2021;27:3918–34.
- [35] Park GT, Koh SU, Jung HG, Kim KY. Effect of microstructure on the hydrogen trapping efficiency and hydrogen induced cracking of linepipe steel. *Corros Sci* 2008;50:1865–71.
- [36] Ronevich JA, Somerday BP, San Marchi CW. Effects of microstructure banding on hydrogen assisted fatigue crack growth in X65 pipeline steels. *Int J Fatigue* 2016;82:497–504.
- [37] Tau L, Chan SLI. Effects of ferrite/pearlite alignment on the hydrogen permeation in a AISI 4130 steel. *Mater Lett* 1996;29:143–7.
- [38] Ohaeri E, Eduok U, Szpunar J. Hydrogen related degradation in pipeline steel: A review. *Int J Hydrog Energy* 2018;43:14584–617.
- [39] Lee H, Lap-Ip Chan S. Hydrogen embrittlement of AISI 4130 steel with an alternate ferrite/pearlite banded structure. *Mat Sci Eng A* 1991;142:193–201.
- [40] Choo WY, Lee JY. Thermal analysis of trapped hydrogen in pure iron. *Metall and Mat Trans A* 1982;13:135–40.
- [41] Choo WY, Lee JY. Effect of cold working on the hydrogen trapping phenomena in pure iron. *Metall Trans A* 1983;14:1299–305.
- [42] Wei FG, Tsuzaki K. Quantitative analysis on hydrogen trapping of TiC particles in steel. *Metall and Mat Trans A* 2006;37:331–53.
- [43] Dunne DP, Hejazi D, Saleh AA, Haq AJ, Calka A, Pereloma EV. Investigation of the effect of electrolytic hydrogen charging of X70 steel: I. The effect of microstructure on hydrogen-induced cold cracking and blistering. *Int J Hydrog Energy* 2016;41:12411–23.
- [44] Cheng YF. Analysis of electrochemical hydrogen permeation through X-65 pipeline steel and its implications on pipeline stress corrosion cracking. *Int J Hydrog Energy* 2007;32:1269–76.
- [45] Jack TA, Pourazizi R, Ohaeri E, Szpunar J, Zhang J, Qu J. Investigation of the hydrogen induced cracking behaviour of API 5L X65 pipeline steel. *Int J Hydrog Energy* 2020;45:17671–84.
- [46] Fallahmohammadi E, Bolzoni F, Fumagalli G, Re G, Benassi G, Lazzari L. Hydrogen diffusion into three metallurgical microstructures of a C–Mn X65 and low alloy F22 sour service steel pipelines. *Int J Hydrog Energy* 2014;39:13300–13.
- [47] Olden V, Alvaro A, Akselsen OM. Hydrogen diffusion and hydrogen influenced critical stress intensity in an API X70 pipeline steel welded joint – Experiments and FE simulations. *Int J Hydrog Energy* 2012;37:11474–86.
- [48] Thomas A, Szpunar JA. Hydrogen diffusion and trapping in X70 pipeline steel. *Int J Hydrog Energy* 2020;45:2390–404.
- [49] Skjellerudsveen M, Akselsen OM, Olden V, Johnsen R, Smirnova A. Effect of Microstructure and Temperature on Hydrogen Diffusion and Trapping in X70 grade Pipeline Steel and its Weldments, Proc EUROCORR conf, Moscow; 2010.
- [50] Dey S, Sivaprasad S, Das N, Chatteraj I. Study of Electrochemical Behavior, Hydrogen Permeation and Diffusion in Pipeline Steel. *Mater Sci Forum* 2021;1019:145–56.
- [51] Zhang T, Zhao W, Li T, Zhao Y, Deng Q, Wang Y, et al. Comparison of hydrogen embrittlement susceptibility of three cathodic protected subsea pipeline steels from a point of view of hydrogen permeation. *Corros Sci* 2018;131:104–15.
- [52] Myhre AO, Hagen AB, Nyhus B, Olden V, Alvaro A, Vinogradov A. Hydrogen Embrittlement Assessment of Pipeline Materials Through Slow Strain Rate Tensile Testing. *Procedia Struct Integr* 2022;42:935–42.
- [53] Wang D, Hagen AB, Wan D, Lu X, Johnsen R. Probing hydrogen effect on nanomechanical properties of X65 pipeline steel using in-situ electrochemical nanoindentation. *Mater Sci Eng A* 2021;824:141819.
- [54] Manolatos P, Jerome M, Galland J. Necessity of a palladium coating to ensure hydrogen oxidation during electrochemical permeation measurements on iron. *Electrochim Acta* 1995;40:867–71.
- [55] Husby H, Iannuzzi M, Johnsen R, Kappes M, Barnoush A. Effect of nickel on hydrogen permeation in ferritic/pearlitic low alloy steels. *Int J Hydrog Energy* 2018;43:3845–61.

- [56] Bruzzoni P, Carranza RM, Lacoste JRC. Influence of palladium films on hydrogen gas entry into iron: a study by electrochemical impedance spectroscopy. *Int J Hydrog Energy* 2000;5.
- [57] Castaño Rivera P, Ramunni VP, Bruzzoni P. Hydrogen trapping in an API 5L X60 steel. *Corros Sci* 2012;54:106–18.
- [58] Demarez A, Hocks AG, Meuniers FA. Diffusion of hydrogen in mild steel. *Acta Metall* 1954;2:214–23.
- [59] ISO 17081 Method of measurement of hydrogen permeation and determination of hydrogen uptake and transport in metals by an electrochemical technique 2014.
- [60] Practice for Evaluation of Hydrogen Uptake, Permeation, and Transport in Metals by an Electrochemical Technique. ASTM International; 2018.
- [61] Frappart S, Feaugas X, Creus J, Thebault F, Delattre L, Marchebois H. Study of the hydrogen diffusion and segregation into Fe–C–Mo martensitic HSLA steel using electrochemical permeation test. *J Phys Chem Solids* 2010;71:1467–79.
- [62] Turnbull A. The effect of H₂S concentration and pH on hydrogen permeation in AISI 410 stainless steel in 5% NaCl. *Corros Sci* 1989;29:93–104.
- [63] Cheng L, Li L, Zhang X, Liu J, Wu K. Numerical simulation of hydrogen permeation in steels. *Electrochim Acta* 2018;270:77–86.
- [64] Karimi S, Taji I, Palencsár S, Dugstad A, Hajilou T, Barnoush A, et al. Evaluation of microstructural and environmental effects on the hydrogen uptake and desorption in high-strength carbon steels: A thermal desorption spectroscopy study. *Corros Sci* 2023;219:111210.
- [65] Peng Z, Liu J, Huang F, Hu Q, Cheng Z, Liu S, et al. Effect of Submicron-Scale MnS Inclusions on Hydrogen Trapping and HIC Susceptibility of X70 Pipeline Steels. *Steel Res Int* 2018;89:1700566.
- [66] Xue HB, Cheng YF. Characterization of inclusions of X80 pipeline steel and its correlation with hydrogen-induced cracking. *Corros Sci* 2011;53:1201–8.
- [67] Bolzoni F, Fallahmohammadi E. Electrochemical Investigation of Hydrogen Diffusion in Pipeline Steels. *NACE CORROSION*, 2013, p. NACE-2013-2792.
- [68] Griffiths AJ, Turnbull A. On the effective diffusivity of hydrogen in low alloy steels. *Corros Sci* 1995;37:1879–81.
- [69] Drexler A, Vandewalle L, Depover T, Verbeken K, Domitner J. Critical verification of the Kissinger theory to evaluate thermal desorption spectra. *Int J Hydrog Energy* 2021;46:39590–606.
- [70] Johnson HH, Quick N, Kumnick AJ. Hydrogen trapping mechanisms by permeation techniques. *Scripta Metall* 1979;13:67–72.
- [71] Oriani RA. The diffusion and trapping of hydrogen in steel. *Acta Metall* 1970;18:147–57.
- [72] Krom AHM, Bakker A. Hydrogen trapping models in steel. *Metall Mater Trans B* 2000;31:1475–82.
- [73] Bernstein IM. The effect of hydrogen on the deformation of iron. *Scripta Metall* 1974;8:343–9.
- [74] Choo WY, Lee JY. Hydrogen trapping phenomena in carbon steel. *J Mater Sci* 1982;17:1930–8.
- [75] Takai K. Hydrogen Existing States in Metals. *Trans JSME Ser A* 2004;70:1027–35.
- [76] Zheng S, Qin Y, Li W, Huang F, Qiang Y, Yang S, et al. Effect of hydrogen traps on hydrogen permeation in X80 pipeline steel - a joint experimental and modelling study. *Int J Hydrog Energy* 2023;48:4773–88.
- [77] Kissinger HE. Reaction Kinetics in Differential Thermal Analysis. *Anal Chem* 1957;29:1702–6.

Report

Hydrogen uptake and diffusivity in X65 steels: Unpublished results

This report is not included in NTNU Open

ISBN 978-82-326-7768-9 (printed ver.)
ISBN 978-82-326-7767-2 (electronic ver.)
ISSN 1503-8181 (printed ver.)
ISSN 2703-8084 (online ver.)



NTNU

Norwegian University of
Science and Technology